Cell Systems

Article

High-Throughput Affinity Measurements of Transcription Factor and DNA Mutations Reveal Affinity and Specificity Determinants

Graphical Abstract

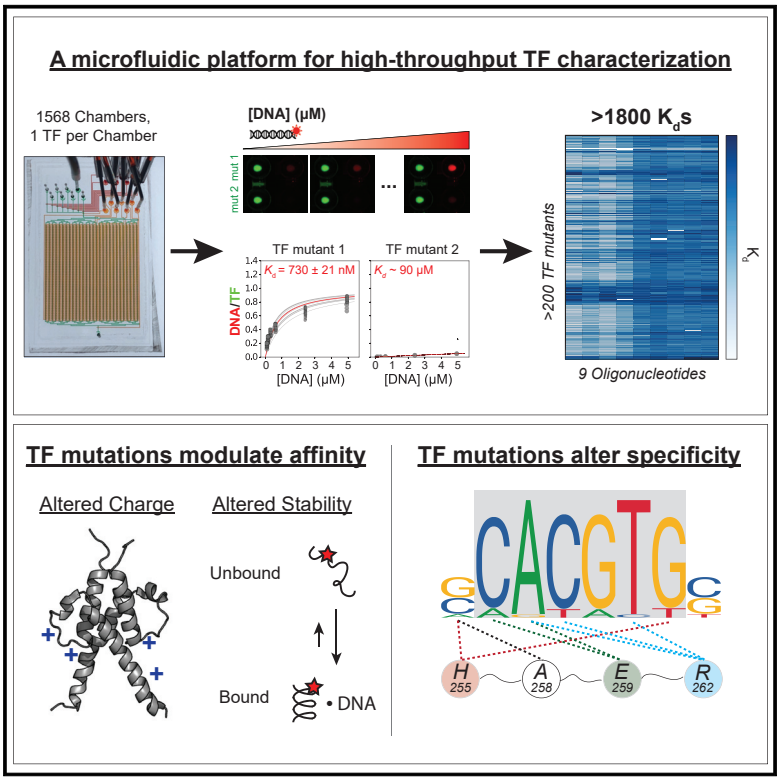

Authors

Arjun K. Aditham, Craig J. Markin, Daniel A. Mokhtari, Nicole DelRosso, Polly M. Fordyce

Correspondence

pfordyce@stanford.edu

In Brief

Aditham et al. report a microfluidic platform for quantitatively measuring the effects of transcription factor mutations on DNA binding for hundreds of variants in parallel and reveal that many combinations of mutations within transcription factors and DNA can tune affinities over a wide, physiologically relevant range.

Highlights

- Microfluidic platform for high-throughput biophysical analysis of protein variants
- Binding affinities of ~210 Pho4 variants with 9 DNA sequences (~1,800 measurements)
- Mutating non-conserved Pho4 residues and flanking nucleotides alters DNA affinity
- Double-mutant cycles of Pho4-DNA interface reveal drivers of binding specificity

Aditham et al., 2021, Cell Systems *12*, 112–127
February 17, 2021
https://doi.org/10.1016/j.cels.2020.11.012

CellPress

CellPress

Cell Systems

Article

High-Throughput Affinity Measurements of Transcription Factor and DNA Mutations Reveal Affinity and Specificity Determinants

Arjun K. Aditham,[1,2] Craig J. Markin,[3,8] Daniel A. Mokhtari,[3,8] Nicole DelRosso,[4] and Polly M. Fordyce[1,2,5,6,7,*]

[1]Department of Bioengineering, Stanford University, Stanford, CA 94305, USA
[2]Stanford ChEM-H, Stanford University, Stanford, CA 94305, USA
[3]Department of Biochemistry, Stanford University, Stanford, CA 94305, USA
[4]Graduate Program in Biophysics, Stanford University, Stanford, CA 94305, USA
[5]Department of Genetics, Stanford University, Stanford, CA 94305, USA
[6]Chan Zuckerberg Biohub, San Francisco, CA 94110, USA
[8]These authors contributed equally
[7]Lead Contact
*Correspondence: pfordyce@stanford.edu
https://doi.org/10.1016/j.cels.2020.11.012

SUMMARY

Transcription factors (TFs) bind regulatory DNA to control gene expression, and mutations to either TFs or DNA can alter binding affinities to rewire regulatory networks and drive phenotypic variation. While studies have profiled energetic effects of DNA mutations extensively, we lack similar information for TF variants. Here, we present STAMMP (simultaneous transcription factor affinity measurements via microfluidic protein arrays), a high-throughput microfluidic platform enabling quantitative characterization of hundreds of TF variants simultaneously. Measured affinities for ~210 mutants of a model yeast TF (Pho4) interacting with 9 oligonucleotides (>1,800 K_ds) reveal that many combinations of mutations to poorly conserved TF residues and nucleotides flanking the core binding site alter but preserve physiological binding, providing a mechanism by which combinations of mutations in *cis* and *trans* could modulate TF binding to tune occupancies during evolution. Moreover, biochemical double-mutant cycles across the TF-DNA interface reveal molecular mechanisms driving recognition, linking sequence to function. A record of this paper's Transparent Peer Review process is included in the Supplemental Information.

INTRODUCTION

Regulation of gene expression is critical for proper organismal development and response to environmental stimuli. This regulation is accomplished primarily by transcription factor (TF) proteins that bind specific regulatory DNA sequences in the genome to activate or repress gene expression (Mitsis et al., 2020). Reflecting this central role in cellular function, mutations to either DNA regulatory sequences or TF proteins have profound effects across evolution and medicine. Mutations that alter TF-DNA interactions in *cis* (DNA-binding sites) or in *trans* (diffusible factors, e.g., TFs) drive organismal evolution by rewiring transcriptional networks and generating phenotypic variation (Signor and Nuzhdin, 2018; Wong et al., 2017). In medicine, the majority of disease-associated mutations in humans are found within regulatory DNA (Maurano et al., 2012; Nishizaki et al., 2020), and mutations in TFs often lead to cancers (Lambert et al., 2018a; Lee and Young, 2013) and developmental disorders (Lee and Young, 2013; Barrera et al., 2016). A quantitative and predictive understanding of how mutations affect TF-DNA binding interactions would, therefore, have broad impacts on understanding biology.

The probability of TF occupancy at a given genomic site is typically modeled as a function of the Gibbs free energy of binding (ΔG) for that TF-DNA sequence combination and the effective concentration of free TFs in the nucleus (Foat et al., 2006; Kim and O'Shea, 2008; Segal et al., 2008; Gertz and Cohen, 2009; Weirauch et al., 2013; Zhao and Stormo, 2011; Le et al., 2018). As a result, differences in binding site affinity and available TF concentrations can modulate the strength and timing of transcriptional programs (Crocker et al., 2016). While much effort has focused on determining the highest affinity sites for a given TF (Chen et al., 2016; Jolma et al., 2010; Zykovich et al., 2009), nonspecific and low-affinity sites in the genome often play essential functional roles and are evolutionarily conserved (Farley et al., 2015; Crocker et al., 2016; Kribelbauer et al., 2019). Given that even subtle changes in affinity can alter transcription (Meinhardt et al., 2013; Rajkumar et al., 2013; Le et al., 2018), understanding how TF and DNA mutations affect binding requires the ability to measure affinities with high accuracy over a wide energetic range.

Many prior efforts have comprehensively characterized how variation in underlying DNA sequence alters TF binding energies

for up to 10^6 DNA variants in parallel (Le et al., 2018). These studies have established that typical TF-DNA binding energies span nearly 2–3 orders of magnitude (~3 kcal/mol) (Nutiu et al., 2011; Kribelbauer et al., 2019), that mutations to nucleotides within or flanking the "core" consensus site can alter affinities over a wide range (Le et al., 2018; Maerkl and Quake, 2007), and that measured binding energies can predict levels of induction and rates of transcription *in vivo* (Gaudet and Mango, 2002; Aow et al., 2013).

By contrast, far less is known about how mutations throughout a TF protein alter DNA binding, even though binding energies depend on the sequences of both the underlying DNA and the TF. This lack of data likely stems from the technical challenges associated with high-throughput expression, purification, and quantitative biophysical characterization of large TF mutant libraries. Current large-scale studies of simultaneous TF and DNA mutants have been performed with non-thermodynamic screening approaches (Maerkl and Quake, 2009; Persikov et al., 2015). Previous quantitative studies have focused on limited sets of residues, such as those that directly contact the DNA sequence (Ferreiro et al., 2008; Maerkl and Quake, 2009; Wang et al., 2017), regulate dimerization of protein partners (Voronova and Baltimore, 1990), or are associated with human disease (Barrera et al., 2016). While these studies have confirmed that mutations at strongly conserved residues typically dramatically alter DNA-binding affinity, the effects of mutations at poorly conserved residues remain understudied (Meinhardt et al., 2013). Large quantitative datasets describing the effects of mutations throughout and surrounding TF binding domains on DNA binding could reveal mechanistic insights not easily inferred from static crystal structures and provide critical information about binding interfaces for TFs recalcitrant to crystalization efforts (Fuxreiter et al., 2011). In addition, such datasets would also provide an invaluable resource for optimizing computational methods designed to predict mutational effects for precision medicine (Ng and Henikoff, 2003; Adzhubei et al., 2010; Choi et al., 2012) and create synthetic transcriptional circuits.

Here, we report the development of simultaneous transcription factor affinity measurements via microfluidic protein arrays (STAMMP), a microfluidic platform capable of measuring binding affinities for >1,500-TF mutants simultaneously interacting with a DNA sequence of interest in a single experiment. As a first application, we systematically quantify mutational effects on DNA-binding affinity and specificity for Pho4, a homodimeric basic helix-loop-helix (bHLH) TF in yeast that binds a 5′-CACGTG-3′ E-box motif to drive gene expression in response to phosphate starvation (Ogawa et al., 2000). We measured more than 1,800 binding affinities (K_ds or ΔGs) for ~210 Pho4 mutants interacting with oligonucleotides containing mutations within and flanking the core E-box site and found that a large fraction (>70%) of residue mutations have statistically significant effects on DNA binding. Strikingly, of the more than 1,800 pairs of TF and DNA mutations assayed, nearly 70% of mutations that altered but did not ablate binding occurred at nucleotides outside of the core binding site and at residues that do not contact DNA nucleotides. These combinations of mutations in *cis* and in *trans* could tune affinities across a wide range, illustrating the importance of previously unexplored and poorly conserved residues in modulating TF function. Finally, biochemical double-mutant cycles between TF amino acid residue and DNA nucleotide mutations provide mechanistic insight into the interactions that govern recognition, quantifying the energetic contributions of contacts predicted from the crystal structure and revealing additional residues required for specificity. We anticipate that STAMMP and the presented data will be broadly useful for the future development of quantitative models designed to link TF sequence to structure and function.

RESULTS

STAMMP Enables High-Throughput Characterization of the Functional Effects of TF Mutations on DNA Binding

High-throughput functional characterization of large numbers of TF mutants requires the ability to recombinantly express and purify hundreds of TFs in parallel. To accomplish this task, STAMMP affinity measurements take place within a microfluidic device containing 1,568 valved reaction chambers, each of which contains a "plasmid" compartment and a "binding reaction" compartment (Figures 1A and S1) (Fordyce et al., 2010; Maerkl and Quake, 2007). Three sets of valves control fluid flow within and between reaction chambers: "neck" valves separate plasmid and binding compartments, "sandwich" valves physically sequester reaction chambers from one another to prevent cross-contamination, and "button" valves (Figure 1A) in the binding compartment enable selective surface patterning within the device and trap macromolecular binding interactions at equilibrium for quantitative affinity measurements.

To program each reaction chamber with a specific TF variant, microfluidic devices are aligned to spotted plasmid arrays (Figure 1B). Each plasmid encodes expression of a TF variant fused to a C-terminal monomeric eGFP tag (Zacaharias et al., 2002), with the identity of each mutant encoded by its position in the array. After alignment, device surfaces are specifically patterned with anti-eGFP antibodies (anti-GFP) beneath the "button" valve and coated elsewhere with biotinylated bovine serum albumin (bBSA) to prevent nonspecific adsorption. All TF variants are then expressed in parallel via the introduction of cell-free extract into each chamber and incubation of the device for 45 minutes at 37°C. After expression, TFs are purified via recruitment to antibody-patterned surfaces (Figures 1B and 2). Subsequent closing of the "button" valves allows extensive washing and trypsin digestion to remove any nonspecifically bound TFs and cell-free expression components while protecting surface-immobilized protein; the final eGFP fluorescence intensity in each chamber reports on the amount of immobilized TF (Figures 1B and 1C).

To measure full binding isotherms for all expressed TFs interacting with a particular oligonucleotide sequence, we iteratively introduce fluorescently tagged DNA duplexes at multiple concentrations across all chambers (Figures 1C and 2). After allowing reactions to come to equilibrium, we again close the "button" valves in each chamber, thereby trapping all bound TF-DNA complexes. After washing, we image all reaction chambers across the device to quantify TF and DNA intensities and estimate fractional occupancies (Figure 1C). We then fit estimated fractional occupancies as a function of the effective concentration of free DNA in solution (calculated from intensities using per-chamber calibration curves, Figure S2) to a Langmuir isotherm to extract binding affinities (K_ds) and relative

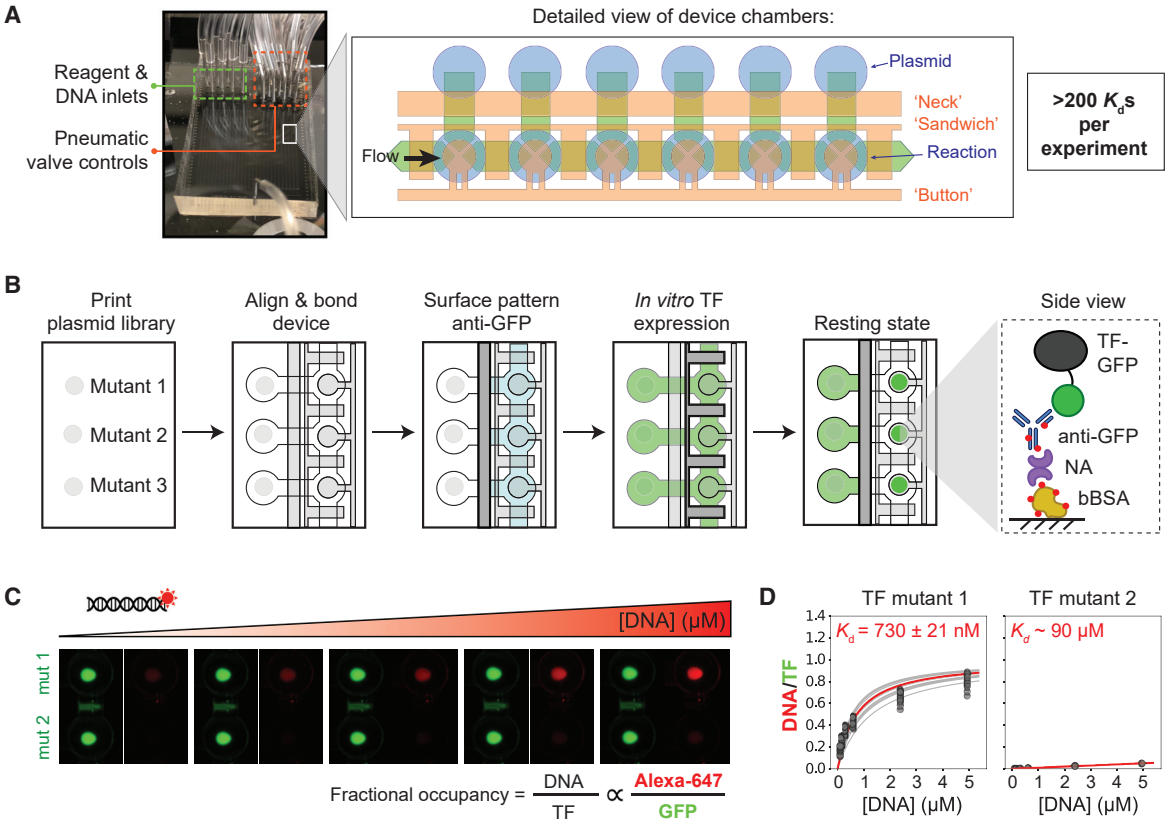

Figure 1. STAMMP: Microfluidic Platform for High-Throughput TF Expression and Assays

(A) Photograph of MITOMI device with labeled reagent and DNA inlets and pneumatic valve controls highlighted (left). Inset (right) shows plasmid (labeled "plasmid") and DNA binding reaction compartments (labeled "reaction") and annotated pneumatic valves ("button," "sandwich," and "neck") in orange.

(B) Workflow for device surface functionalization and *in situ* expression and purification of TF libraries and final schematic of components used for surface-immobilization of eGFP-tagged TFs (right). Components of functionalized surface, include bBSA, NeutrAvidin (NA), and biotinylated anti-GFP, which binds the GFP-tagged TF (TF-GFP).

(C) Workflow illustrating iterative introduction, equilibration, and trapping of TF-bound fluorescently labeled DNA to quantify concentration-dependent binding; final ratios of DNA and TF fluorescence are proportional to fractional occupancy. Image contrast was enhanced to improve visibility for display purposes.

(D) Langmuir isotherms fit DNA/TF fluorescence intensity ratios as a function of free DNA concentration yield interaction binding affinities. Example raw binding data (gray markers and fit lines) and calculated median fit curves (red lines) for 2 mutants are shown at right. K_d values represent median values ± SEM for statistical replicates.

differences in binding affinities (ΔΔGs) for all TFs in parallel (Figure 1D).

A Library of Pho4 Mutants Designed to Probe Mechanisms of Binding Site Recognition

bHLH TFs are highly abundant in eukaryotes, representing the third most abundant TF structural class in the human genome (Lambert et al., 2018b). Pho4 is one of the eight bHLHs in *S. cerevisiae* (Chen and Lopes, 2007), and prior work has established that Pho4 binds the E-box core motif (5′-CACGTG-3′) element to drive gene expression in response to phosphate starvation. In addition to this well-characterized and inducible biological function, Pho4 has a well-characterized DNA-binding interface (Shimizu et al., 1997; Cave et al., 2000) and a wealth of prior biophysical data describing how mutations to the underlying DNA sequence affect affinity (Maerkl and Quake, 2007; Fordyce et al., 2010; Le et al., 2018). Comparisons between the Pho4 crystal structure and those of other bHLH proteins (Shimizu et al., 1997; Brownlie et al., 1997; Párraga et al., 1998) also show structural similarity, suggesting that Pho4 can serve as a model for understanding how bHLH specificity is encoded in a protein sequence.

The DNA-binding domains (DBDs) of all bHLH TF superfamily members contain a helical basic region (which directly contacts DNA) and two additional helices separated by an unstructured loop of variable length (Figure 3A). Four residues within the basic region directly contact nucleobases within the major groove of the E-box recognition site and are strongly conserved throughout organisms, including yeast and humans (R252, H255, E259, and R263 in Pho4); additional residues within the loop contact the DNA backbone (Figures 3A and S3). Pho4 binds DNA as a homodimer (Figure 3B), with conserved hydrophobic residues in the helix 1 and helix 2 regions promoting stable dimerization (Figure 3A).

To systematically probe how residues throughout and immediately surrounding the DBD contribute to binding affinity and specificity, we generated a library of 223 Pho4 mutants comprising systematic substitutions, variants from other bHLH

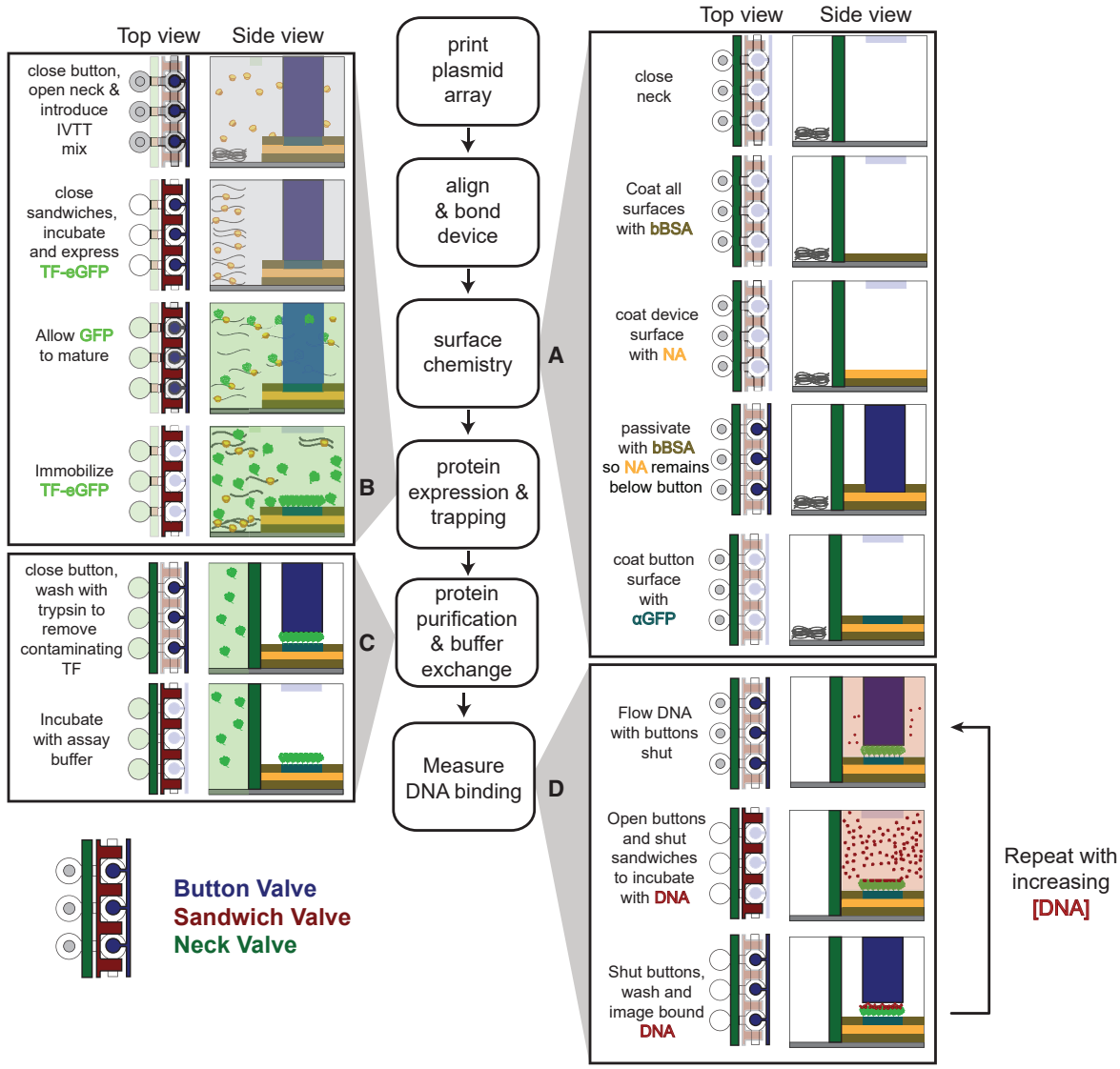

Figure 2. Detailed Experimental Workflow

(A) Surface chemistry to pattern antibody in device for subsequent TF immobilization.

(B) Expression of GFP-tagged TFs via *in vitro* transcription/translation with sandwich valves depressed to prevent cross-contamination. After allowing GFP to fold and mature, button valves are opened to bind expressed protein to patterned antibody-coated surfaces.

(C) Trypsin digest of nonspecifically bound TFs and equilibration of trapped TF in assay buffer.

(D) Schematic showing introduction of DNA at a single concentration to quantify binding, with measurements repeated over multiple DNA concentrations to generate a concentration-dependent binding curve.

orthologs, known disease-associated variants from human orthologs, and a selection of mutants designed to probe mechanisms of binding (Figure 3C). For systematic substitutions, we introduced alanine and valine residues at each site, thereby ablating side chains and substituting a hydrophobic moiety, respectively. To probe disease-associated and evolutionary variants, we introduced mutations from the human bHLH MAX previously observed in tumor samples and made substitutions to residues observed in orthologs across ascomycetes, humans, and *C. elegans* (DeMasi et al., 2011) at the corresponding Pho4 positions. Finally, we tested the effects of altering the electrostatic charge of amino acids on Pho4 binding by substituting charged residues for those with the opposite charge or by substituting uncharged residues for positively charged residues.

After on-chip expression, immobilization, and purification, expressed TFs were visible as high-intensity spots within each reaction chamber in the eGFP channel, while chambers lacking plasmid typically showed no fluorescence (Figure 3D). A small fraction of chambers lacking plasmid yielded observable intensities, providing a sensitive readout of potential cross-contamination between chambers that were used to set a lower threshold for identifying chambers with successful expression. Overall, 216 of 223 mutants (~97%) successfully expressed at least once (Figure 3E), and 205 of 223 mutants (~92%)

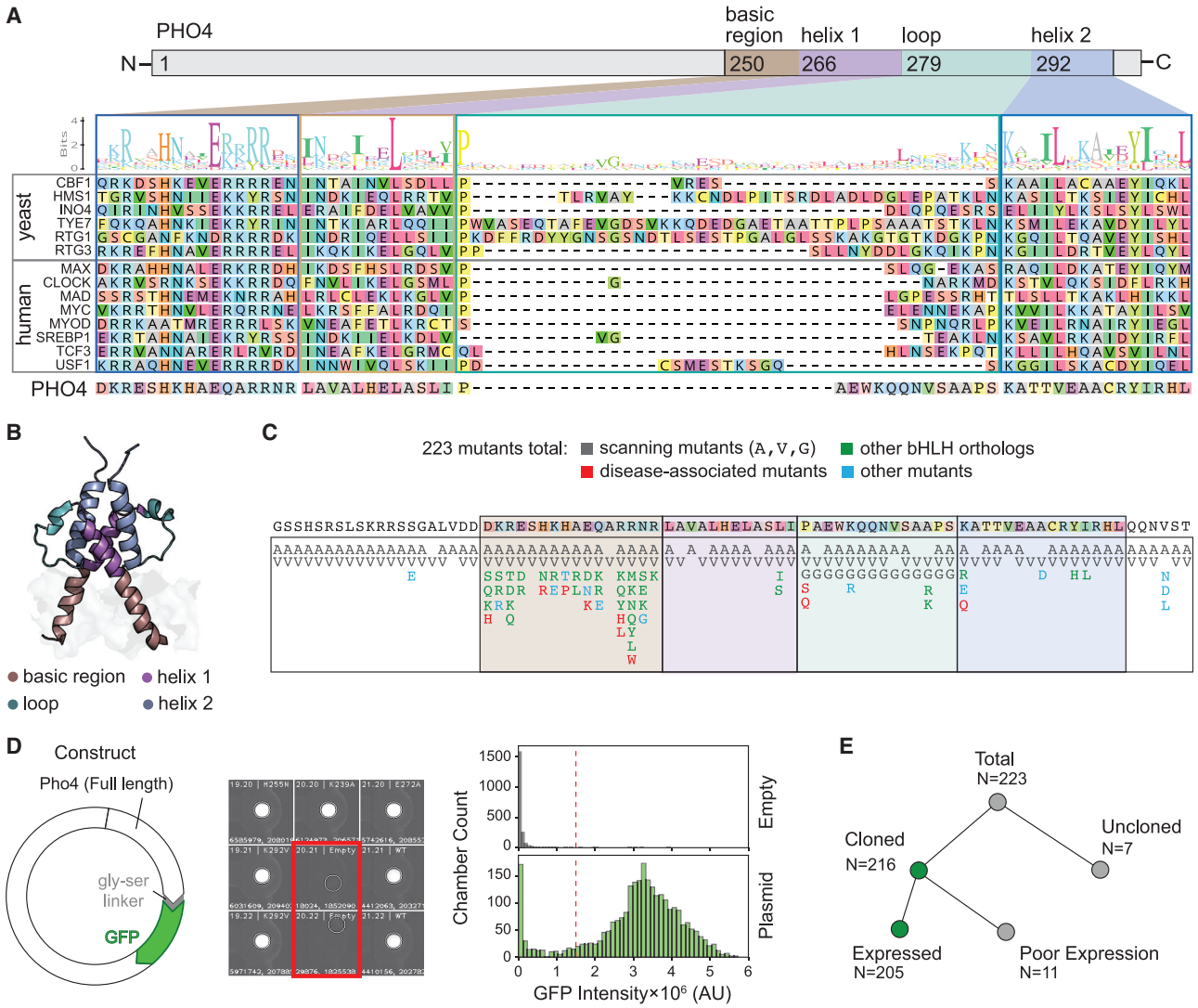

Figure 3. Pho4 Mutant Library Design and Expression

(A) Protein sequence alignment for bHLH proteins across yeast and humans.

(B) Pho4 structure (PDB: 1A0A) with regions within the DNA-binding domain labeled.

(C) Pho4 library mutants categorized by scan, presence in other bHLH proteins, representation in disease variants, and other types of mutations (charge modulation, etc.).

(D) Plasmid map of full-length Pho4 construct fused to C-terminal GFP tag (left), sample image of 9 of 1,568 device chambers showing measured fluorescence intensities for chambers containing Pho4-eGFP plasmid and empty chambers (red) (middle), and measured intensities for all chambers across 3 devices (right). Vertical red dashed line denotes cutoff intensity between positive and no TF expression.

(E) Binary tree summarizing mutant outcomes for all 223 mutants in the library. 216 cloned mutants expressed at least once, of which 205 variants expressed reliably across 26 experiments in this study.

expressed consistently across the 26 experiments in this study (Figure 3E).

Most Mutations throughout Pho4 Have Statistically Significant Effects on DNA Binding

First, we tested which residues contribute to Pho4 DNA binding by quantifying the effects of amino acid mutations on measured binding affinity for 5′-C CACGTG A-3′, a cognate DNA sequence with medium-affinity flanking nucleotides chosen to enhance the ability to observe beneficial and deleterious effects on binding (Le et al., 2018). We generated fluorescently labeled DNA constructs by annealing an Alexa647-labeled primer to a universal sequence at the 3′ end of each DNA and extending constructs using Klenow polymerase fragment (Figure 4A). Measured binding affinities were highly reproducible between experimental replicates (Figure S4), allowing reliable determination of mutations that both increased and decreased affinity relative to wild type Pho4. To estimate affinities for deleterious variants with K_d values above concentrations probed experimentally, we globally fit all binding curves to a Langmuir isotherm with a single shared saturation value and individually fit K_d values (Fordyce et al., 2010, 2012; Nguyen et al., 2019; see STAR Methods and

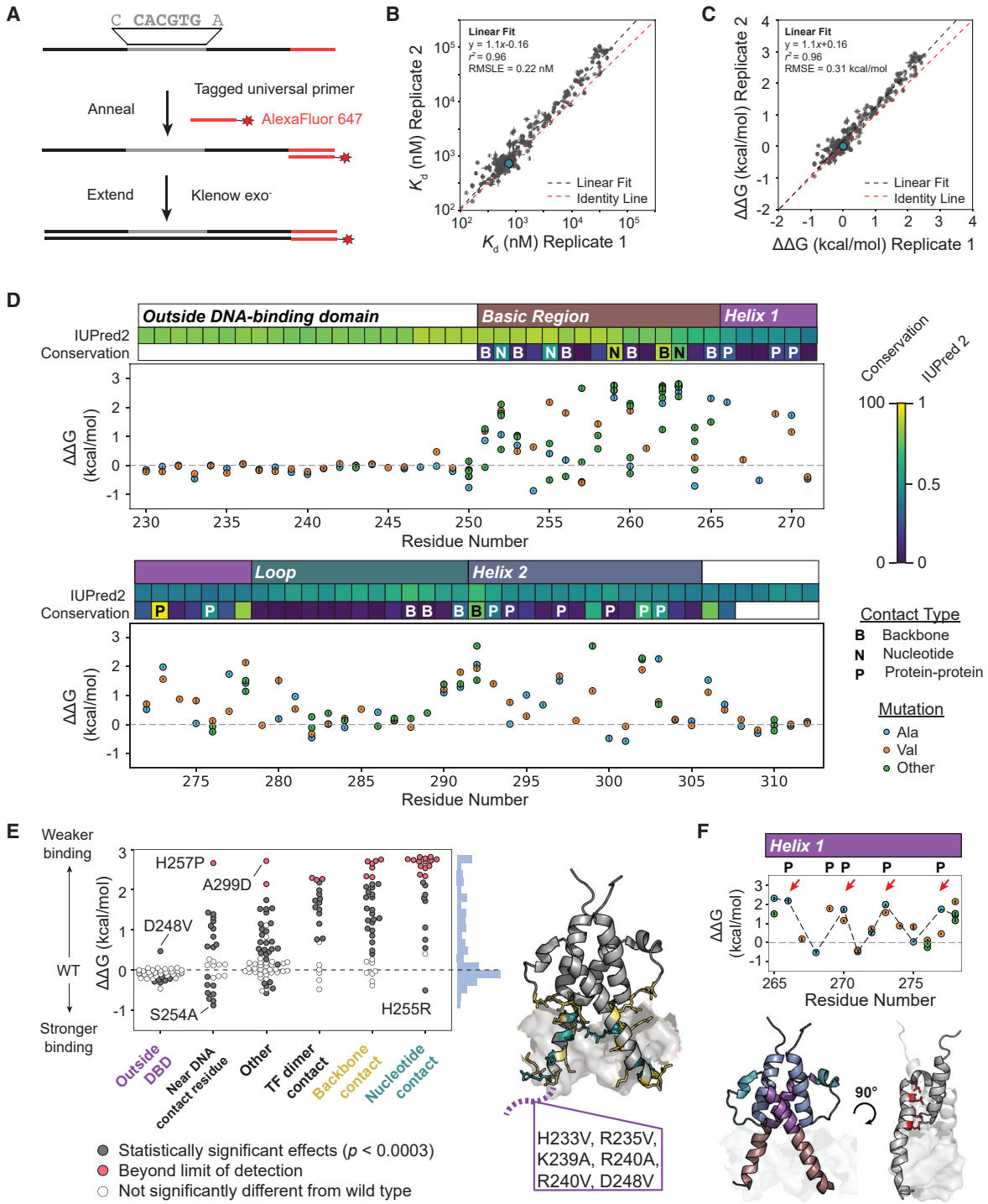

Figure 4. Many Mutations throughout the Pho4 DBD Alter DNA Binding

(A) Workflow for creating fluorescently labeled DNA duplexes for binding assays.

(B) Pairwise comparison of measured K_d values (median ± SEM) for all TF mutants interacting with a 5′-CCACGTGA-3′ sequence assayed across two separate devices (n = 190); wild type Pho4 is shown in blue. Black and red dashed lines indicate a linear regression and the identity line, respectively. Affinity measurements were log-transformed and fitted to a linear model; RMSLE was then calculated from log-transformed values.

(C) Pairwise comparison of measured ΔΔGs (median ± SEM) for Pho4 mutants; wild type Pho4 is shown in blue. Gray and red dashed lines indicate a linear regression and the identity line, respectively.

(D) Median ΔΔG of binding (±SEM) for all Pho4 mutants interacting with a 5′-CCACGTGA-3′ sequence; known crystal structure contacts (Shimizu et al., 1997; Figure S4), amino acid conservation, and IUPred2 score (score > 0.5 is predicted disordered) are shown (Mészáros et al., 2018; Erdős and Dosztányi, 2020).

(legend continued on next page)

Figure S5). We also calculated change in binding energy relative to wild type Pho4 by dividing affinity measurements for each Pho4 mutant by the median affinity of wild type Pho4 and multiplying by the gas constant and temperature, thereby yielding ΔΔG values in kcal/mol. Extracted K_d and ΔΔG values for all mutants across experiments were highly reproducible over an energetic range of ~4 kcal/mol (K_d: r^2 = 0.96, root mean squared log error [RMSLE] = 0.22 nM; ΔΔG: r^2 = 0.96, root mean square error [RMSE] = 0.31 kcal/mol) (Figures 4B, 4C, and S4). We designated mutants with measured ΔΔG values not statistically significantly different (using a two-tailed t-test with a Bonferroni correction) from those for a mutant lacking DNA-binding activity (A299D, which likely disrupts the dimerization interface) as binding-deficient (see STAR Methods, Figures S6 and S7).

A large fraction of mutations to residues within and outside of the DBD had statistically significant effects on DNA binding (~56%), including at positions not in contact with DNA (Figure 4D). As expected, mutating residues outside of the DBD generally had little to no effect, while mutations to the nucleotide- and backbone-contacting residues typically reduced binding to below the limit of detection (Figures 4D and 4E). Despite poor sequence conservation of the bHLH loop region (Figure 3A), mutations to residues in the loop close to either helix 1 or helix 2 had strong effects on binding, likely due to either proximity to the DNA molecule and known backbone-contacting residues or via disruption of essential secondary structure (Figure S8). Although mutations to strongly conserved residues tended to be more deleterious overall (r^2 = 0.41), effects were strongly mutation dependent, with different substitutions at a given position yielding changes in binding affinities that varied by ~2 kcal/mol (Figures S8 and S9). Protein variation effect analyzer (PROVEAN), a computational algorithm designed to predict the functional effects of mutations, was moderately successful at predicting whether mutations with large energetic effects were damaging or benign using a discrete cutoff (area under the curve [AUC] = 0.82); however, the overall correlation between the magnitudes of predicted and observed effects was relatively poor (r^2 = 0.35) (Figure S9). Taken together, these results indicate that, while phylogeny-based algorithms can broadly predict whether a mutation will be benign or damaging (Dong et al., 2015; Reeb et al., 2020), they cannot quantitatively predict effects on TF function upon mutation.

Multiple mutations to residues near DNA contacts and outside of the DNA-binding domain significantly increased DNA affinity, including H255R, which corresponds to a hotspot cancer variant in the human MAX protein (Cerami et al., 2012; Gao et al., 2013; Wang et al., 2017). These results suggest that this particular variant may exact its deleterious effects by increasing nonspecific binding to DNA in the genome. This is also consistent with prior suggestions that TFs are evolutionarily selected to have moderate affinities *in vivo* to enable dynamic transcriptional responses to changing nuclear TF concentrations (Gaudet and Mango, 2002; Wang et al., 2017; Bruno et al., 2019; Kribelbauer et al., 2018) (Figures 4D and 4E). The removal of positively charged residues in the N-terminal intrinsically disordered tail (Figure S10) yielded small but statistically significant increases in DNA-binding affinity, suggesting that charged residues outside the DBD might play a role in DNA binding in Pho4 as reported for other TFs (Vuzman and Levy, 2010, 2012; Shammas, 2017).

Systematic Mutagenesis Coupled to High-Resolution Affinity Measurements Can Reveal Secondary Structure

Many TFs, including bHLHs, include large disordered regions that are thought to assume a folded 3D structure only upon binding DNA and, therefore, pose technical challenges for crystalization. We, therefore, sought to assess whether systematic mutational scans coupled with quantitative affinity measurements could reveal clues regarding secondary structures in the absence of crystal structures or NMR data. Observed periodic effects of mutations within helix 1 mapped to the reference crystal structure (Shimizu et al., 1997) revealed that deleterious mutations lie at the protein dimerization interface while benign mutations can be found at the solvent-exposed exterior (Figure 4F). Moreover, valine substitutions tended to be more deleterious compared with alanine mutations at the DNA interface (likely due to their steric bulk) while alanine substitutions were disfavored compared with valine mutations at the protein-protein interface (likely due to disruptions in hydrophobic packing) (Figure S12). Scanning mutagenesis with amino acid substitutions of varied biochemical properties coupled to high-resolution energetic measurements may, therefore, have utility for guiding computational structural predictions and for explaining mechanisms of residue function within a host protein.

Comparing Effects of TF Mutations across Oligonucleotide Sequences Reveals Residues Involved in Modulating Affinity and Specificity

TF mutations may alter transcriptional regulation by uniformly modulating DNA-binding affinity (i.e., altering affinity to all DNA sequences equally), modulating DNA specificity (i.e., differentially affecting affinity for some DNA sequences), or a combination of the two. To distinguish between affinity and specificity effects, we systematically measured effects of TF mutations on binding to 8 additional DNA sequences comprising single-nucleotide mutations within the core 5′-CACGTG-3′ E-box motif as well as the first flanking nucleotide on either side (Figures 5A and S12–S14). Across all of our devices, K_d measurements are highly reproducible (Figure S15). The RMSE for K_d measurements ranges from 0.2 to 0.5 (based on $\log_{10}$-transformed K_d values in nM), corresponding to affinity differences of 1.5- to 3-fold, with accurate replication of measured values for K_d values up to ~50 μM. For ΔΔG measurements, the calculated RMSE across replicates ranges from 0.2 to 0.4 kcal/mol, with accurate replication of measured ΔΔGs up to 2.5–3.0 kcal/mol. Because measured K_d values were significantly greater than Pho4 concentration in the device (see STAR Methods), K_d measurements remain unchanged

(E) Median ΔΔG of binding for all mutations binned by interaction with DNA based on crystal structure (right) and labeled by statistical difference from wild type Pho4 and background binding. ΔΔGs above 0 kcal/mol indicate weaker binding than wild type Pho4; ΔΔGs below 0 kcal/mol indicate stronger binding than wild type Pho4.

(F) Periodicity of effects on DNA binding (top) and indicated positions on Pho4 crystal structure (bottom). Data reflects median ΔΔG (±SEM) for DNA binding; dashed line passes through alanine mutants.

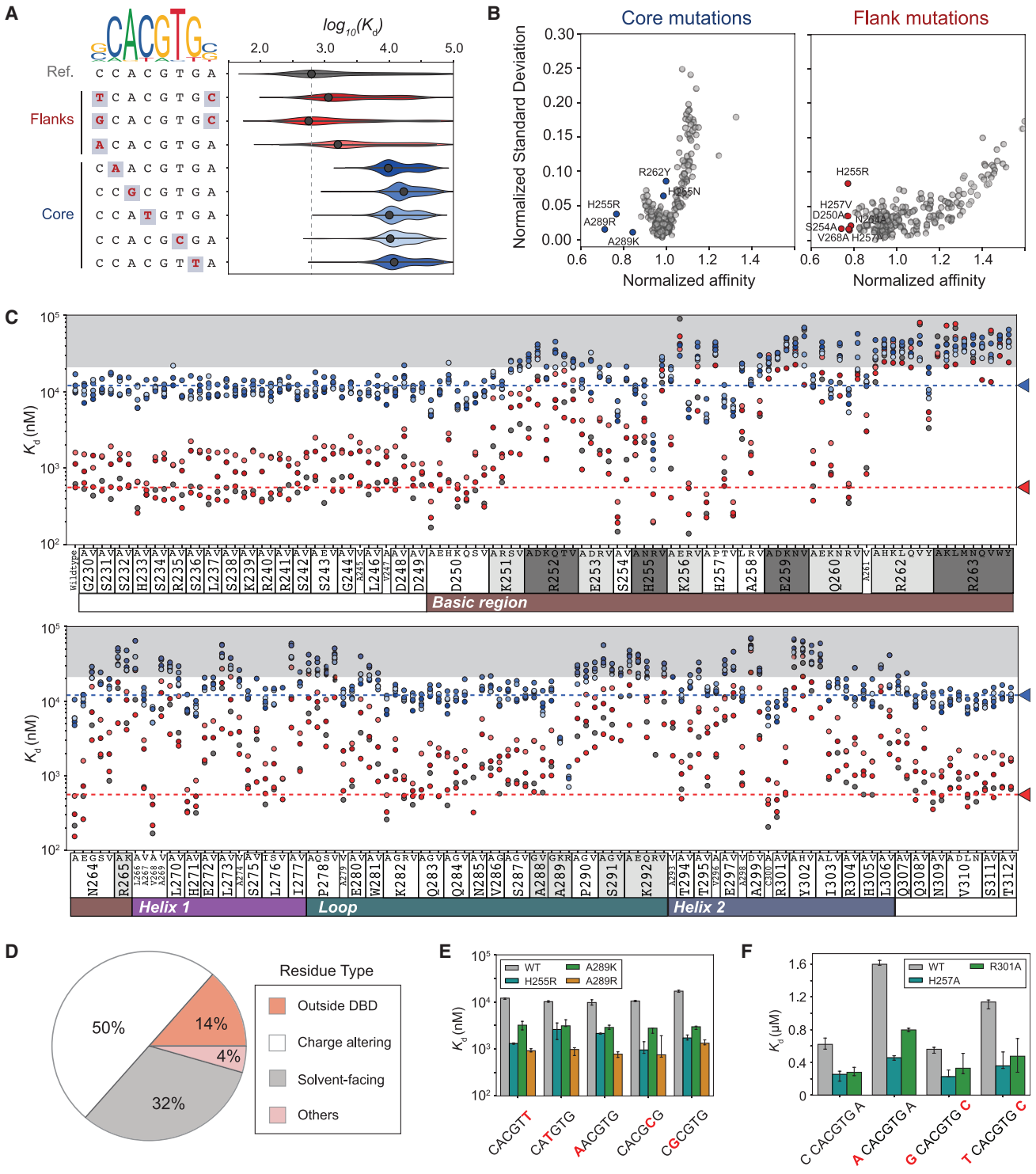

Figure 5. Effects of Pho4 Mutations on DNA Affinity and Specificity

(A) PWM logo and list of DNA sequences studied alongside effects on binding affinity (in nM) for all Pho4 variants studied. Black data points reflect median affinity of wild type Pho4 for DNA sequence; vertical dashed line indicates median affinity of wild type Pho4 for the reference oligo 5′-C CACGTG A-3′.

(B) Normalized standard deviation versus normalized affinities for all Pho4 mutants indicating mutants with effects on affinity and/or specificity.

(C) Measured median binding affinities across experimental replicates for all TF mutations interacting with all oligonucleotides. Blue arrow indicates median wild type Pho4 affinity for the low-affinity 5′-C CACGTT A-3′ sequence; red arrow indicates median wild type Pho4 affinity for the DNA sequence (5′-G CACGTG C-3′). Points are colored by oligo identity, as in Figure 4A.

(legend continued on next page)

even with 2-fold changes in Pho4 available for binding in the assay (Figure S16). In subsequent analyses, we aggregate measurements across all replicates for a Pho4 variant and DNA oligonucleotide and then report the median K_d or ΔΔG values (±SEM) for all replicates over all experiments.

To identify mutants with statistically significant different binding from the wild type Pho4, we performed an independent t-test for all mutants against wild type Pho4 and used a Bonferroni-corrected p-value cutoff (based on a p-value of 0.05) to determine significance. For most oligonucleotide sequences, the false-negative rate ranged between 20%–30%; 5'-C CGCGTG A-3' had a higher false-negative rate, likely due to the overall lower number of replicates present (Figures S13 and S17). Mutations in the core binding site had a slightly higher false-negative rate, likely due to the lower dynamic range, as evidenced by an overall smaller experimentally measured ΔΔG range among Pho4 mutants for those sequences.

Consistent with the known Pho4 position weight matrix (PWM) and a variety of previous reports, we observed that mutations to the core E-box motif significantly reduced affinity and a 5′ C flanking nucleotide was preferred (Fisher and Goding, 1992; Maerkl and Quake, 2007; Le et al., 2018; Spivak and Stormo, 2012). Measured affinities were ~3-fold weaker than seen previously (Maerkl and Quake, 2007), likely due to low levels of nonspecific adsorption of expressed TFs on chamber walls (see STAR Methods); comparisons to other quantitative measurements of Pho4 DNA-binding affinity via EMSA (Cave et al., 2000) showed nearly 10-fold differences in absolute affinity measurements. However, we note that measuring *in vitro* binding affinities are a complex function of salt (Papaneophytou et al., 2014), crowding agents, and assay temperature. Indeed, a prior study of the same DNA sequence using a different technique (circular dichroism [CD] spectroscopy) resulted in K_d measurements that differed nearly an order of magnitude (Cave et al., 2000). In addition, affinity measurements are sensitive to distal sequences outside of the consensus binding site (Afek et al., 2014), which differed among these assays. ΔΔGs are a relative measurement and are, therefore, unaffected.

To identify TF mutants with affinity or specificity effects across multiple DNA sequences, we quantified the spread in measured DNA-binding affinities (standard deviation) normalized by the median affinity of all assayed Pho4 variants for each oligo $log_{10}(K_d)_{i,j}/median(log_{10}(K_d)_j)$, where i is a particular TF mutation and j is a particular oligonucleotide mutation (Figure 5B). Overall, standard deviations increase as measurements diverge toward very high or low affinity (particularly for core mutations), reflecting increased measurement noise toward the dynamic range limits of the assay. For very-low-affinity binders, the fractional uncertainty in K_d values returned by the global fits becomes very large. For very-high-affinity binders, the uncertainty again increases, as there are fewer DNA concentrations measured within the linear binding regime. Several mutants (H255R, A289R, and A289K) increase the median affinity without increasing the standard deviation, likely by positioning positively charged residues in proximity to the negatively charged DNA backbone (Figures 5B and S18). Several mutations to critical DNA-contacting residues, R262Y and H255N, both of which are observed in the phylogenetic record (Kim et al., 1995; Shimizu et al., 1997; del Olmo Toledo et al., 2018; Figure 2A), appeared to increase the variance in measured affinities (see STAR Methods), suggesting that these mutations may primarily alter specificity (Figure 5B).

Measured affinities plotted as a function of mutated residue position for all 1,853 unique TF-DNA mutant pairs reveal several striking trends (Figure 5C). *In vivo*, wild type Pho4 binds both the reference E-box sequence (5′-CACGTG-3′) and a known biologically relevant low-affinity site (5′-CACGTT-3′) (Barbarić et al., 1996; Zhou and O'Shea, 2011). We, therefore, used these values as guidelines for establishing a range of physiologically relevant binding (Figure 5C). For wild type Pho4 and mutations outside of the DBD, changes to less favorable flanking nucleotides or mutations in the core binding site typically reduced affinities by ~4 and ~20-fold, respectively, preserving low-to-medium-affinity binding. For many residues within the DBD (and particularly for those that make direct contacts with DNA), the combined effects of TF and DNA mutations reduced binding to that of the dynamic range floor (Figure 5C). However, a large number of DBD mutants retained the ability to bind oligonucleotides containing flanking sequence mutations with a range of physiologically relevant binding affinities. Overall, 128 of the 151 mutants with altered binding relative to the wild type protein retained the ability to bind at least some oligonucleotides at levels above background. Moreover, some of these mutants have differential effects for different flanking sequences. Thus, combinations of mutations in *cis* and *trans* allow for the generation of large ranges of binding affinities and "tuning" of TF occupancies *in vivo*.

Differences in Electrostatics and Helical Propensity Modulate Binding Affinity

Closer examination of residues that significantly increased DNA-binding affinity revealed that many appeared to introduce an additional positive charge near the DNA (~50%, as for H255R, A289K, and A289R) (Figures 5D, 5E, and S19). However, a large fraction did so without altering charge at DNA-contacting residues, including H257A and R301A (Figures 5D and 5F). Approximately 32% of mutations found to enhance affinity were primarily alanine or valine substitutions at solvent-facing residues (Figures 5D, 6A, and S19), highlighting the role of non-contacting and distal amino acid residues in dictating binding affinity and spurring mechanistic questions regarding how they exert their effects.

Prior studies have revealed that helix 1 of Pho4 and other bHLH TFs are unstructured in the absence of DNA and adopt a primarily helical conformation upon binding cognate DNA (Cave et al., 2000; Sauvé et al., 2004). Prior work has shown that modulating the helical propensity of TF sequences can tune binding affinity for DNA sequences containing the E-box motif by stabilizing the helical conformation of the TF (Kunne and Allemann, 1997; Turner et al., 2004) (Figure 6B). To test if

(D) Proportions of mutations that statistically significantly enhance DNA-binding affinity.
(E) Binding affinities for wild type Pho4 and H255R, A289K, and A289R mutants (median affinity ± SEM).
(F) Binding affinities for Pho4 H257A (helix 1) and R301A (helix 2) interacting with DNA sequences containing flanking nucleotide mutations (median affinity ± SEM).

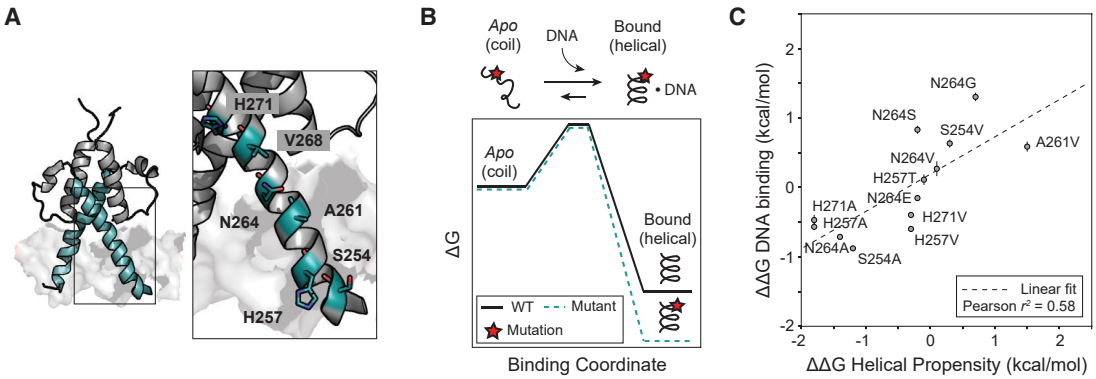

Figure 6. Solvent-Facing Residues Modulate Affinity by Tuning Helical Propensity

(A) Crystal structure of Pho4 with basic region and helix 1 highlighted (cyan); right, inset of solvent-facing residues in this region.

(B) Schematic reaction coordinate diagram for wild type (solid black line) and mutated Pho4 (cyan dashed line) in which the mutant construct has higher helical stability.

(C) Measured change in DNA-binding affinity (ΔΔG, median ± SEM) for the 5′-C CACGTG A-3′ reference oligonucleotide versus previously measured changes in helical propensity for individual residue substitutions (O'Neil and DeGrado, 1990); dashed line indicates linear regression.

changes in helical propensity were sufficient to explain observed differences in measured binding affinity for alanine and valine mutants, we compared measured changes in Gibbs free energy of binding with previously determined changes in Gibbs free energy for helix formation (O'Neil and DeGrado, 1990) for all residues near DNA-contacting residues (Figure 6A) and found that these were highly correlated (r^2 = 0.58; RMSE = 0.70 kcal/mol) (Figure 6C). As expected, measured ΔΔG values for mutations at nucleotide-contacting residues in helical regions were dominated by changes in hydrogen bonding and only weakly correlated with predicted changes in helical propensity (r^2 = 0.27; RMSE = 2.0 kcal/mol; Figure S20A), and mutations to residues in the loop region, which remains unstructured regardless of DNA binding, showed no correlation (r^2 = 0.0089; RMSE = 1.2 kcal/mol; Figure S20B). We observed that distal mutations of amino acid residues to alanine or valine also enhanced affinity and coincided with helical regions in the loop and helix 2 of Pho4. Analysis (Figure S21) only showed minor correlation (r^2 = 0.33) with a helical propensity, likely due to the distance away from the DNA molecule and highly preformed helical content in the absence of DNA (Cave et al., 2000; Sauvé et al., 2004). Together, these results strongly suggest that mutations in helical regions that modulate the equilibrium between unstructured and helical conformations can tune TF binding.

Double-Mutant Cycles across the TF-DNA Interface Can Reveal Intermolecular Interactions Required for Recognition

Beyond simply cataloging effects, this set of 1,853 quantitative affinities provides a unique opportunity to measure the strength of intermolecular interactions across the TF-DNA interface via biochemical double-mutant cycles (Horovitz, 1996; Horovitz et al., 2019). In general, we expect that mutating TF amino acid residue(s) essential for recognizing a particular nucleotide will be relatively less deleterious upon that nucleotide's mutation. As a simplified example, consider a TF that binds a DNA sequence such that residue 1 does not directly contact any nucleotides but residue 2 makes direct contact with nucleotide 2 (Figure 7A). For residue 1, mutating this residue will have the same relative effect on affinity regardless of the oligonucleotide sequence. For residue 2, mutating this residue will significantly reduce binding to the wild type oligonucleotide but have a less deleterious effect for an oligonucleotide in which nucleotide 2 has been mutated. Systematic comparisons of the relative effects on affinity for all TF mutants for each DNA sequence can therefore provide a comprehensive method for revealing functional interactions required for specific recognition and binding.

As the first application of this approach, we compared affinities measured for the Pho4 mutant library interacting with the biologically relevant low-affinity 5′-C CACGTT A-3′ site and the WT reference E-box sequence (5′-C CACGTG A-3′). The crystal structure for Pho4 bound to a DNA duplex containing a 5′-C CACGTG T-3′ suggests a direct contact between the H255 residue and the final G nucleotide within the E-box **(**Figure 7B**, inset)**, predicting that mutating H255 should have differential effects for sequences containing a G or a T at this position. As expected, measured affinities were weaker overall for the mutant DNA sequence, with most mutants having similar effects (Figures 7B, S22, and S23; r^2 = 0.84). However, several mutants were significantly less deleterious for binding the mutated DNA sequence than the cognate DNA sequence, including the expected H255 mutants (H255R, H255N, and H255V), and E259D. Inspection of measured concentration-dependent binding curves confirmed energetic non-additivity for combined TF and DNA mutations (Figures S23D–S23F). Additional observed energetic effects can be explained by previously observed structural contacts; for example, E259 residue contacts the C nucleotide base-paired with the G on the opposite strand. These results, therefore, establish that double-mutant cycles across the TF-DNA interface via STAMMP represent a high-throughput approach for detecting relevant functional interactions required for recognition.

Double-Mutant Cycles Reveal TF Residues Required to Specify Flanking Nucleotide Preferences

For Pho4, preferences for nucleotides flanking the core consensus site play a critical role in dictating *in vivo*

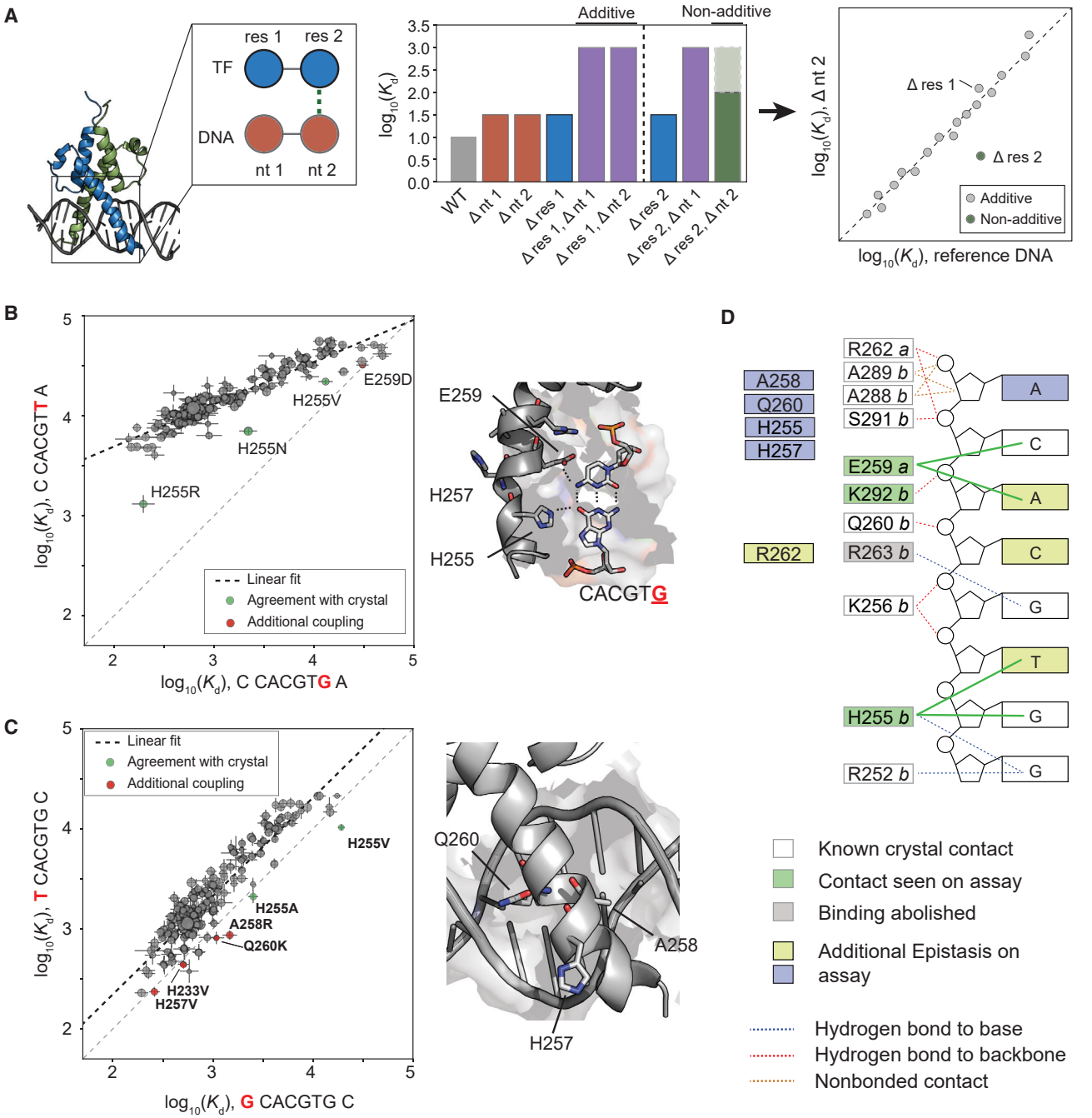

Figure 7. Pairwise Affinity Comparisons Reveal Determinants of Binding Specificity

(A) Example cartoon illustrating how epistasis between Pho4 and DNA mutations can be detected by comparing energetic effects of TF mutations across different DNA sequences.

(B) Pairwise comparison between measured binding affinities ($\log_{10}(K_d)$, median ± SEM) for Pho4 mutants interacting with a low-affinity mutant sequence (5′-C CACGT**T** A-3′) versus the medium-affinity reference sequence (5′-C CACGTG A-3′) (left); inset of crystal structure with outlier TF residues labeled.

(C) Pairwise comparison between measured binding affinities ($\log_{10}(K_d)$, median ± SEM) for 2 DNA sequences with 5′ flanking nucleotide mutations (left); inset of crystal structure indicating residues H257, A258, and Q260 (right).

(D) Comparison between identified energetic couplings identified in this study and known crystallographic contacts.

occupancies, rates of gene activation, and levels of induction (Aow et al., 2013; Gordân et al., 2013; Rajkumar et al., 2013; Le et al., 2018). However, the residues responsible for mediating this specificity remain unknown. While the crystal structure of Pho4 suggested that DNA-contacting residues R252 and H255 mediate specificity (Shimizu et al., 1997), mutagenesis studies

of Pho4 studies have implicated residues outside of the DBD (Fisher and Goding, 1992) and demonstrated that mutations in orthologous TFs corresponding to the Pho4 A258 residue can alter flanking nucleotide specificity (Beltran et al., 2004).

To investigate the origins of flanking nucleotide specificity, we compared measured affinities for a sequence in which the first 5′ flanking nucleotide was mutated to a T (5′-T CACGTG C-3′) with those for a 5′-G CACGTG C-3′ variant (Figures 7C and S24). Although measured affinities for the mutant oligonucleotide were slightly weaker for nearly all mutants, a small set of mutants bound the flanking 5′ T nucleotide more tightly. This set included multiple mutations to H255, consistent with previous findings that this residue helps mediate flanking nucleotide specificity (Shimizu et al., 1997). However, we also detected enhanced binding for the A258R, Q260K, and H257V variants (Shimizu et al., 1997; Beltran et al., 2004) (Figures 7C and S24D–S24F), establishing that mutations within the DBD can alter specificity (Figure 7C). These substitutions include both aliphatic and positively charged residues, suggesting that introducing steric bulk at the DNA interface (such as A to R, and Q to K substitutions) may modulate flanking nucleotide specificity (Fisher and Goding, 1992). H257 is a solvent-facing residue on the same helix as A258 and Q260, suggesting that H257V might alter the conformation of residues A258 and Q260 or the overall helicity of the TF to modulate binding specificity.

Repeating this analysis for mutations throughout the core binding site recapitulated many contacts predicted by the known crystal structure (Figures 7D and S23–S28). For mutations that abolish binding across all oligonucleotides (e.g., mutations at R263 and most backbone-contacting residues) (Figures 7D and S23–S28), double-mutant cycle analysis cannot quantify epistasis; however, these critical contacts are typically easily identified from phylogeny. We observed a case in which a known backbone-contacting residue of Pho4, R262, can affect DNA-binding specificity upon mutation. While backbone-contacting residues have been shown previously to mediate specificity via "indirect readout" mechanisms (De Masi et al., 2011; Gordân et al., 2013; Slattery et al., 2014), we note here that R262Y was the only mutant at either position 262 or 263 still capable of binding DNA. The finding is consistent with phylogenetic data showing that the human bHLH family member SREBP1 contains a tyrosine at the orthologous position and that this mutation enhances conformational flexibility to allow binding to varied E-box sequences (del Olmo Toledo et al., 2018; Párraga et al., 1998; Figure S29). In addition, this analysis identified specificity-altering mutations (e.g., H255N and R262Y) that cannot be predicted from a crystal structure crystalized in the presence of a single DNA sequence. High-throughput thermodynamic measurements can, therefore, complement and supplement traditional structural analysis for identifying macromolecular contacts.

DISCUSSION

Here, we present STAMMP, which enables quantitative measurements of DNA-binding affinities across >1,500 TF variants within a single experiment. Using this system, we measured absolute and relative binding energies for ~210 Pho4 mutants interacting with multiple DNA sequences, including substitutions at positions spanning the core binding site and the 5′ and 3′ flanking nucleotides. In total, 76% (n = 163) of TF mutations led to statistically significant differences in DNA binding; of these, 80% (n = 133) preserved binding above background levels. A large fraction of these residues does not directly contact DNA (either nucleobases or the backbone), suggesting that many poorly conserved positions that were previously unexplored experimentally may play critical roles in specifying and remodeling transcriptional responses.

Mutations in *cis* have long been considered the primary drivers of evolutionary variation (Nelson et al., 2013; Wong et al., 2017), as TF mutations can have pleiotropic effects on the cellular function that limit evolvability and diversification of genetic networks (Signor and Nuzhdin, 2018). These conclusions have been further bolstered by experimental evidence that mutations to DNA-contacting residues or core consensus nucleotides often ablate binding (Maerkl and Quake, 2009; De Masi et al., 2011), creating large fitness penalties that pose evolutionary barriers. Here, the ability to assess many mutations in parallel and measure even subtle differences in affinity suggests that effects of mutations in *trans* could be compensated for by concomitant changes in nucleotides flanking *cis*-regulatory elements to preserve transcriptional responses (Beltran et al., 2004; Rogers and Bulyk, 2018). In addition, the observation that mutations may stabilize helical conformations to promote DNA binding suggests that these residues could allow the formation of permissive binding intermediates (Bloom et al., 2010; Gong et al., 2013; Jalal et al., 2020; McKeown et al., 2014; Starr et al., 2017). The higher affinity binding of these permissive binding intermediates could allow TFs to acquire and accommodate additional TF or DNA mutations that would otherwise reduce binding to non-physiological levels, making otherwise inaccessible evolutionary trajectories feasible.

Obtaining structures for TFs is often technically challenging because many TFs assume a folded conformation only upon interacting with a consensus binding site and contain large, intrinsically disordered domains. Reflecting this, of 1,639 predicted TFs in the human genome, only 185 (~11%) have crystal structures available Lambert et al., 2018b. Of these structures, most are solely composed of the DBD alone and are crystallized only in the presence of a single high-affinity DNA sequence. STAMMP can provide critical functional information about residues within intrinsically disordered regions previously shown to be important for DNA binding and dynamic protein-DNA recognition (Vuzman and Levy, 2012; Shammas, 2017; Ferreiro et al., 2008; Fuxreiter et al., 2011). Moreover, the ability to return quantitative affinity measurements for multiple oligonucleotide sequences provides critical information required to probe the mechanistic origins of specificity and extract energetic information from crystalized structures (Farrel et al., 2016).

The experimental difficulty of quantitatively assaying effects of protein mutations has led to the development of various computational algorithms that use combinations of phylogeny (Ng and Henikoff, 2003; Hopf et al., 2017; Choi et al., 2012), structure (Adzhubei et al., 2010; Blanco et al., 2018), and prior experimental measurements (Pelossof et al., 2015) to predict mutational effects on DNA binding. While these computational models have shown some success in predicting if particular disease-associated mutations ablate DNA binding, our

comparisons between computational predictions and experimental data further reinforce that these algorithms' abilities to produce quantitative predictions of mutational effects are modest and typically underestimate effects of mutations to poorly conserved, non-contacting residues (Miller et al., 2017; Reeb et al., 2020). In future work, we anticipate that STAMMP datasets may serve as critical resources for testing, revising, and refining computational algorithms. Furthermore, systematic studies of TFs at this resolution may reveal context dependencies for effects of TF mutations and mechanisms by which sequence variation within structurally related TFs give rise to differences in sequence preference (Berger et al., 2008; Salisbery et al., 2012).

Within the cell nucleus, TF-DNA interaction affinities over a wide physiological range precisely specify transcriptional programs (Farley et al., 2015; Kribelbauer et al., 2019; Le et al., 2018), and even subtle decreases or increases to affinity can alter transcription rate and disrupt overlying genetic circuits (Gaudet and Mango, 2002; Meinhardt et al., 2013; Farley et al., 2015; Crocker et al., 2016; Wang et al., 2017; Bhimsaria et al., 2018; Le et al., 2018; Nishizaki et al., 2020). For most mutations attempting to recapitulate disease-associated human variants, binding affinity was reduced to background levels as previously reported (Wang et al., 2017). However, one mutant designed to mimic disease-associated orthologs (H255R) increased DNA-binding affinity across a broad spectrum of DNA sequences, suggesting that enhanced affinity may drive disease by altering transcriptional programs. This observation is consistent with prior studies suggesting that TF affinities must be appropriately tuned for function, that very-high-affinity DNA-binding sites can be statistically significantly underrepresented within genomes (Le et al., 2018), and that TF sequences are evolved for submaximal binding strength (Bruno et al., 2019). Moreover, these results imply that, in some cases, appropriate therapeutic interventions could attempt to disrupt (rather than restore) binding.

In future work, the ability to express and functionally characterize hundreds of TF mutants in a single experiment at low cost enables a wide variety of precision medicine applications. STAMMP could be used to systematically assess the effects of disease-associated TF variants, thereby providing an additional high-throughput method for assessing functional consequences of variants of unknown significance (Gasperini et al., 2016; Matreyek et al., 2018; Federici and Soddu, 2020). STAMMP could also be extended toward testing compounds for their potential to drug TFs and serve as new cancer therapeutics (Struntz et al., 2019; Lambert et al., 2018a).

STAR★METHODS

Detailed methods are provided in the online version of this paper and include the following:

- KEY RESOURCES TABLE
- RESOURCE AVAILABILITY
  - Lead Contact
  - Materials Availability
  - Data and Code Availability
- METHOD DETAILS
  - Mold and Device Fabrication
  - Pho4 Structural Examination
  - Prediction of Intrinsically Disordered Tail
  - High-Throughput QuikChange Mutagenesis
  - QuikChange Mutagenesis
  - Plasmid Array Printing
  - Preparation of Fluorescently-Labeled dsDNA for Binding Assays:
  - Double-Stranded DNA Preparation and Dilution
  - Microscopy Instrumentation
  - On-Chip Surface Patterning:
  - Surface Patterning
  - On-chip TF Expression and Purification
  - DNA Binding Measurements
- QUANTIFICATION AND STATISTICAL ANALYSIS
  - Image Processing and Quantitation
  - Quality Control and Binding Curve Generation
  - Determining Statistical Significance from Wildtype Pho4 & from Background
  - Predicting Likely Effects from Phylogeny
  - Identifying 'Affinity' and 'Specificity' Mutants
  - Helical Propensity Analysis
  - Double-Mutant Cycle Analysis

SUPPLEMENTAL INFORMATION

Supplemental Information can be found online at https://doi.org/10.1016/j.cels.2020.11.012.

ACKNOWLEDGMENTS

P.M.F. acknowledges the support of an Alfred P. Sloan Foundation fellowship and is a Chan Zuckerberg Biohub Investigator. A.K.A. and N.D. acknowledge the support of the National Science Foundation (GRFP, grant number DGE-1656518). A.K.A. also acknowledges support from the ChEM-H Chemistry/Biology Interface (CBI) Predoctoral Training program. C.J.M. was supported by a Canadian Institutes of Health Research (CIHR) Postdoctoral Fellowship. D.A.M. acknowledges support from the Stanford MSTP program and a Stanford Interdisciplinary Graduate Fellowship (SIGF, Anonymous Donor) affiliated with Stanford ChEM-H. The authors thank Scott Longwell for experimental pipeline assistance and Kara Brower for microfluidic mold fabrication. We thank Connor Horton and Michael Hayes for critical feedback on the manuscript.

AUTHOR CONTRIBUTIONS

Conceptualization, A.K.A. and P.M.F.; Formal Analysis, A.K.A. and P.M.F.; Investigation, A.K.A. and N.D.; Resources, A.K.A., C.J.M., and D.A.M.; Writing – Original Draft: A.K.A. and P.M.F.; Writing – Review & Editing, all authors. Supervision & Funding Acquisition: P.M.F.

DECLARATION OF INTERESTS

P.M.F. is a member of the Advisory Board of *Cell Systems*.

Received: June 24, 2020
Revised: August 8, 2020
Accepted: November 24, 2020
Published: December 18, 2020

REFERENCES

Aditham, A.K., Shimko, T.C., and Fordyce, P.M. (2018). BET-seq: binding energy topographies revealed by microfluidics and high-throughput sequencing. Methods Cell Biol. *148*, 229–250.

Adzhubei, I.A., Schmidt, S., Peshkin, L., Ramensky, V.E., Gerasimova, A., Bork, P., Kondrashov, A.S., and Sunyaev, S.R. (2010). A method and server for predicting damaging missense mutations. Nat. Methods *7*, 248–249.

Afek, A., Schipper, J.L., Horton, J., Gordân, R., and Lukatsky, D.B. (2014). Protein−DNA binding in the absence of specific base-pair recognition. Proc. Natl. Acad. Sci. USA *111*, 17140–17145.

Aow, J.S.Z., Xue, X., Run, J.Q., Lim, G.F.S., Goh, W.S., and Clarke, N.D. (2013). Differential binding of the related transcription factors Pho4 and Cbf1 can tune the sensitivity of promoters to different levels of an induction signal. Nucleic Acids Res *41*, 4877–4887.

Barbarić, S., Münsterkötter, M., Svaren, J., and Hörz, W. (1996). The homeodomain protein Pho2 and the basic-Helix-Loop-Helix protein Pho4 bind DNA cooperatively at the yeast PHO5 promoter. Nucleic Acids Res *24*, 4479–4486.

Barrera, L.A., Vedenko, A., Kurland, J.V., Rogers, J.M., Gisselbrecht, S.S., Rossin, E.J., Woodard, J., Mariani, L., Kock, K.H., Inukai, S., et al. (2016). Survey of variation in human transcription factors reveals prevalent DNA binding changes. Science *351*, 1450–1454.

Beltran, A.C., Dawson, P.E., and Gottesfeld, J.M. (2004). Role of DNA sequence in the binding specificity of synthetic basic-helix-loop-helix domains. ChemBioChem. *6*, 104–113.

Berger, M.F., Badis, G., Gehrke, A.R., Talukder, S., Philippakis, A.A., Peña-Castillo, L., Alleyne, T.M., Mnaimneh, S., Botvinnik, O.B., Chan, E.T., et al. (2008). Variation in homeodomain DNA binding revealed by high-resolution analysis of sequence preferences. Cell *133*, 1266–1276.

Bhimsaria, D., Rodríguez-Martínez, J.A., Pan, J., Roston, D., Korkmaz, E.N., Cui, Q., Ramanathan, P., and Ansari, A.Z. (2018). Specificity landscapes unmask submaximal binding site preferences of transcription factors. Proc. Natl. Acad. Sci. USA *115*, E10586–E10595.

Blanco, J.D., Radusky, L., Climente-González, H., and Serrano, L. (2018). FoldX accurate structural protein–DNA binding prediction using PADA1 (protein assisted DNA assembly 1). Nucleic Acids Res. *46*, 3852–3863.

Bloom, J.D., Gong, L.I., and Baltimore, D. (2010). Permissive secondary mutations enable the evolution of influenza oseltamivir resistance. Science *328*, 1272–1275.

Brower, K., Puccinelli, R.R., Markin, C.J., Shimko, T.C., Longwell, S.A., Cruz, B., and Gomez-Sjoberg, R. (2018). An open-source, programmable pneumatic setup for operation and automated control of single- and multi-layer microfluidic devices. HardwareX *3*, 117–134.

Brownlie, P., Ceska, T., Lamers, M., Romier, C., Stier, G., Teo, H., and Suck, D. (1997). The crystal structure of an intact human Max–DNA complex: new insights into mechanisms of transcriptional control. Structure *5*, 509–520.

Bruno, L., Ramlall, V., Studer, R.A., Sauer, S., Bradley, D., Dharmalingam, G., Carroll, T., Ghoneim, M., Chopin, M., Nutt, S.L., et al. (2019). Selective deployment of transcription factor paralogs with submaximal strength facilitates gene regulation in the immune system. Nat. Immunol. *20*, 1372–1380.

Cave, J.W., Kremer, W., and Wemmer, D.E. (2000). Backbone dynamics of sequence specific recognition and binding by the yeast Pho4 bHLH domain probed by NMR. Protein Sci. *9*, 2354–2365.

Cerami, E., Gao, J., Dogrusoz, U., Gross, B.E., Sumer, S.O., Aksoy, B.A., Jacobsen, A., Byrne, C.J., Heuer, M.L., Larsson, E., et al. (2012). The cBio cancer genomics portal: an open platform for exploring multidimensional cancer genomics data. Cancer Discov. *2*, 401–404.

Chen, D., Orenstein, Y., Golodnitsky, R., Pellach, M., Avrahami, D., Wachtel, C., Ovadia-Shochat, A., Shir-Shapira, H., Kedmi, A., Juven-Gershon, T., et al. (2016). SELMAP - SELEX affinity landscape MAPping of transcription factor binding sites using integrated microfluidics. Sci. Rep. *6*, 33351.

Chen, M., and Lopes, J.M. (2007). Multiple basic helix-loop-helix proteins regulate expression of the ENO1 gene of Saccharomyces cerevisiae. Eukaryot. Cell *6*, 786–796.

Choi, Y., and Chan, A.P. (2015). PROVEAN web server: a tool to predict the functional effect of amino acid substitutions and indels. Bioinformatics *31*, 2745–2747.

Choi, Y., Sims, G.E., Murphy, S., Miller, J.R., and Chan, A.P. (2012). Predicting the functional effect of amino acid substitutions and indels. PLoS One *7*, e46688.

Cock, P.J.A., Antao, T., Chang, J.T., Chapman, B.A., Cox, C.J., Dalke, A., Friedberg, I., Hamelryck, T., Kauff, F., Wilczynski, B., and de Hoon, M.J.L. (2009). Biopython: freely available Python tools for computational molecular biology and bioinformatics. Bioinformatics *25*, 1422–1423.

Crocker, J., Noon, E.P., and Stern, D.L. (2016). The soft touch: low-affinity transcription factor binding sites in development and evolution. Curr. Top. Dev. Biol. *117*, 455–469.

De Masi, F., Grove, C.A., Vedenko, A., Alibés, A., Gisselbrecht, S.S., Serrano, L., Bulyk, M.L., and Walhout, A.J.M. (2011). Using a structural and logics systems approach to infer bHLH–DNA binding specificity determinants. Nucleic Acids Res. *39*, 4553–4563.

del Olmo Toledo, V., Puccinelli, R., Fordyce, P.M., and Pérez, J.C. (2018). Diversification of DNA binding specificities enabled SREBP transcription regulators to expand the repertoire of cellular functions that they govern in fungi. PLoS Genet. *14*, e1007884.

Dong, C., Wei, P., Jian, X., Gibbs, R., Boerwinkle, E., Wang, K., and Liu, X. (2015). Comparison and integration of deleteriousness prediction methods for nonsynonymous SNVs in whole exome sequencing studies. Hum. Mol. Genet. *24*, 2125–2137.

Edelstein, A.D., Tsuchida, M.A., Amodaj, N., Pinkard, H., Vale, R.D., and Stuurman, N. (2014). Advanced methods of microscope control using μManager software. J. Biol. Methods *1*, e11.

Erdős, G., and Dosztányi, Z. (2020). Analyzing protein disorder with IUPred2A. Curr. Protoc. Bioinformatics *70*, e99.

Farley, E.K., Olson, K.M., Zhang, W., Brandt, A.J., Rokhsar, D.S., and Levine, M.S. (2015). Suboptimization of developmental enhancers. Science *350*, 325–328.

Farrel, A., Murphy, J., and Guo, J.T. (2016). Structure-based prediction of transcription factor binding specificity using an integrative energy function. Bioinformatics *32*, i306–i313.

Federici, G., and Soddu, S. (2020). Variants of uncertain significance in the era of high-throughput genome sequencing: a lesson from breast and ovary cancers. J. Exp. Clin. Cancer Res. *39*, 46.

Ferreiro, D.U., Sánchez, I.E., and de Prat Gay, G. (2008). Transition state for protein-DNA recognition. Proc. Natl. Acad. Sci. USA *105*, 10797–10802.

Fisher, F., and Goding, C.R. (1992). Single amino acid substitutions alter helix-loop-helix protein specificity for bases flanking the core CANNTG motif. EMBO J. *11*, 4103–4109.

Foat, B.C., Morozov, A.V., and Bussemaker, H.J. (2006). Statistical mechanical modeling of genome-wide transcription factor occupancy data by MatrixREDUCE. Bioinformatics *22*, e141–e149.

Fordyce, P.M., Gerber, D., Tran, D., Zheng, J., Li, H., DeRisi, J.L., and Quake, S.R. (2010). De novo identification and biophysical characterization of transcription-factor binding sites with microfluidic affinity analysis. Nat. Biotechnol. *28*, 970–975.

Fordyce, P.M., Pincus, D., Kimmig, P., Nelson, C.S., El-Samad, H., Walter, P., and DeRisi, J.L. (2012). Basic leucine zipper transcription factor Hac1 binds DNA in two distinct modes as revealed by microfluidic analyses. Proc. Natl. Acad. Sci. USA *109*, E3084–E3093.

Fuxreiter, M., Simon, I., and Bondos, S. (2011). Dynamic protein–DNA recognition: beyond what can be seen. Trends Biochem. Sci. *36*, 415–423.

Gao, J., Aksoy, B.A., Dogrusoz, U., Dresdner, G., Gross, B., Sumer, S.O., Sun, Y., Jacobsen, A., Sinha, R., Larsson, E., et al. (2013). Integrative analysis of complex cancer genomics and clinical profiles using the cBioPortal. Sci. Signal. *6*, pl1.

Gasperini, M., Starita, L., and Shendure, J. (2016). The power of multiplexed functional analysis of genetic variants. Nat. Protoc. *11*, 1782–1787.

Gaudet, J., and Mango, S.E. (2002). Regulation of organogenesis by the Caenorhabditis elegans FoxA protein PHA-4. Science *295*, 821–825.

Geertz, M., Shore, D., and Maerkl, S.J. (2012). Massively parallel measurements of molecular interaction kinetics on a microfluidic platform. Proc. Natl. Acad. Sci. USA *109*, 16540–16545.

Gertz, J., and Cohen, B.A. (2009). Environment-specific combinatorial cis-regulation in synthetic promoters. Mol Syst Biol *5*, https://doi.org/10.1038/msb.2009.1.

Gong, L.I., Suchard, M.A., and Bloom, J.D. (2013). Stability-mediated epistasis constrains the evolution of an influenza protein. eLife *2*, e00631.

Gordân, R., Shen, N., Dror, I., Zhou, T., Horton, J., Rohs, R., and Bulyk, M.L. (2013). Genomic regions flanking E-box binding sites influence DNA binding specificity of bHLH transcription factors through DNA shape. Cell Rep. *3*, 1093–1104.

Hopf, T.A., Ingraham, J.B., Poelwijk, F.J., Schärfe, C.P.I., Springer, M., Sander, C., and Marks, D.S. (2017). Mutation effects predicted from sequence co-variation. Nat. Biotechnol. *35*, 128–135.

Horovitz, A. (1996). Double-mutant cycles: a powerful tool for analyzing protein structure and function. Fold. Des. *1*, R121–R126.

Horovitz, A., Fleisher, R.C., and Mondal, T. (2019). Double-mutant cycles: new directions and applications. Curr. Opin. Struct. Biol. *58*, 10–17.

Jalal, A.S.B., Tran, N.T., Stevenson, C.E., Chan, E.W., Lo, R., Tan, X., Noy, A., Lawson, D.M., and Le, T.B.K. (2020). Diversification of DNA-binding specificity by permissive and specificity-switching mutations in the ParB/Noc protein family. Cell Rep. *32*, 107928.

Jarmoskaite, I., AlSadhan, I., Vaidyanathan, P.P., and Herschlag, D. (2020). How to measure and evaluate binding affinities. eLife *9*, e57264.

Jolma, A., Kivioja, T., Toivonen, J., Cheng, L., Wei, G., Enge, M., Taipale, M., Vaquerizas, J.M., Yan, J., Sillanpää, M.J., et al. (2010). Multiplexed massively parallel SELEX for characterization of human transcription factor binding specificities. Genome Res. *20*, 861–873.

Kim, H.D., and O'Shea, E.K. (2008). A quantitative model of transcription factor–activated gene expression. Nat. Struct. Mol. Biol. *15*, 1192–1198.

Kim, J.B., Spotts, G.D., Halvorsen, Y.D., Shih, H.M., Ellenberger, T., Towle, H.C., and Spiegelman, B.M. (1995). Dual DNA binding specificity of ADD1/SREBP1 controlled by a single amino acid in the basic helix-loop-helix domain. Mol. Cell. Biol. *15*, 2582–2588.

Kribelbauer, J.F., Rastogi, C., Bussemaker, H.J., and Mann, R.S. (2019). Low-affinity binding sites and the transcription factor specificity paradox in eukaryotes. Annu. Rev. Cell Dev. Biol. *35*, 357–379.

Künne, A.G.E., and Allemann, R.K. (1997). Covalently linking BHLH subunits of MASH-1 increases specificity of DNA binding. Biochemistry *36*, 1085–1091.

Lambert, M., Jambon, S., Depauw, S., and David-Cordonnier, M.H. (2018a). Targeting transcription factors for cancer treatment. Molecules *23*, 1479.

Lambert, S.A., Jolma, A., Campitelli, L.F., Das, P.K., Yin, Y., Albu, M., Chen, X., Taipale, J., Hughes, T.R., and Weirauch, M.T. (2018b). The human transcription factors. Cell *172*, 650–665.

Laskowski, R.A., Jabłońska, J., Pravda, L., Vařeková, R.S., and Thornton, J.M. (2018). PDBsum: structural summaries of PDB entries. Protein Sci. *27*, 129–134.

Le, D.D., Shimko, T.C., Aditham, A.K., Keys, A.M., Longwell, S.A., Orenstein, Y., and Fordyce, P.M. (2018). Comprehensive, high-resolution binding energy landscapes reveal context dependencies of transcription factor binding. Proc. Natl. Acad. Sci. USA *115*, E3702–E3711.

Lee, T.I., and Young, R.A. (2013). Transcriptional regulation and its misregulation in disease. Cell *152*, 1237–1251.

Luscombe, N.M., Laskowski, R.A., and Thornton, J.M. (1997). NUCPLOT: a program to generate schematic diagrams of protein-nucleic acid interactions. Nucleic Acids Res. *25*, 4940–4945.

Maerkl, S.J., and Quake, S.R. (2007). A systems approach to measuring the binding energy landscapes of transcription factors. Science *315*, 233–237.

Maerkl, S.J., and Quake, S.R. (2009). Experimental determination of the evolvability of a transcription factor. Proc. Natl. Acad. Sci. USA *106*, 18650–18655.

Matreyek, K.A., Starita, L.M., Stephany, J.J., Martin, B., Chiasson, M.A., Gray, V.E., Kircher, M., Khechaduri, A., Dines, J.N., Hause, R.J., et al. (2018). Multiplex assessment of protein variant abundance by massively parallel sequencing. Nat. Genet. *50*, 874–882.

Maurano, M.T., Humbert, R., Rynes, E., Thurman, R.E., Haugen, E., Wang, H., Reynolds, A.P., Sandstrom, R., Qu, H., Brody, J., et al. (2012). Systematic localization of common disease-associated variation in regulatory DNA. Science *337*, 1190–1195.

McKeown, A.N., Bridgham, J.T., Anderson, D.W., Murphy, M.N., Ortlund, E.A., and Thornton, J.W. (2014). Evolution of DNA specificity in a transcription factor family produced a new gene regulatory module. Cell *159*, 58–68.

Meinhardt, S., Manley, M.W., Parente, D.J., and Swint-Kruse, L. (2013). Rheostats and toggle switches for modulating protein function. PLoS One *8*, e83502.

Mészáros, B., Erdős, G., and Dosztányi, Z. (2018). IUPred2A: context-dependent prediction of protein disorder as a function of redox state and protein binding. Nucleic Acids Res. *46*, W329–W337.

Miller, M., Bromberg, Y., and Swint-Kruse, L. (2017). Computational predictors fail to identify amino acid substitution effects at rheostat positions. Sci. Rep. *7*, 41329.

Mitsis, T., Efthimiadou, A., Bacopoulou, F., Vlachakis, D., Chrousos, G., and Eliopoulos, E. (2020). Transcription factors and evolution: an integral part of gene expression (Review). World Acad. Sci. J. *2*, 3–8.

Nelson, C.S., Fuller, C.K., Fordyce, P.M., Greninger, A.L., Li, H., and DeRisi, J.L. (2013). Microfluidic affinity and ChIP-seq analyses converge on a conserved FOXP2-binding motif in chimp and human, which enables the detection of evolutionarily novel targets. Nucleic Acids Res. *41*, 5991–6004.

Ng, P.C., and Henikoff, S. (2003). SIFT: predicting amino acid changes that affect protein function. Nucleic Acids Res. *31*, 3812–3814.

Nguyen, H.Q., Roy, J., Harink, B., Damle, N.P., Latorraca, N.R., Baxter, B.C., Brower, K., Longwell, S.A., Kortemme, T., Thorn, K.S., et al. (2019). Quantitative mapping of protein-peptide affinity landscapes using spectrally encoded beads. eLife *8*, e40499.

Nishizaki, S.S., Ng, N., Dong, S., Porter, R.S., Morterud, C., Williams, C., Asman, C., Switzenberg, J.A., and Boyle, A.P. (2020). Predicting the effects of SNPs on transcription factor binding affinity. Bioinformatics *36*, 364–372.

Nutiu, R., Friedman, R.C., Luo, S., Khrebtukova, I., Silva, D., Li, R., Zhang, L., Schroth, G.P., and Burge, C.B. (2011). Direct measurement of DNA affinity landscapes on a high-throughput sequencing instrument. Nat. Biotechnol. *29*, 659–664.

O'Neil, K.T., and DeGrado, W.F. (1990). A thermodynamic scale for the helix-forming tendencies of the commonly occurring amino acids. Science *250*, 646–651.

Ogawa, N., DeRisi, J., and Brown, P.O. (2000). New components of a system for phosphate accumulation and polyphosphate metabolism in Saccharomyces cerevisiae revealed by genomic expression analysis. Mol. Biol. Cell *11*, 4309–4321.

Papaneophytou, C.P., Grigoroudis, A.I., McInnes, C., and Kontopidis, G. (2014). Quantification of the effects of ionic strength, viscosity, and hydrophobicity on protein–ligand binding affinity. ACS Med. Chem. Lett. *5*, 931–936.

Párraga, A., Bellsolell, L., Ferré-D'Amaré, A.R., and Burley, S.K. (1998). Co-crystal structure of sterol regulatory element binding protein 1a at 2.3 Å resolution. Structure *6*, 661–672.

Pelossof, R., Singh, I., Yang, J.L., Weirauch, M.T., Hughes, T.R., and Leslie, C.S. (2015). Affinity regression predicts the recognition code of nucleic acid–binding proteins. Nat. Biotechnol. *33*, 1242–1249.

Persikov, A.V., Wetzel, J.L., Rowland, E.F., Oakes, B.L., Xu, D.J., Singh, M., and Noyes, M.B. (2015). A systematic survey of the Cys2His2 zinc finger DNA-binding landscape. Nucleic Acids Res. *43*, 1965–1984.

Rajkumar, A.S., Dénervaud, N., and Maerkl, S.J. (2013). Mapping the fine structure of a eukaryotic promoter input-output function. Nat. Genet. *45*, 1207–1215.

Reeb, J., Wirth, T., and Rost, B. (2020). Variant effect predictions capture some aspects of deep mutational scanning experiments. BMC Bioinformatics *21*, 107.

Rogers, J.M., and Bulyk, M.L. (2018). Diversification of transcription factor-DNA interactions and the evolution of gene regulatory networks. Wiley Interdiscip. Rev. Syst. Biol. Med. *10*, e1423.

Sailsbery, J.K., Atchley, W.R., and Dean, R.A. (2012). Phylogenetic analysis and classification of the fungal bHLH domain. Mol. Biol. Evol. *29*, 1301–1318.

Sauvé, S., Tremblay, L., and Lavigne, P. (2004). The NMR solution structure of a mutant of the Max b/HLH/LZ free of DNA: insights into the specific and reversible DNA binding mechanism of dimeric transcription factors. J. Mol. Biol. *342*, 813–832.

Schindelin, J., Arganda-Carreras, I., Frise, E., Kaynig, V., Longair, M., Pietzsch, T., Preibisch, S., Rueden, C., Saalfeld, S., Schmid, B., et al. (2012). Fiji: an open-source platform for biological-image analysis. Nat. Methods *9*, 676–682.

Segal, E., Raveh-Sadka, T., Schroeder, M., Unnerstall, U., and Gaul, U. (2008). Predicting expression patterns from regulatory sequence in Drosophila segmentation. Nature *451*, 535–540.

Shammas, S.L. (2017). Mechanistic roles of protein disorder within transcription. Curr. Opin. Struct. Biol. *42*, 155–161.

Shimizu, T., Toumoto, A., Ihara, K., Shimizu, M., Kyogoku, Y., Ogawa, N., Oshima, Y., and Hakoshima, T. (1997). Crystal structure of PHO4 bHLH domain-DNA complex: flanking base recognition. EMBO J. *16*, 4689–4697.

Signor, S.A., and Nuzhdin, S.V. (2018). The evolution of gene expression in cis and trans. Trends Genet. *34*, 532–544.

Slattery, M., Zhou, T., Yang, L., Dantas Machado, A.C., Gordân, R., and Rohs, R. (2014). Absence of a simple code: how transcription factors read the genome. Trends Biochem. Sci. *39*, 381–399.

Spivak, A.T., and Stormo, G.D. (2012). ScerTF: a comprehensive database of benchmarked position weight matrices for Saccharomyces species. Nucleic Acids Res. *40*, D162–D168.

Starr, T.N., Picton, L.K., and Thornton, J.W. (2017). Alternative evolutionary histories in the sequence space of an ancient protein. Nature *549*, 409–413.

Struntz, N.B., Chen, A., Deutzmann, A., Wilson, R.M., Stefan, E., Evans, H.L., Ramirez, M.A., Liang, T., Caballero, F., Wildschut, M.H.E., et al. (2019). Stabilization of the Max homodimer with a small molecule attenuates Myc-driven transcription. Cell Chem. Biol. *26*, 711–723.e14.

Thorn, K. (2014). Shading correction of fluorescence images. http://nic.ucsf.edu/blog/2014/01/shading-correction-of-fluorescence-images/.

Turner, E.C., Cureton, C.H., Weston, C.J., Smart, O.S., and Allemann, R.K. (2004). Controlling the DNA binding specificity of bHLH proteins through intramolecular interactions. Chem. Biol. *11*, 69–77.

Untergasser, A., Cutcutache, I., Koressaar, T., Ye, J., Faircloth, B.C., Remm, M., and Rozen, S.G. (2012). Primer3—new capabilities and interfaces. Nucleic Acids Res *40*, e115.

Voronova, A., and Baltimore, D. (1990). Mutations that disrupt DNA binding and dimer formation in the E47 helix-loop-helix protein map to distinct domains. Proc. Natl. Acad. Sci. USA *87*, 4722–4726.

Vuzman, D., and Levy, Y. (2010). DNA search efficiency is modulated by charge composition and distribution in the intrinsically disordered tail. Proc. Natl. Acad. Sci. USA *107*, 21004–21009.

Vuzman, D., and Levy, Y. (2012). Intrinsically disordered regions as affinity tuners in protein–DNA interactions. Mol. BioSyst. *8*, 47–57.

Wang, D., Hashimoto, H., Zhang, X., Barwick, B.G., Lonial, S., Boise, L.H., Vertino, P.M., and Cheng, X. (2017). MAX is an epigenetic sensor of 5-carboxylcytosine and is altered in multiple myeloma. Nucleic Acids Res. *45*, 2396–2407.

Weirauch, M.T., Cote, A., Norel, R., Annala, M., Zhao, Y., Riley, T.R., Saez-Rodriguez, J., Cokelaer, T., Vedenko, A., Talukder, S., et al. (2013). Evaluation of methods for modeling transcription factor sequence specificity. Nat. Biotechnol. *31*, 126–134.

Wong, E.S., Schmitt, B.M., Kazachenka, A., Thybert, D., Redmond, A., Connor, F., Rayner, T.F., Feig, C., Ferguson-Smith, A.C., Marioni, J.C., et al. (2017). Interplay of cis and trans mechanisms driving transcription factor binding and gene expression evolution. Nat. Commun. *8*, 1092.

Zacharias, D.A., Violin, J.D., Newton, A.C., and Tsien, R.Y. (2002). Partitioning of lipid-modified monomeric GFPs into membrane microdomains of live cells. Science *296*, 913–916.

Zhao, Y., and Stormo, G.D. (2011). Quantitative analysis demonstrates most transcription factors require only simple models of specificity. Nat. Biotechnol. *29*, 480–483.

Zhou, X., and O'Shea, E.K. (2011). Integrated approaches reveal determinants of genome-wide binding and function of the transcription factor Pho4. Mol. Cell *42*, 826–836.

Zykovich, A., Korf, I., and Segal, D.J. (2009). Bind-n-Seq: high-throughput analysis of in vitro protein–DNA interactions using massively parallel sequencing. Nucleic Acids Res. *37*, e151.

STAR★METHODS

KEY RESOURCES TABLE

REAGENT or RESOURCE	SOURCE	IDENTIFIER
Antibodies		
Goat polyclonal Anti-GFP Antibody (Biotin)	Abcam	Cat#ab6658; RRID: AB_305631
Bacterial and Virus Strains		
NEB 5-alpha Competent *E. coli*	New England Biolabs	C2987I
Chemicals, Peptides, and Recombinant Proteins		
NEBuffer 2	New England Biolabs	B7002S
Trizma hydrochloride	Sigma Life Science	T3253-500G
NaCl, BioUltra	Sigma Life Science	71376-1KG
UltraPure BSA	ThermoFisher	AM2618
Biotinylated BSA	ThermoFisher Pierce	29130
NeutrAvidin	Thermo Scientific	31000
Phosphate Buffered Saline (10X)	Corning	46-013-CM
Bovine Serum Albumin (Heat shock fraction)	Sigma Life Science	B4287-25G
Trehalose Dihydrate	Sigma Life Science	T9531-25G
Klenow fragment, exo-	In-house stock	N/A
Critical Commercial Assays		
PURExpress *In Vitro* Protein Synthesis Kit	New England Biolabs	E6800L
RNAsin Ribonuclease Inhibitor	Promega	N2515
TrypLE	ThermoFisher	12604-013
Deposited Data		
Raw binding measurements, analytical code	This paper	https://doi.org/10.17605/OSF.IO/8QRZP
Oligonucleotides		
Primers for Binding assays, see Table 1 (Methods)	This paper	N/A
Recombinant DNA		
Plasmid: PURExpress Pho4-monomeric eGFP fusion	This paper	N/A
Software and Algorithms		
Biopython	Cock et al., 2009	https://biopython.org/
Fiji	Schindelin et al., 2012	https://imagej.net/Fiji
ImageStitcher	This paper, Github	https://github.com/FordyceLab/ImageStitcher
ProcessingPack	This paper, Github	https://github.com/FordyceLab/ProcessingPack-STAMMP
RunPack	This paper, Github	https://github.com/FordyceLab/RunPack-STAMMP
PROVEAN	Choi et al., 2012, 2015	http://provean.jcvi.org/index.php
μManager	Edelstein, et al., 2014	https://micro-manager.org/

RESOURCE AVAILABILITY

Lead Contact

Further information and requests for resources and reagents should be directed to and will be fulfilled by the Lead Contact, Polly Fordyce (pfordyce@stanford.edu).

Materials Availability

Plasmids generated in this study are available upon request to the lead contact.

Data and Code Availability

Source Data

Raw binding affinity measurements and data for all supplemental binding curves have been deposited at Open Science Framework (DOI: 10.17605/OSF.IO/8QRZP). Accessory data (eg. PROVEAN results, conservation calculations, helical propensity information) are available in the ''Accessory Data'' subfolder within the ''Information for Aggregate Analysis'' folder.

Original code is publicly available at the Open Science Framework (OSF: https://doi.org/10.17605/OSF.IO/8QRZP) under the ''Raw Code'' Folder. Automation software associated with experimental and microscopy setups is located at https://github.com/FordyceLab/RunPack-STAMMP. Software for processing images is available at https://github.com/FordyceLab/ImageStitcher. Analytical software is available at https://github.com/FordyceLab/ProcessingPack-STAMMP. Use of other software is described in the STAR Methods section.

The scripts used to generate the figures reported in this paper are available at (OSF: https://doi.org/10.17605/OSF.IO/8QRZP) under the ''Raw Code'' Folder. Names of files indicate source code and scripting for generating pertinent figures.

Any additional information required to reproduce this work is available from the Lead Contact.

METHOD DETAILS

Mold and Device Fabrication

Flow and control molding masters were fabricated as described previously (Fordyce et al., 2012; Le et al., 2018). Two-layer microfluidic devices were then cast from these molds using polydimethylsiloxane (PDMS) polymer (RS Hughes, RTV615). Control layers of the microfluidic device (Figure S1, orange) were generated by pouring 60 grams of PDMS (1:5 ratio of cross-linker to base) onto the molds, degassing to remove all air in a vacuum chamber under vacuum for ~45 minutes, and baking for 40 minutes at 80°C in a convection oven. After this step, control layers for each device were cut out and removed from the wafer and the fluid line inlets were punched using a catheter hole punch (SYNEO, CR0350255N20R4) mounted onto a drill press (Technical Innovations). The flow layer (Figure S1, blue/green) was generated by spin-casting PDMS (1:20 ratio of cross-linker to polymer) onto the molds at 266 rpm for 10 sec, followed by 1750-1850 rpm for 75 seconds. Layers were relaxed on a flat surface for 10 minutes at room temperature prior to baking at 80°C for 40 minutes in an oven. Cut and punched device control layers were then aligned to flow layers remaining on master molds manually using a stereoscope. Aligned devices were then baked for 40 minutes at 80 °C in an oven, excised from the molds using a scalpel, and the remaining flow-layer fluidics inlets made using the same catheter punch as above.

Pho4 Structural Examination

Categorization of Residues by Interaction with DNA

DNA backbone and nucleotide contacts for Pho4 (Figure S4) were inferred from the available crystal structure (Shimizu et al., 1997; PDB: 1A0A). To identify other residues likely making hydrogen-bonded contacts with DNA, we used NUCPLOT interpretations of the crystal structure (Luscombe et al., 1997) to cross-validate. Based on these, we considered residues 251, 253, 256, 260, 265, 288, 289, 291, and 292 as backbone-contacting; residues 252, 255, 259, and 263 were considered nucleotide-contacting.

To identify residues responsible for Pho4 homodimerization, we examined the crystal structure and the PDBSum protein-protein contact map (Laskowski et al., 2018). Based on this contact map, we identified residues 266, 293, 270, 276, 269, 294, 297, 302, 303, 300, 273 as protein-protein contact residues.

We categorized residues as ''near DNA contact residue'' if they were within 12 amino acids (in linear sequence space) of a DNA-contacting residue within the Pho4 primary sequence. We identified residues 250, 254, 257, 258, 261, 264, 265, 287, and 290 in this category.

Finally, we categorized residues 230-249 and 307-312 as lying outside of the DNA-binding domain based on the Pho4's domain annotation from UniProt. Other residues which did not fit into these categories were categorized as ''other.''

Prediction of Intrinsically Disordered Tail

To predict the intrinsic disorder of the Pho4 DNA binding domain and N-terminal residues preceding the DNA-binding domain, we used the IUPred2A algorithm (Mészáros et al., 2018; Erdős and Dosztányi, 2020). We analyzed the entirety of the Pho4 reading frame using the default IUPred2 long disorder setting and analyzed data using the IUPred scores returned by the program. For this analysis, we considered scores above 0.5 as being disordered as previously noted (Erdős and Dosztányi, 2020).

High-Throughput QuikChange Mutagenesis

Pho4 Plasmid

Prior to Pho4 mutant library generation, we generated a version of the PURExpress control expression plasmid (containing a T7 promoter and an ampicillin selectable marker) in which we inserted the full coding sequence for WT Pho4 fused to a C-terminal monomeric GFP tag (Zacharias et al., 2002) with an intervening gly-ser linker (GGGSGGGGSG). This insertion was sequence-validated via Sanger sequencing and all subsequent mutagenesis used this sequence as a plasmid template.

Primer Design

Mutagenic primers were designed using an in-house automated script (https://github.com/FordyceLab/designQuikChangePrimers). Briefly, the program takes as input a list of desired mutations (e.g. "H255R" for His 255 to Arg mutation) and the protein ORF sequence. For each desired mutation, the script generates different primer candidates by varying the primer length and the position of the mutation site relative to the center of the primer. Candidates were scored using heuristics based on the manufacturer's recommendations included in the QuikChange (Agilent) protocol. First, we selected the mutagenic codon requiring the smallest number of nucleotide mismatches. Next, we calculated the primer scores as follows: (1) we calculated the annealing temperature (T_m) according to the formula given in the QuikChange manual and scored primers such that a maximum score of 2 was given for $78 \leq Tm < 82^{\circ}C$ and this score linearly decreased (with slope=1) for each 1°C change outside this range; (2) we added an additional score of 1 for a G-C base pair at the 5' or the 3' end; (3) we subtracted between 0.25 and 1 if the primer was predicted to have 3' self-complementarity, depending on the degree of predicted self-complementary; (4) we subtracted 0.25 from the score if the first two 5' or 3' bases were the same, to minimize the risk of slippage at the ends; (5) we penalized primer candidates longer than 38 bp (as long as Tm was > 79°C) to reduce oligo synthesis costs; and (6) we calculated predicted primer hairpin temperatures using the primer3-py 'calcHairpin' function (Untergasser et al., 2012) and performed an additional round of optimization if the primer had a predicted hairpin with melting temperature >50°C to decrease this melting temperature, if possible. The final primer was chosen based on the highest cumulative score. Additional details regarding primer optimization calculations are available in the Github repository. Optimized primers were subsequently ordered from IDT (Integrated DNA Technologies) at the 10 nmol synthesis scale in a 96-well plate format with standard desalting purification. These primers were normalized at 6 nmol per well with forward and reverse primers encoding mutations premixed in each well and shipped dry.

QuikChange Mutagenesis

Primers were resuspended in 120 μL of Milli-Q H_2O and left at room temperature to allow primers to solubilize for approximately 1 hour, creating working stock solutions of 50 μM for downstream PCR. Using a 96-channel manual pipettor (Liquidator, Rainin), we added 5 μL of solubilized primers to 195 μL of Milli-Q water to dilute to a working concentration of 1.25 μM and mixed well by pipetting up and down. Finally, we transferred 6 μL of these diluted primers to a new 96-well plate before adding QuikChange reaction Master Mix to all wells (as described below).

We prepared the QuikChange master mix (Agilent Technologies, New England Biolabs) by scaling the single reaction recipe as necessary and keeping on ice prior to use:

Per Single Reaction

14 μL deionized H_2O (*e.g.* Milli-Q H_2O)

2.5 μL 10× Pfu buffer (AD)
0.25-μL Plasmid template (100 ng/μL)
1.25 μL DMSO (5% v/v)
0.5 μL dNTPs (final concentration: 200 μM)
0.5 μL Pfu turbo polymerase (AD) (0.05 Units)
6 μL Forward and Reverse primers (300 nM)

After preparation of the Master Mix, we added 19 μL of this Master Mix into each well using a multichannel pipette and mixed well. We then sealed plates with foil, centrifuged briefly, and placed them into the thermocycler for the PCR reaction according to manufacturer's protocols (Agilent QuikChange Manual).

Next, we treated reactions with Dpn1 enzyme (New England Biolabs, R0176L) to digest any remaining WT plasmid. To do this, we took 10 μL of the above mutagenesis reaction, and added 10 μL of Dpn1 reaction mix (1 μL Dpn1, 2 μL CutSmart Buffer, and 7 μL deionized H_2O). These reactions were well-mixed via pipetting and incubated on a thermocycler with the following protocol.

37°C, 3 hrs
80°C, 20 min
4°C, hold

We then used 1 μL of each reaction to transform 5 μL of *E. coli* DH5α cells (New England Biolabs, C2987I). The cells and PCR product were left on ice for 30 minutes, heat-shocked at 42°C for 30 seconds, and recovered in 300 μL SOC Medium (NEB, B9020S) for 1 hour prior to plating on LB agar plates supplemented with ampicillin (100 μg/mL). Plates were kept at 37°C overnight to grow colony transformants. Single colonies from these plates were then picked and grown at 37°C in 6–8 mL of LB medium supplemented with ampicillin (100 μg/mL) overnight; plates were subsequently stored at 4 °C in case additional colonies need to be picked. We miniprepped plasmids using Qiagen miniprep reagents and validated proper mutagenesis via Sanger sequencing. Colonies were re-picked if the sequencing revealed a wildtype Pho4 clone, an errant mutation elsewhere in the construct, or poor sequencing quality. In cases where no transformants appeared after the mutagenesis reaction, we repeated QuikChange reactions with manually designed primers.

Plasmid Array Printing

Prior to printing, we transferred 10 μL of the plasmid solution from each well of the 96 well to 2 different wells within 384 well plates (Thermo Scientific, AB-1055) using a Biomek FX Automated Workstation (Beckman Coulter, model A31843), recording plasmid

locations to map mutants to chambers in downstream experiments. To standardize well volumes, we then evaporated all wells within the 384 well plates to dryness and re-solubilized in 12–15 μL of print solution formulated as follows:

1% (10 mg/mL) Bovine Serum Albumin (Sigma Life Science, B4287-25G)

200mM (11.65mg/mL) NaCl (Sigma Life Science, 71376-1KG)

12mg/mL trehalose dihydrate (Sigma Life Science, T9531-25G)

These ingredients were combined and dissolved in Milli-Q H2O and filter sterilized prior to use (Millipore, SE1M179M6). When not in use, we stored the print solution and plates with plasmids at 4°C. For longer term storage, we sealed plasmid plates with foil and stored at -20°C.

Prior to printing, all plates were defrosted at 4°C overnight and then centrifuged at 4°C (2000g for 10 minutes). We arrayed plasmids onto epoxysilane-coated 2"x3" glass slides (Thermo Scientific, UCSF2X3-C50-20) using a custom built microarrayer outfitted with silicon pins (Parallel Synthesis Technologies, SMT-S75). To prevent contamination of DNA during prints, pins were washed twice in near-boiling water for 10 seconds, followed by vacuum drying for 8 seconds. After arrays dried overnight, we aligned fabricated PDMS devices onto printed plasmid arrays such that each plasmid spot was isolated in its own unique chamber within the device. Devices were then bonded to the glass slides by baking for 4–12 hours at 95°C on a hotplate (Torrey Pines Scientific) prior to running experiments.

Preparation of Fluorescently-Labeled dsDNA for Binding Assays:

DNA Sequences Studied

All DNA sequences were designed with a universal complementary 3′ region to allow annealing of a single 5′ AlexaFluor-647-conjugated DNA primer to all sequences (calculated T_m of this annealing was 37°C) (STAR Methods Table).

Name	Full Sequence (5’ to 3’)
CCACGTGA	CAATACACTGTTATC AGACC CAC GTG ACGAG CTACTCGTTCGGTTA TCCGGCGGTATGAC
TCACGTGC	CAATACACTGTTATC AGACT CACG TG CCGAG CTACTCGTTCGGTTATC CGGCGGTATGAC
ACACGTGA	CAATACACTGTTATC AGACA CACG TG ACGAG CTACTCGTTCGGTTAT CCGGCGGTATGAC
GCACGTGC	CAATACACTGTTATC AGACG CACG TG CCGAG CTACTCGTTCGGTTAT CCGGCGGTATGAC
CAACGTGA	CAATACACTGTTATC AGACC AAC GTG ACGAG CTACTCGTTCGGTT ATCCGGCGGTATGAC
CCGCGTGA	CAATACACTGTTATC AGACC CGC GTG ACGAG CTACTCGTTCGGTT ATCCGGCGGTATGAC
CCATGTGA	CAATACACTGTTATC AGACC CAT GTG ACGAG CTACTCGTTCG GTTATCCGGCGGTATGAC
CCACGCGA	CAATACACTGTTATC AGACC CAC GCG ACGAG CTACTCGTTCGGTTA TCCGGCGGTATGAC
CCACGTTA	CAATACACTGTTATC AGACC CAC GTT ACGAG CTACTCGTTCGGTT ATCCGGCGGTATGAC
“Universal”	AlexaFluor-647-5’-GTCATACCGCCGGA-3’

STAR Methods Table. DNA oligonucleotide sequences used in these experiments. For each sequence, the 8 bp TF consensus site is shown in bold, the single nucleotide variant is underlined, and the universal 3’ sequence used for annealing a 5’ Alexa-647-conjugated sequence is shown in italics.

Double-Stranded DNA Preparation and Dilution

We ordered nearly all DNA sequences as a single strand from Integrated DNA Technologies (IDT) with standard desalting purification and 'LabReady' formulation (100 μM in IDTE buffer, pH = 8.0); for several oligonucleotides ordered dry, we resuspended the oligonucleotide in Milli-Q H_2O to a final concentration of 100 μM (confirmed using a DeNovix instrument). We then converted these ssDNA sequences to fluorescently-labeled double-stranded DNA via: (1) annealing of a universal 5'-AlexaFluor-647-labeled primer to all sequences, and (2) extension using Klenow fragment, exo-. To minimize variation in measured fluorescence intensities between runs, we prepared fresh labeled dsDNA on the day of each experiment.

To begin annealing and extension reactions, we defrosted NEBuffer 2 (New England Biolabs, B7002S) and dNTPs (100 mM, Thermo Scientific) and kept them on ice. Next, we prepared two annealing reactions, formulated as follows:

12 μL single-stranded DNA (100mM)
12 μL "Universal" primer (100uM)
12 μL dNTP mixture (4 mM)
4 μL NEBuffer 2 (10x stock)

We then performed the annealing reaction using the following protocol on a thermocycler:

94°C, 3 min
Cool to 37°C over 45 minutes

To extend the annealed universal primer, we removed the tubes from the thermocycler, spun them down using a centrifuge, added the following, and mixed well via pipetting:

8 μL of Milli-Q H_2O
1 μL of NEBuffer 2 (10x stock)
1 μL of Klenow enzyme (made in-house)

The tubes were then placed back in the thermocycler for the extension step of the protocol:

37°C, 60 min
80°C, 20 min
10°C, hold

After the extension step, we again centrifuged the tubes using a table-top microcentrifuge and placed them on ice. To remove any aggregates that could clog the microfluidic channels on the device, we sterile filtered reactions with a 0.45um filter spin column (Merck Millipore, UFC30HVNB). Finally, we equilibrated dsDNA reactions in the final assay buffer (10mM Tris-HCl, 100mM NaCl, 1mM DTT, pH 7.5; aliquoted and filtered using 0.45 μM Steriflip vacuum (Millipore, SE1M179M6) using 10K filter spin concentrator columns (Amicon Ultra, UFC501096). To do this, we added 100 μL of the duplexing reaction in the filter spin concentrator, added 200 μL of assay buffer (~300 μL total volume), and spun down to concentrate back to 100 μL via centrifugation (8000-9000g for 8 minutes); this process was repeated 5 times. After the final step, we eluted the DNA by inverting the filter into the collection tube and centrifuging at 3000g for 5 minutes.

For each DNA concentration series, we serially diluted this eluent 1:2 in assay buffer supplemented with 50 μg/mL of UtraPure BSA (ThermoFisher, AM2618) to yield effective final concentrations of ~5 μM, ~2.5 μM, ~600nM, ~300 nM, ~160nM, ~90 nM. For DNA sequences containing mutations in the core binding site, we modified this concentration series to include slightly higher maximum DNA concentrations (~ 7.5 μM, ~ 4 μM, ~ 2 μM, ~ 400 nM, ~ 200 nM, ~40 nM). We noted that addition of UltraPure BSA did not result in changes in affinity. We then calibrated fluorescence intensity to effective DNA concentration by using a DeNovix instrument to measure the absorbance at 260 nm.

Microscopy Instrumentation

We performed all measurements on a Nikon Ti-S Microscope with a motorized XY stage (Applied Scientific Instrumentation, MS-2000 XYZ stage), cMOS camera (Oxford Instruments, Andor Zyla 4.2 CMOS), and solid-state light source (Lumencor, Sola SE Light Engine). We programmed the microscope to perform a gridded acquisition of the device using MicroManager (Edelstein et al., 2014). This grid was set using a 10% overlap between imaging fields for image stitching (described in Analysis), and all images were collected using a 4X objective lens using a 2x2 bin setting.

On-Chip Surface Patterning:

Device Connections for Reagent Introduction

To introduce reagents onto the microfluidic device, reagents were loaded via syringe suction into Tygon tubing (Saint-Gobain, AAD04103) connected to a syringe at one end using a 23-gauge luer connector (McMaster-Carr, 75165A684) and fitted with a blunt-ended steel pin at the other (0.013 in ID x 0.025 in OD x 0.5 in length, New England Small Tube Corporation, NE-1310-02). After loading reagents into the syringe, we inserted the blunt-ended steel pin into the appropriate device port, removed the other end of the Tygon from the Luer-fitted syringe (Brower et al., 2018), and connected the tubing directly to a custom pneumatic manifold that drives fluid flow via positive pressure (Brower et al., 2018). All pneumatic control valves were actuated using a custom automated pneumatic control manifold (Brower et al., 2018) controlled using an in-house python software package (https://github.com/FordyceLab/RunPack).

Surface Patterning

Device surfaces were functionalized with surface-immobilized antibody largely as previously described (Aditham et al., 2018; Le et al., 2018); however, we included a few modifications. First, valve lines controlling the ''button'', ''sandwich'', and ''neck'' valves (Figure S1) were pressurized with 550mM NaCl in Milli-Q H_2O to prevent premature solubilization of the DNA spots by osmotic balancing of fluids between the pneumatic control and reagent flow channels. All other control lines were pressurized with Milli-Q H_2O. Second, we controlled all pneumatic valves on the device at a pressure ranging from 35-37 psi and introduced reagents at pressures of 3.5-4 psi.

To begin antibody patterning, we first dead-end filled all device control lines. Next, we flowed biotinylated BSA (2 mg/mL, ThermoFisher Pierce, 29130) to expel all air from device flow layers by opening the inlet and outlet valves; to expel any remaining air bubbles from the flow channels, we closed the outlet valve after 2-3 minutes and continued to apply pressure to dead-end fill the device for an additional 5-10 minutes. After all air bubbles were expelled, we opened the outlet valve to allow reagent flow, and introduced 2 mg/mL biotinylated BSA for an additional 5 minutes with the ''button'' valves pressurized and then for 30 minutes with the ''button'' valves open. Next, we flushed the device with phosphate buffered saline (10X stock, Corning, 46-013-CM; diluted to 1X in Milli-Q H_2O) for 10 minutes. We then introduced neutravidin (1 mg/mL, Thermo Scientific, 31000) for 30 minutes with ''button'' valves opened, followed by another PBS wash for 10 minutes. To passivate all device surfaces except those protected by the ''button'' valves, we the pressurized the ''button'' valves and introduced biotinylated BSA again for 30 minutes, thereby coating device surfaces and preventing non-specific antibody binding. After an additional 10 minute PBS wash, we introduced biotinylated anti-GFP antibody (100 ug/mL, Abcam, ab6658) into the device for 2 minutes with the ''button'' valves pressurized (to ensure antibody was evenly distributed throughout the device) and then opened ''button'' valves and flowed for an additional 13 minutes and 20 seconds, thereby specifically recruiting biotinylated anti-GFP antibodies to exposed neutravidin-coated surfaces beneath ''button'' valves (Figure 2). Finally, we washed the device with PBS for 10 minutes. Upon conclusion of these steps, we stored the device with the "button'' valves pressurized, the outlet valve shut and the PBS inlet valve open. A light PBS flow kept the device from drying out; we typically completed surface chemistry the night before an experimental assay.

On-chip TF Expression and Purification

On-chip TF Expression

After surface patterning, we expressed all TF variants on the device using the PURExpress *in vitro* transcription/translation system (New England Biolabs, E6800L). First, we combined PURExpress components A (10 μL) & B (7.5 μL) off-chip, mixed gently per the manufacturer's instructions via pipetting, and stored the reaction on ice for 45 minutes, which we observed increased expression yields. After this, we added 1.5 μL of RNAsin (Promega, N2515) and Milli-Q water or DNAse-free water (Promega) to 25 μL. A single 25 μL PURExpress reaction was sufficient for expression on a single device; for multiple devices, we scaled this reaction master mix as necessary.

After incubation, we flowed PURExpress through flow channels for 10 minutes with the ''neck'' and ''button'' valves closed and the ''sandwich'' valve open to completely fill all channels. After this period, we closed the outlet valve, opened the ''neck'' valves, and closed the ''sandwich'' and ''button'' valves to push PURExpress into the plasmid compartments. To ensure that each plasmid compartment was fully filled with PURExpress, we again opened the ''button'' and ''sandwich'' valves with the outlet valve closed and continued flowing PURExpress for an additional 2-3 minutes. To begin protein expression, we then opened the ''neck'' valves (to allow protein expression in the entire chamber), closed the ''sandwich'' valves and ''button'' valves (thereby isolating adjacent chambers from one another and protecting the antibody-coated surface), and placed the device on a preheated hot plate (Torrey Pines Scientific) at 37°C for 45 minutes. To allow GFP to fold and mature, we then removed the device from the hot plate and incubated at room temperature for an additional 2 hours. Finally, we opened the ''button'' valves to allow expressed GFP-tagged TFs to bind patterned anti-GFP antibodies on the slide surface beneath the ''button'' valves. During this step, we mounted the device on a Nikon Ti-S microscope (described above) and periodically imaged using gridded acquisition imaging software to monitor build-up of GFP intensity over time.

On-chip TF Purification

After allowing TF binding to proceed for 2 hours, we again closed the ''neck'' valve (to sequester the plasmid compartment from the reaction compartment), closed the ''button'' valve (to protect surface-immobilized TFs from flow-induced shear, opened the ''sandwich'' valves, and washed with PBS for 10 minutes to wash away any non-specifically bound TF proteins, thereby purifying TFs within each chamber. To remove TF proteins non-specifically adsorbed to device walls, we additionally washed with TrypLE (1X stock, ThermoFisher, 12604-013) for 15 minutes, washed with 2 mg/mL biotinylated BSA for 15 minutes to re-passify device walls, and finally washed with PBS for 10 minutes. After this step, we removed all reagent lines except for PBS and washed the inlet manifold with PBS for 10 minutes to remove trace amounts of trypsin that could otherwise damage proteins during the assay.

DNA Binding Measurements

After on-chip recombinant protein expression and purification, we prepared the device for DNA incubation. All measurements were performed at temperatures between 21 and 24°C (ambient room temperature). Briefly, we replaced the fluidics line containing PBS with a new line containing assay buffer and again washed the inlet manifold of the device for 10 minutes. To equilibrate expressed TFs with assay buffer, we flowed assay buffer across the device for 5 minutes with the ''button'' valves closed, then opened the ''button'' valves and flowed for an additional 2 minutes; this process was repeated twice. We followed this with another 50-minute buffer equil-

ibration period, in which "button" valves were open, exposing TFs to assay buffer. During this preliminary equilibration step, we connected Tygon tubing containing each labeled dsDNA concentration to be assayed into the device, allowing all subsequent experimental steps to be automated using custom in-house software (https://github.com/FordyceLab/RunPack-STAMMP).

For each concentration of DNA (from the lowest to the highest), we: (1) closed "neck" and "button" valves and opened "sandwich" and inlet and outlet valves; (2) flowed labeled DNA across the device for 10 minutes; (3) closed "sandwich", inlet, and outlet valves; (4) opened "button" valves (to allow surface-immobilized TFs to interact with soluble DNA); (5) incubated for 50 minutes (to allow reactions to come to equilibrium); (6) imaged all chambers within the device in the Cy5 (DNA) channel (to quantify intensities and calculate the concentration of soluble DNA available for binding in each chamber); (7) closed "button" valves (to trap TF-bound DNA); (8) washed with assay buffer for 10 minutes; and (9) imaged all chambers in both the GFP (TF) and Cy5 (DNA) channels to quantify the relative intensities of trapped species in each chamber. To quantify free DNA in solution at each step, we imaged the device in the Cy5 channel at exposures ranging from 30 ms to 150 ms to ensure an adequate dynamic range for downstream analysis. To quantify surface-immobilized TF intensities and intensities of bound DNA, we acquired 500 ms exposure images in the GFP channel and 3000 ms exposure images in the Cy5 channel. To image the entire device, we tiled acquisitions across the device (typically 7 x 7 gridded images).

QUANTIFICATION AND STATISTICAL ANALYSIS

We performed all analysis in Python, with exceptions as noted below.

Image Processing and Quantitation

To correct for position-dependent variation in excitation illumination and collection efficiency, we applied a flatfield correction to all GFP and Cy5 fluorescence images using correction images as previously described (Thorn, 2014). We also collected initial images of devices prior to the start of each experiment for every channel and exposure time to collect background measurements to calculate optimal flatfield correction parameters. Tiled acquisition images were then stitched to generate a single large image of each device using an in-house image stitching program (https://github.com/FordyceLab/ImageStitcher).

Each DNA concentration measurement yielded 3 stitched images: (1) a "Prewash Cy5" image in the Cy5 channel used to calculate the concentration of free DNA available for binding; (2) a "Postwash GFP" images used to quantify the amount of surface-immobilized TFs at each step of the binding assay; and (3) a "Postwash Cy5" image used to quantify the amount of fluorescently-labeled DNA bound to surface-immobilized TFs at each step.

To quantify Alexa-647-labeled DNA intensities within each chamber (for the "Prewash Cy5" image) and labeled DNA and TF intensities beneath the "button" valve (for the "Postwash GFP" and "Postwash Cy5" images), we used a custom, in-house python image processing package (https://github.com/FordyceLab/ProcessingPack-STAMMP). Briefly, we first identified the four corners of the device by marking the centers of the top left, top right, bottom left, and bottom right corner binding reaction chambers using the "Prewash Cy5" image associated with a high introduced DNA concentration. The other chamber coordinates were initially approximated by using these corners as vertices of a 28-column x 56-row grid (chamber dimensions of the PC1k device); we then employed a Hough Transform to find chamber centers. We then used these same coordinates to quantify median fluorescence chamber intensities for all chambers across all 6 measured DNA concentrations. Finally, median chamber intensities were converted to DNA chamber concentrations using per-chamber DNA calibration curves (as described below).

To quantify fluorescence intensities associated with surface-immobilized TFs and trapped bound DNA, we first identified "button" centroid locations and perimeters using the first "Postwash GFP" image as a reference. "Button" centroid positions were approximated using a grid search to maximize the fluorescence intensity within a circular area slightly larger than the expected physical size of the buttons. We then applied these same feature locations to all "Postwash GFP" and "Postwash Cy5" images, indexed by the DNA concentration step at which they were acquired. To quantify "button"-associated GFP and Alexa-647 intensities within each chamber, we summed the total fluorescence spot intensity in each channel and then subtracted contributions from local background (calculated by summing the intensities of an annulus surrounding the spot area and then normalizing this value by the relative ratio of the "button" and annulus areas). Finally, we associated all chamber and "button" intensities with a particular mutant using a custom Python script that maps plate well location (and associated mutant ID) to reaction chambers within the device.

Quality Control and Binding Curve Generation

Prior to generating binding curves, we employed several quality control checks to the raw imaging data: (1) we computed a linear regression between observed intensities for each chamber in the "Prewash Cy5" image and the concentration of introduced DNA, inspected r^2 values associated with each fit (Figure S2); (2) we compared the distributions of GFP intensities between plasmid-containing chambers and empty chambers and eliminated chambers with intensities below an experiment-specific threshold ($1.5x10^6$ - $2.5x10^6$ RFU); (3) we eliminated any chambers with measured "Postwash Cy5" median intensities below background levels; and (4) we manually examined raw images to eliminate chambers containing any unusual particulates or debris leading to aberrant DNA binding curves.

To generate per-chamber binding curves, we then plotted the measured ratio of intensities beneath the "button" valve (Alexa-647-DNA/TF-GFP from "Postwash Cy5" and "Postwash GFP" images) against the DNA concentration at each assay step.

Calculating K_d values

To determine the measured K_d values for each chamber, we globally fit the measured ratio of fluorescence intensities (DNA intensity/transcription factor intensity) for each chamber to a single-site binding model (Maerkl and Quake, 2007; Fordyce et al., 2010):

$$R_i([DNA_i]) = \frac{R_{max} \cdot [DNA_i]}{K_{d,i} + [DNA_i]}$$

Here, $R_i([DNA_i])$ denotes the measured intensity ratio as a function of soluble DNA concentration within a given chamber, R_{max} is a global constant shared across *all* chambers corresponding to the maximum ratio of intensities at saturating [DNA], $[DNA_i]$ denotes the concentration of soluble DNA within a given chamber, and $K_{d,i}$ denotes the dissociation constant (K_d) for a given chamber. This global fitting procedure relies on the following 4 assumptions:

(1) The fluorescence intensities of the DNA (labeled with AlexaFluor-647) and TFs (labeled with eGFP) are linearly related to the number of molecules bound to the device surface or in solution. With this assumption, the measured ratio of DNA/TF intensities within a given chamber (i.e. the ratio of AlexaFluor-647/GFP intensities) is linearly related to the fractional occupancy (number of DNA molecules bound by surface-immobilized TFs). The validity of this assumption is supported by the fact that observed DNA calibration curves are highly linear **(**Figure S2**).**

(2) The maximum concentration of TF deposited in each chamber is well below measured K_d values, ensuring that there is no significant depletion of DNA ligand even at the lowest DNA concentrations used in the assay and that we can approximate the unbound fraction using the observed chamber intensity prior to binding. We have previously measured the maximum concentration of TF deposited within each chamber to be 30nM (Le et al., 2018), well below the K_d values for the most tightly bound sequences in the assay. Moreover, we find that measured K_d values between experiments are unchanged by 2-fold differences in the amount of immobilized TF-eGFP, as expected for immobilized TF concentrations well below measured K_ds **(**Figure S16**).**

(3) The reaction has come to equilibrium prior to making the measurement. In our assays, we incubated TFs with each concentration of DNA for 50 minutes, consistent with prior work (Maerkl and Quake, 2007; Fordyce et al., 2010; Le et al., 2018). As described in Jarmoskaite et al. 2020, the rate equation for the approach to equilibrium for a two-component binding system under conditions where one binding partner (here, the DNA) is in excess is given by:

$$k_{equil} = k_{on}[\mathrm{DNA}] + k_{off}$$

Here, k_{equil} represents the rate constant for the approach to equilibrium, k_{on} is the association rate constant, [DNA] is the soluble DNA concentration, and k_{off} is the dissociation rate constant (Jarmoskaite et al., 2020). This rate constant is the slowest under the limiting conditions in which the [DNA] concentration approaches zero, yielding:

$$k_{equil} \sim k_{off}$$

To estimate the half-life of the time to reach equilibrium for Pho4 binding interactions, we can substitute measured values from previous experiments measuring TF dissociation rates for wildtype Tye7 (another bHLH TF from yeast) of $\sim 8 \times 10^{-3}$ s^{-1} (Geertz et al., 2012):

$$t_{1/2} = \frac{\ln(2)}{k_{equil}} \sim \frac{\ln(2)}{k_{off}}$$

This calculation yields an estimated $t_{1/2}$ of 87 seconds for high-affinity consensus motifs; for weaker interactions, we note that k_{off} increases, reducing the time to equilibrium. In the STAMMP experiments, we equilibrated all measurements for 50 minutes, equivalent to over 30 estimated half-lives and well in excess of the 5 half-lives required to reach 96.6% completion.

(4) Mutations to Pho4 do not significantly affect the stoichiometry of the binding interaction. With this assumption, all chambers can be fit with a single chamber-specific affinity parameter ($K_{d,i}$) and a single shared R_{max} value, thereby making it possible to extract K_d values even for oligonucleotides with K_ds well above the highest measured concentration whose curves do not plateau. This assumption is supported by the observation that local fits to all chambers that reach saturation (in which we do not constrain the R_{max} parameter to be the same across chambers) return best fit R_{max} values that vary by only ~33% from the median R_{max} for nearly all mutants **(**Figure S5**)** (with the exception of A289K and A289R, which we excluded from downstream analyses of DNA sequences with only flanking nucleotide mutations as they could not be appropriately fitted using the global fit).

To enhance the accuracy of estimated K_d values even for oligonucleotides with binding affinities above the highest measured DNA concentration, we initially determined a global R_{max} value for all mutants by calculating the median Alexa-647-DNA/TF-GFP ratio for the top 10% of DNA/protein measurements at the final DNA concentration within the assay. We then fit all curves using this constant R_{max} across all chambers within a given experiment, optimizing only the per-chamber K_d value via nonlinear least squares fitting. Over several experiments for experiments containing only flanking nucleotide mutations (where many mutants reached saturation at the maximum [DNA]), this R_{max} value was largely consistent (0.67 ± 0.012, median ± SEM) (Figure S12). For experiments assessing bind-

ing to oligonucleotides containing mutations in the core consensus site, this median R_{max} value was typically lower, and so all curves were fitted using R_{max} values of 0.66 or 0.68. In one experiment, we calibrated the R_{max} value by measuring binding to the reference DNA sequence 5'-C CACGTG A-3' at a high concentration and used the median of the top 10%. All binding curves and all returned K_ds for all chambers across all experiments are available as Supplemental Files.

To calculate ΔΔGs across a given experiment, we used the following formula:

$$\Delta\Delta G = RT \cdot \ln\left(\frac{K_d}{K_{d,ref}}\right) \quad \text{(Equation 2)}$$

where R is the gas constant ($1.987 \cdot 10^{-3}$ kcal/(K · mol)), T is 298 K, and $K_{d,\,ref}$ is the median K_d measurement for the wildtype PHO4 protein interacting with the DNA oligonucleotide sequence used in a given experiment.

In Equation 2, $K_{d,\,ref}$ was calculated by taking the median affinity of all wildtype Pho4 measurements for a particular oligonucleotide sequence. For the above calculation, the median number of wildtype Pho4 replicates was 12 measurements per experiment (range: 2-16 replicates per experiment).

Determining Statistical Significance from Wildtype Pho4 & from Background

To identify mutants with statistically significant differences in DNA binding from the WT protein, we compared the distribution of all measured ΔΔG values for every mutant against the distribution of all measured ΔΔG values for the WT Pho4 protein using an independent, two-tailed T-test (assuming unpooled variance). We used a Bonferroni corrected p-value assuming a normal *p-value* of 0.05 and 213 measured mutants ($p < 0.0003$) as a threshold of significance.

To identify mutants with binding that was statistically significantly different from background (nonspecific) DNA binding on the assay, we compared the distribution of all measured ΔΔG values for every mutant against the distribution of all measured ΔΔG values for an A299D mutant that lacks DNA binding and again used a Bonferroni correction to determine a conservative threshold for significance. To select A299D as an appropriate mutant to use, we compared the Cy5 signal intensities for empty chambers (without expressed TFs) with those of several TF variants at the highest DNA concentration assayed for two sample experiments. Measured fluorescence intensities for two null-binding mutants, H257P and A299D, were consistently similar to those of the empty chambers (Figure S7). As A299 is not involved in DNA binding or close to DNA binding residues, we selected A299D for comparison.

Predicting Likely Effects from Phylogeny

Analysis of Pho4 Variants via PROVEAN

To attempt to predict whether certain Pho4 mutants would be 'damaging' for function, we used the PROVEAN (PROtein Variation Effect Analyzer) software tool (Choi, et. al., 2012, 2015) as provided using default cutoff score of -2.5.

To generate a receiver operating characteristic (ROC) curve, we compared the PROVEAN scores to the ΔΔG values for the reference DNA sequence 5'-CCACGTGA-3'. We considered mutants that were between -0.5 kcal/mol and 1 kcal/mol (inclusive) as indistinguishable from wildtype (ie. a benign variant). For ROC analysis, we varied the prediction cutoff score -10 to 3 in increments of 0.5 and calculated four quantities at each cutoff:

(1) true-neutral (TN): statistically indistinguishable binding from wildtype and predicted benign;
(2) false-neutral (FN): statistically significantly different binding from wildtype Pho4 and predicted neutral;
(3) true-deleterious (TD): distinguishable from wildtype Pho4 and predicted deleterious; and
(4) false-deleterious (FD): indistinguishable from wildtype and predicted deleterious.

At each threshold, we calculated true positive rate (TP) and false positive rate (FP) using the following formulae: TP = TN/(TP+FD) and FP = FN/(FN+TD). We then calculated the area under the curve (AUC) for the ROC using the trapz function in Python (NumPy). As a negative control, we also calculated ROC and AUC values for 25 trials in which ΔΔG values were scrambled.

Entropy Calculations

We calculated entropy at every Pho4 position using a publicly available deposited sequence alignment for bHLH proteins (bHLH Family identifier: PF00010) We then trimmed columns in the multiple sequence alignment to include non-gapped positions in the Pho4 reference sequence. Entropy was calculated using the information_content method within the Biopython package with the expected frequency of each residue at every position within Pho4 at the default setting for the Biopython information_content method (Cock et al., 2009).

Identifying 'Affinity' and 'Specificity' Mutants

Affinity vs. *Specificity Analysis*

To test if mutations globally enhanced affinity or altered specificity, we considered all data from oligonucleotides containing 'flanking' nucleotide mutations (5'-CCACGTGA-3', 5'-GCACGTGC-3', 5'-ACACGTGA-3', and 5'-TCACGTGC-3') *and* 'core' nucleotide mutations (5'-CCACGTGA-3', 5'-CAACGTGA-3', 5'-CCGCGTGA-3', 5'-CCATGTGA-3', 5'-CCACGCGA-3', and 5'-CCACGTTA-3'). Because their affinities were increased beyond assay resolution, we excluded A289K and A289R from analysis for all 'flanking' nucleotide mutations. For the DNA sequence 5'-TCACGTGC-3', we also noted that H255R raised affinity beyond assay resolution and, for this DNA sequence, also excluded this mutant. For each mutant and for each oligonucleotide sequence, we then calculated the

normalized change in affinity for that mutant relative to all Pho4 constructs ($K_{d,mutant}/K_{d,median\ for\ all\ mutants}$). For each mutant, we then calculated the median and standard deviation values of this metric to identify constructs that consistently increased or decreased affinity to all oligonucleotides ('affinity mutants') or had a particularly large variance in values ('specificity mutants').

If we calculate a normalized affinity where we divide the measured K_d for a particular TF/oligonucleotide pair by the median measured K_d for *all* Pho4 variants interacting with that oligonucleotide, then we would recover a 'normalized affinity' of 1 for a TF mutation that did not affect binding to that oligonucleotide, >1 for a TF mutation that *decreased* binding (increased the K_d), and <1 for a TF mutation that *increased* binding (decreased the K_d). For a mutation with equally reduced binding across all oligonucleotides, we would therefore expect to see a reduced *median* normalized affinity without any increased variance in these values. For a mutation with preferential effects on binding to a limited number of oligonucleotides (ie. changes in specificity), however, we would expect to see an increased variance as changes in binding affinity are now unequal across all DNA sequences studied.

Affinity-Enhancing Mutants

We then identified 'affinity-enhancing' mutants using a T-test against WT Pho4 using a Bonferroni-corrected *p-value* as the significance threshold and considering pools of 'flanking' and 'core' mutant oligonucleotides separately (Figure S19). To arrive at a final list, we further required that mutants enhance affinity by at least 0.3 kcal/mol (*i.e.* >2 standard deviations for WT Pho4 ΔΔG measurements for oligonucleotides containing 'flanking' mutations (median ΔΔG ~ 0 kcal/mol; standard deviation: 0.13 kcal/mol)) for *either* 'flanking' or 'core' mutations. This allowed, for example, consideration of mutants for which binding affinity was increased beyond reliable measurement for flanking nucleotide mutations (eg. A289R, A289K) but was measurable for core site mutations. We then categorized residues based on whether they were within or outside the DNA binding domain, resulted in altered charge of the TF, was at a solvent-facing residue, or was another type of mutation.

Identifying Mutants with 'Altered' Yet Detectable DNA Binding

To identify mutations that altered DNA binding relative to WT, we again aggregated affinity measurements for all oligonucleotides and grouped measurements by protein mutant. For each mutant and for each oligonucleotide sequence, we then calculated the change in binding affinity relative to the affinity of the WT Pho4 construct for that oligonucleotide sequence:

$$\Delta\Delta G_{mutant,\ oligonucleotide} = RT \cdot \ln\left(\frac{K_d}{K_{d,ref}}\right)$$

We then performed a T-test comparing the distribution of ΔΔG values for each mutant relative to the distribution of ΔΔG values for the WT Pho4 construct. Using a Bonferroni-corrected *p-value* threshold ($p < 0.05/215$ mutants), we identified 163/215 mutants with statistically significantly different binding from the WT Pho4 for at least 1 oligonucleotide. Next, we tested whether binding was statistically significantly different from background binding by comparing the distribution of ΔΔG values for each mutant with that of the DNA binding-deficient A299D mutant. Using the same *p-value* threshold, we identified 184/215 mutants that retained detectable binding across at least one oligonucleotide. Finally, we considered the union of these 2 sets (133 mutants) to generate a list of mutants that statistically significantly altered but did not ablate DNA binding.

Identifying Combinations of Residue and Nucleotide Mutations that Preserved Physiological Binding

To identify particular residue/nucleotide mutations that altered but preserved physiologically-relevant levels of binding, we: (1) considered the aggregate dataset of 1849 K_d measurements for all mutants and oligonucleotides, (2) identified mutants with binding that was statistically significantly different from WT but still detectable (as above), (3) filtered out any measurements with K_d values *higher* than the median Kd measured for WT Pho4 interacting with the known physiologically relevant low affinity 5'-C CACGT**T** A-3' site (*e.g.* mutant/nucleotide combinations with weaker binding) (K_d = 12 ± 0.2 μM), and (4) filtered out TF mutations at known DNA nucleotide-contacting residues (*i.e.* Pho4 positions 252, 255, 259, and 263). Finally, we quantified the fraction of combinations of these TF and DNA mutations that altered yet preserved binding that involved a 'flanking' nucleotide mutation. Through this analysis, we found: (1) 1063/1849 combinations of TF and DNA mutations yielded altered binding affinities that were tighter than that measured for WT Pho4 interacting with the 5'-C CACGT**T** A-3' sequence, (2) that 648/1849 of these combinations were also statistically significantly different from WT, and (3) that 435/648 of these combinations involved 'flanking' nucleotide substitutions (67%).

Helical Propensity Analysis

Predicted energetic changes resulting from mutation-dependent alterations in helical propensity were taken from prior measurements (O'Neil, KT, DeGrado, WF. *Science*, 1990., Table 1 of publication). To determine the degree to which changes in measured DNA binding affinity could be explained by predicted changes in helical propensity, we plotted measured differences in DBA binding affinity (ΔΔG for Pho4 mutant variants relative to WT Pho4 for the consensus DNA sequence) *vs.* predicted ΔΔG values from changes in helical propensity for the substituted *vs.* the native residue at each position and performed a linear regression. We performed this comparison for solvent-exposed mutations within helix 1 (where we expect changes in helical propensity to dominate observed energetic effects) **(**Figure 6C**)**, at nucleotide-contacting residues (where we expect changes in helical propensity to have an effect but that overall energetic changes are dominated by altered hydrogen bonding) **(**Figure S20A**)**, and within the loop region (where expect changes in helical propensity to have no correlation with changes in measured binding) **(**Figure S20B**)**. For mutations within the loop region, we excluded backbone-contacting residues and two proline residues likely to have additional effects on binding affinity.

Double-Mutant Cycle Analysis

Comparing Differential Effects of TF Mutations

Identifying epistasis across the TF-DNA interface requires 4 affinity measurements: (1) WT Pho4 binding a 'reference' DNA sequence, (2) mutant Pho4 binding a 'reference' DNA sequence, (3) WT Pho4 binding a 'mutant DNA sequence, and (4) mutant Pho4 binding a 'mutant' DNA sequence. Prior to double-mutant cycle analysis, we: (1) eliminated any TF-DNA combinations with < 4 replicate measurements, (2) excluded measurements to TF mutants due to poor fitting quality for the reference DNA sequence (described above in "Affinity vs. specificity analysis"), and (3) $\log_{10}$-transformed all data.

For each mutant cycle, we then: (1) identified TF/DNA mutant combinations with 'detectable' binding (assessed using a T-test comparing measured affinities with those obtained for the binding-deficient A299D mutant interacting with the same oligonucleotide), (2) eliminated TF mutants lacking detectable binding for *both* oligonucleotides (retaining TF mutants with detectable binding for at least one oligonucleotide), (3) plotted measured log-transformed affinities for each mutant (median ± SEM) for the 'mutant' DNA sequence *vs.* the 'reference' DNA sequence (Figure S22), (4) calculated a linear regression of these pairwise comparison values, (4) calculated residuals for each mutant relative to this linear regression, (5) computed the Z-score of the residual (ie. standardized residual) for each mutant relative to all mutants ($Z_i = r_i$ /SD, where r_i is the residual for mutant i, and SD is the standard deviation of the total distribution of residuals), and (6) identified all mutants with $|Z_i| \geq 2$ for further investigation.

To visualize the concentration-dependent binding behavior that would have been expected if the energetic effects of TF and oligonucleotide mutations were purely additive, we first calculated an expected 'additive' K_d value using the median reference K_d value (for WT Pho4 interacting with the 'reference' oligonucleotide), the median K_d resulting from the relevant oligonucleotide mutation alone, and the median K_d resulting from the TF mutation alone as follows:

$$K_d^{TF_{mut},DNA_{mut}} = \frac{K_d^{TF_{mut},DNA_{WT}} \cdot K_d^{TF_{WT},DNA_{mut}}}{K_d^{TF_{WT},DNA_{WT}}}$$

For each measured concentration, we then plotted the binding curve corresponding to this 'additive' K_d using the single-site binding model equation (Equation 1).

To determine whether the candidate TF mutant appeared epistatic with the DNA nucleotide mutation, we used measurements of (1) WT Pho4 and WT DNA, (2) WT Pho4 and mutant DNA, and (3) mutant Pho4 and WT DNA to generate a distribution of additive K_d measurements (n=100 simulated additive measurements). We then performed a Student's T-test comparing the distribution of 'additive' affinities with the experimentally measured affinities for the double-mutant and used a *p-value* cut-off of 0.05 to define TF mutants that are epistatic with DNA mutants.

Cell Systems, Volume *12*

Supplemental Information

High-Throughput Affinity Measurements of Transcription Factor and DNA Mutations Reveal Affinity and Specificity Determinants

Arjun K. Aditham, Craig J. Markin, Daniel A. Mokhtari, Nicole DelRosso, and Polly M. Fordyce

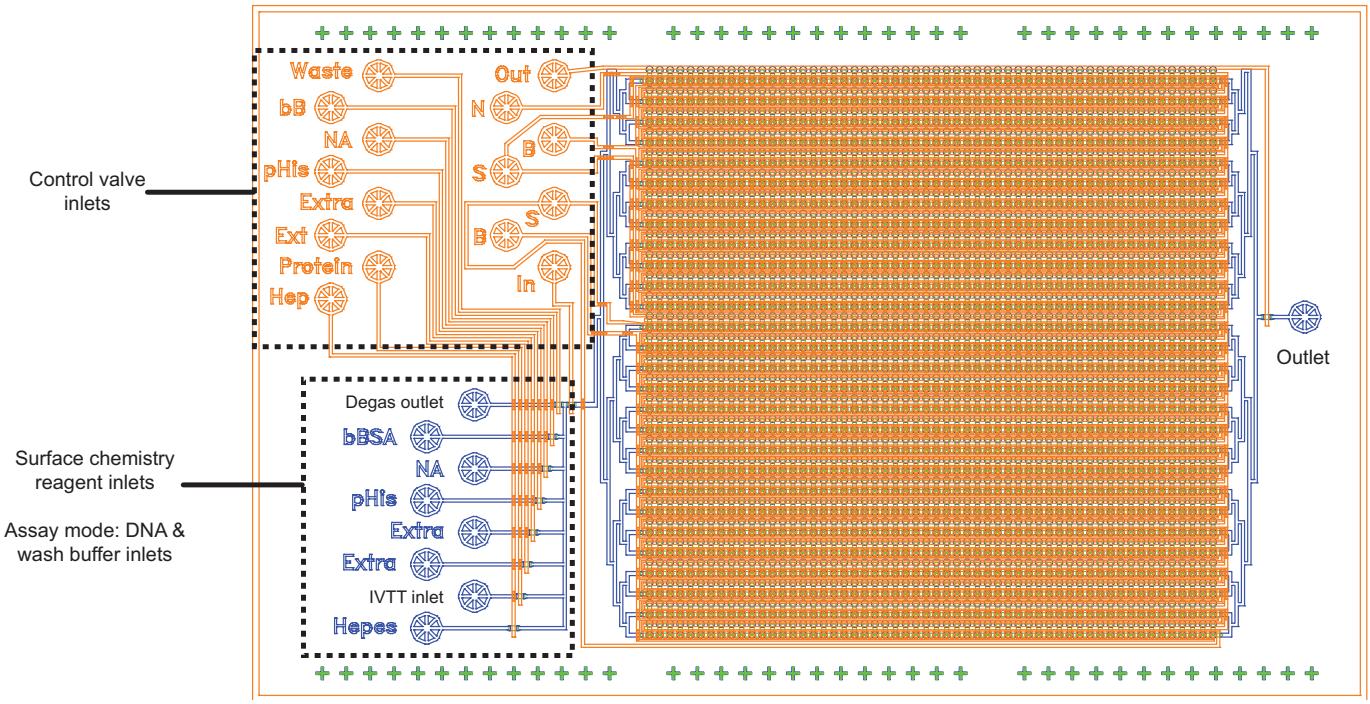

Figure S1 (Related to Figure 1). Architecture of MITOMI microfluidic device. Detailed diagram of MITOMI microfluidic device with valve inlets and outlets annotated showing reagent flow channels (blue) and pneumatic valve channels (orange) that control flow of reagents in device.

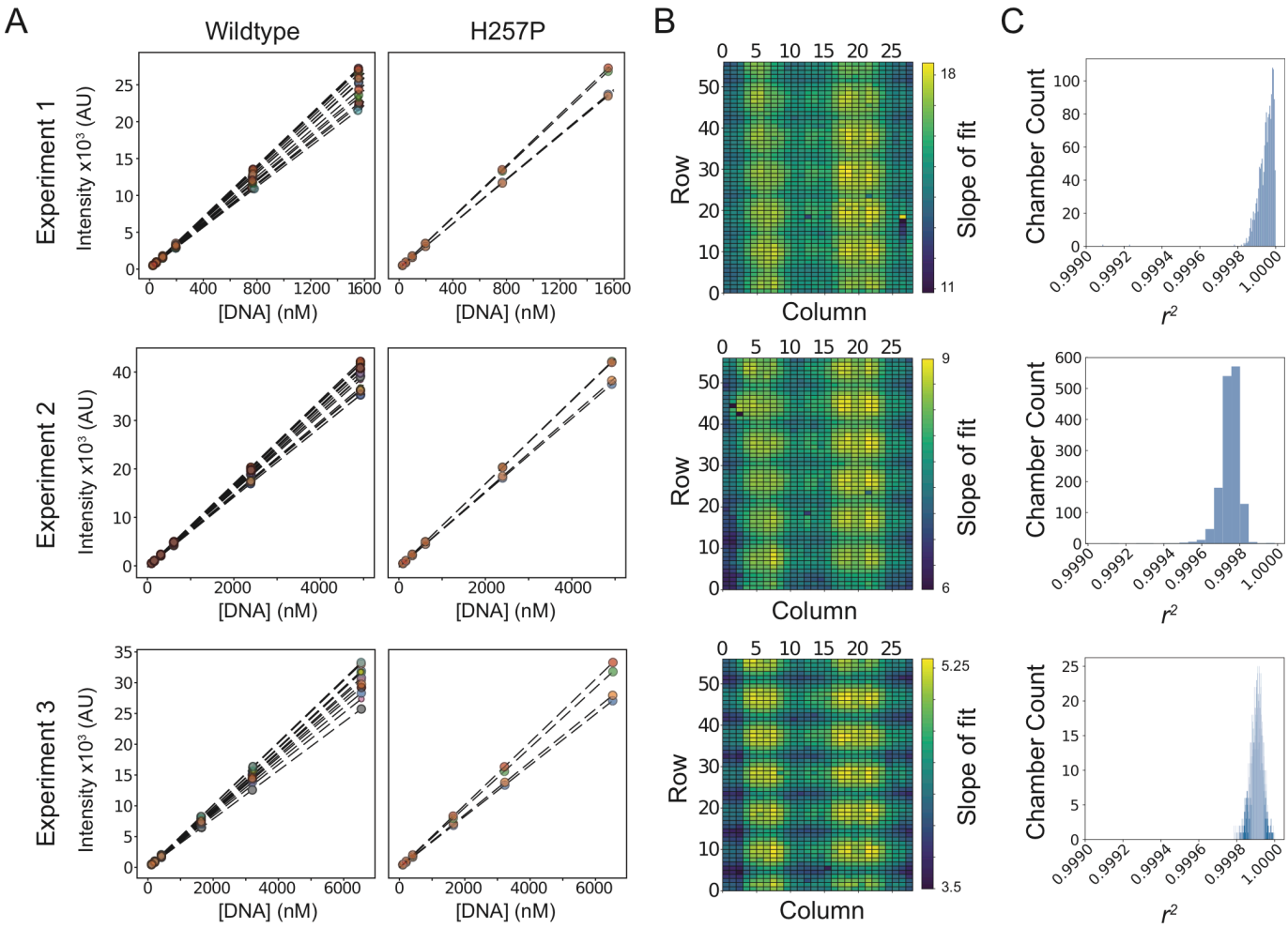

Figure S2 (Related to Figure 1). Calibration curves relating fluorescence intensity and DNA concentration. **(A)** Chamber calibration curves for representative sample chambers containing 2 Pho4 constructs (WT and H257P) across 3 experiments showing individual points (colored by device chamber) and associated linear fits (black dashed lines). **(B)** Heatmaps showing linear fit slope as a function of chamber position within device. Slopes vary by approximately 2-fold across the device, with lowest slopes corresponding to outer edges of the microscope field-of-view. **(C)** Goodness-of-fit distributions for calibration curves.

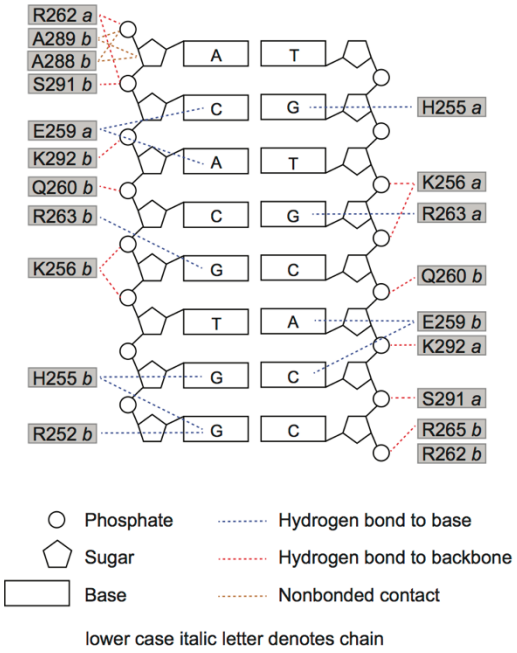

Figure S3 (Related to Figure 3). Amino acid residue and DNA contact map of Pho4 (adapted from Shimizu, et al., 1997 and PDBsum NUCPLOT (Luscombe, et al., 1997)).

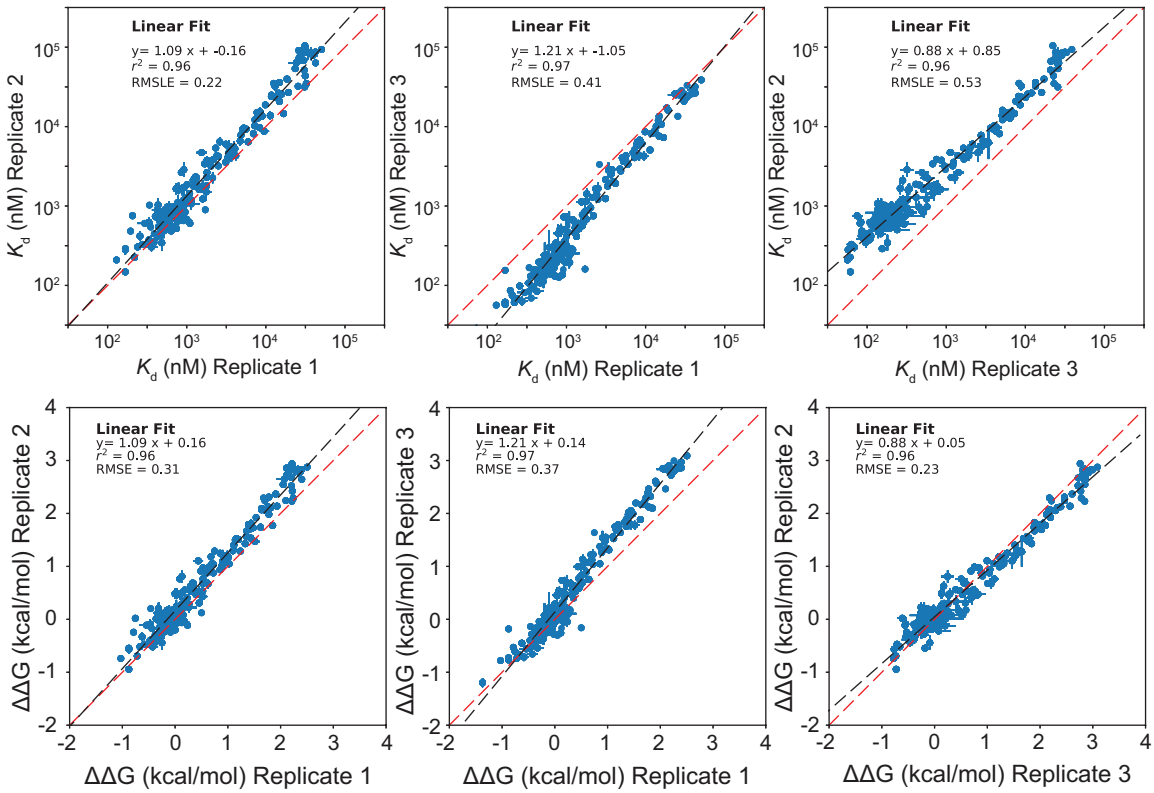

Figure S4 (Related to Figure 4). Pairwise comparison of per-mutant K_ds (top row) and ΔΔGs (bottom row) for all TF mutants across 3 experiments for reference DNA sequence 5'-C CACGTG A-3'. Points indicate median affinities (± SEM) for each TF mutant. ΔΔGs reflect relative differences in binding energy relative to wildtype and vary by <0.4kcal/mol across experiments. Linear fits are indicated by black dashed lines; identity lines are indicated by red dashed lines.

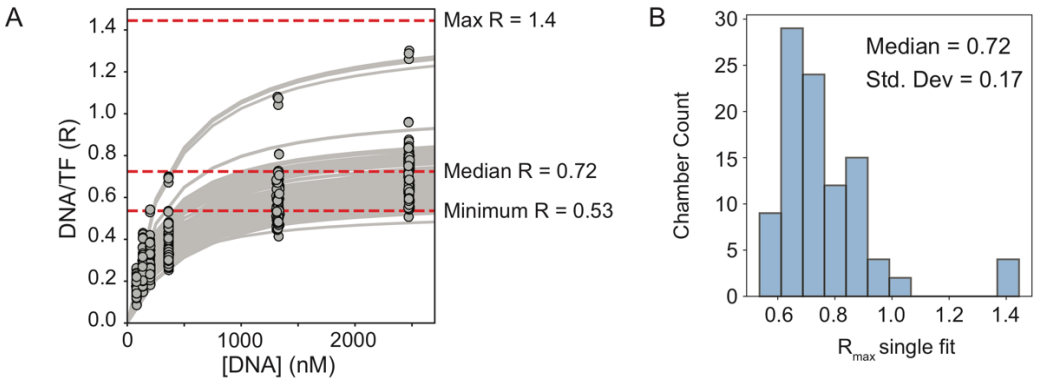

Figure S5 (Related to Figure 4, Methods) Mutations to Pho4 do not perturb binding stoichiometry of Pho4-DNA interactions. **(A)** Per-chamber binding curves for Pho4 mutants with saturating R_{max} allowed to vary for Pho4 mutants that show binding saturation in DNA binding assay. **(B)** Distribution of R_{max} values returned for oll oligonucleotide/TF measurements showing binding saturation.

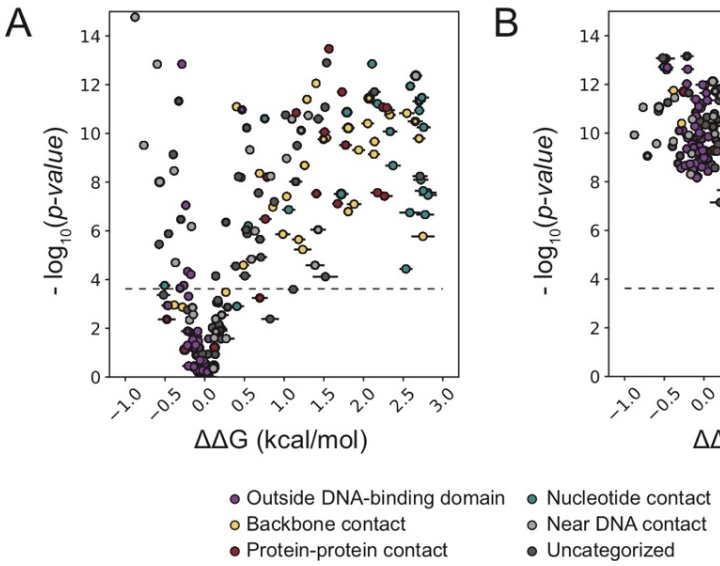

Figure S6 (Related to Figure 4). Determining dynamic range of assay measurements for reference sequence 5'- C CACGTG A -3'. **(A)** Comparison of the distribution of measured ΔΔGs (± SEM) for a given mutant *vs.* the distribution of ΔΔGs for WT Pho4 to determine statistically significant differences in binding (using a two-tailed t-test with a Bonferroni correction). Dashed line indicates estimated threshold for significance (p = 0.00023). **(B)** Comparison of the distribution of measured ΔΔGs (± SEM) for a given mutant *vs.* the distribution of ΔΔGs for an inactive Pho4 mutant (A299D) to determine mutants resolvable from background noise. Dashed line indicates estimated threshold for significance (p = 0.00023).

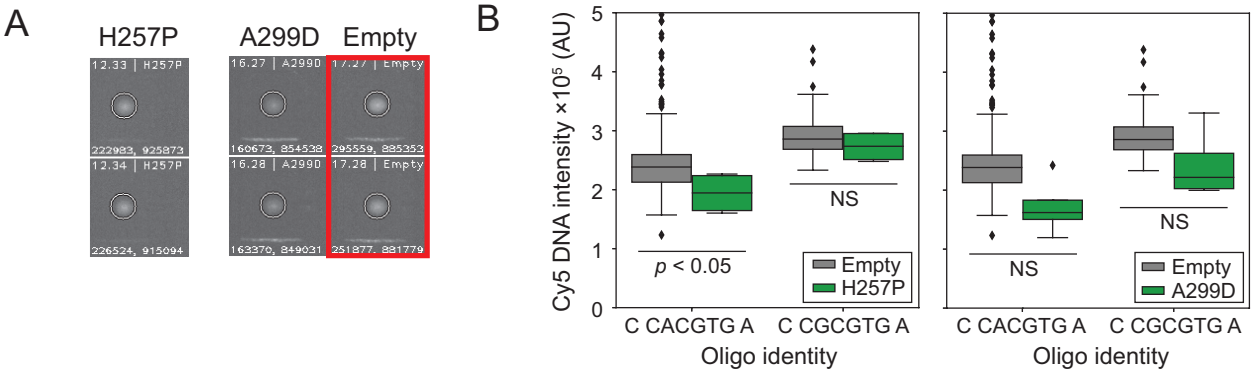

Figure S7 (Related to Figure 4 and Methods). Determining mutants at lower limit of assay detection. **(A)** Images showing measured DNA intensities for two Pho4 variants (H257P and A299D) and empty chambers (boxed in red) to determine effective lower limit of detection for binding to the 5'- C CACGTG A -3' reference sequence. Images are contrast-treated for visibility. **(B)** Distribution of raw Cy5 intensities at the highest DNA concentration for 2 binding deficient mutants (H257P and A299D) across 2 representative devices.

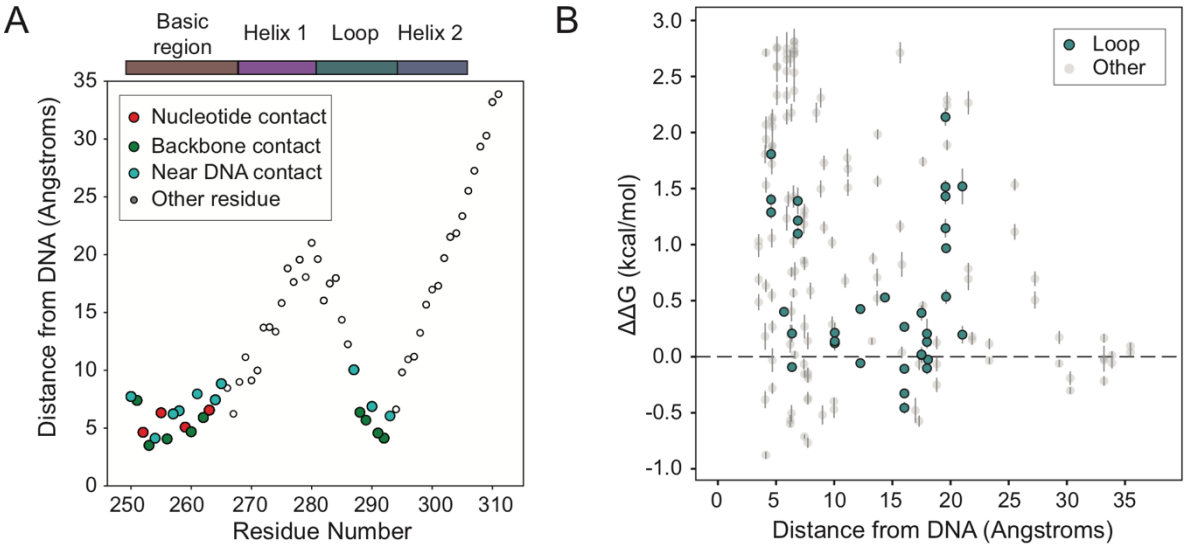

Figure S8 (Related to Figure 4). Measured effect of mutations on DNA affinity as a function of distance from DNA. **(A)** Distance (angstroms) of alpha carbon for each Pho4 residue from DNA, with DNA contacting residues annotated. **(B)** Measured relative change in binding energy (ΔΔG) as a function of distance from DNA for all Pho4 mutants; loop residues are shown in green.

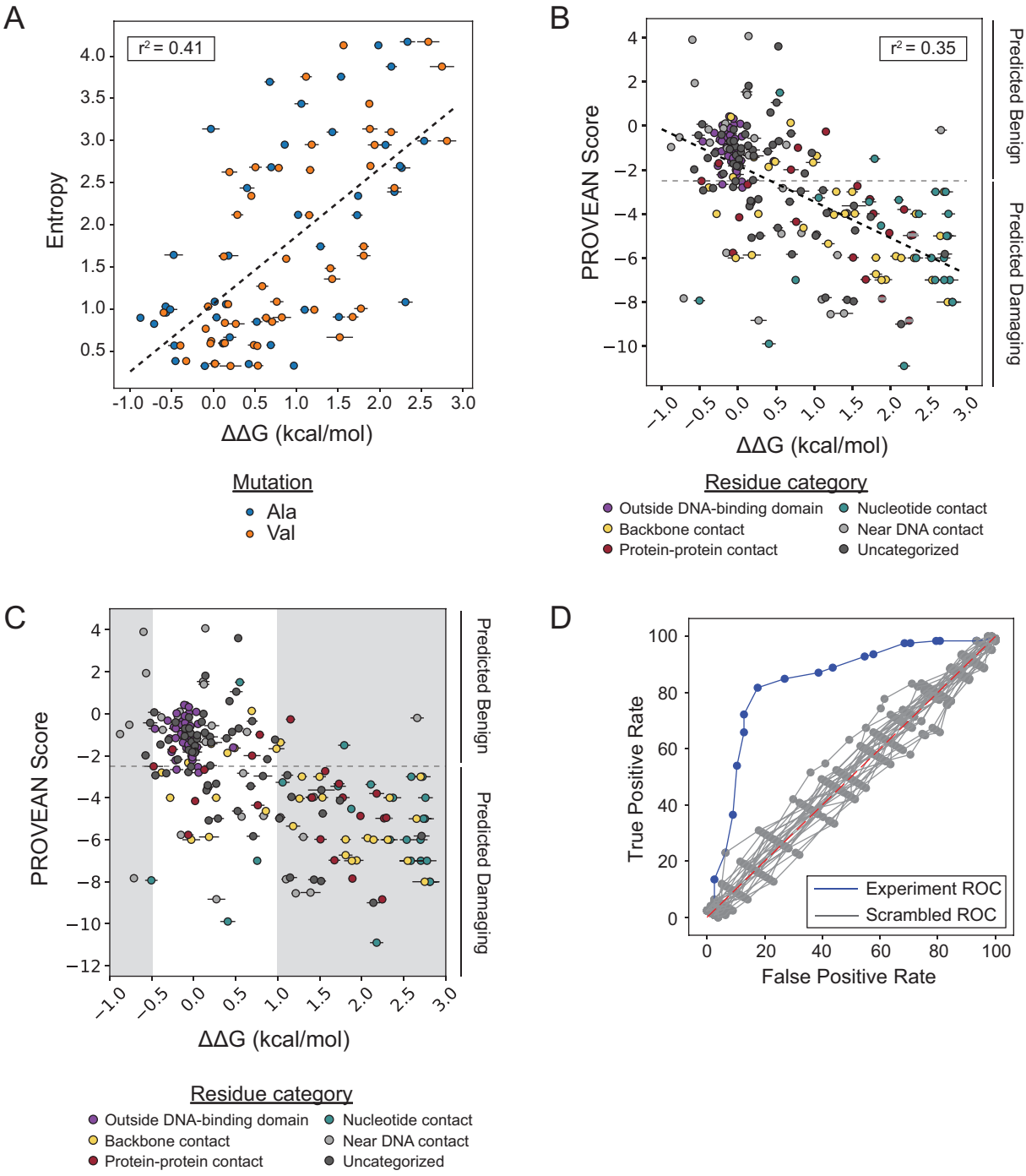

Figure S9 (Related to Figure 4). Comparing observed effects of mutations with those predicted by phylogeny. **(A)** Entropy at a given residue position calculated based on PFAM alignment *vs.* measured mutational effects on affinity (median ΔΔG ± SEM). Dashed line indicates a linear fit between data points (r^2=0.41; y = 0.8*x* + 1.06). **(B)** Calculated PROVEAN score *vs.* measured mutational effect on affinity (median ΔΔG ± SEM). Horizontal dashed line indicates binding affinity of wildtype Pho4; diagonal dashed line indicates a linear regression of the data (r^2=0.35; y = -1.65*x* - 1.8). **(C)** Comparison of PROVEAN score *vs.* measured mutational effect on affinity (median ΔΔG ± SEM) for ROC analysis. Gray regions indicate threshold areas considered 'damaging' (ΔΔG < -0.5 kcal/mol or ΔΔG > 1 kcal/mol). Horizontal dashed line indicates standard damage threshold for PROVEAN. **(D)** ROC curve generated by adjusting damage threshold and calculating false positive and false negative rates. Blue curve indicates experimental ROC (AUC = 0.7). Gray curves indicate 25 separate trials of scrambled ΔΔG (AUC range = 0.43-0.55). Red dash line indicates AUC = 0.5 (random guess).

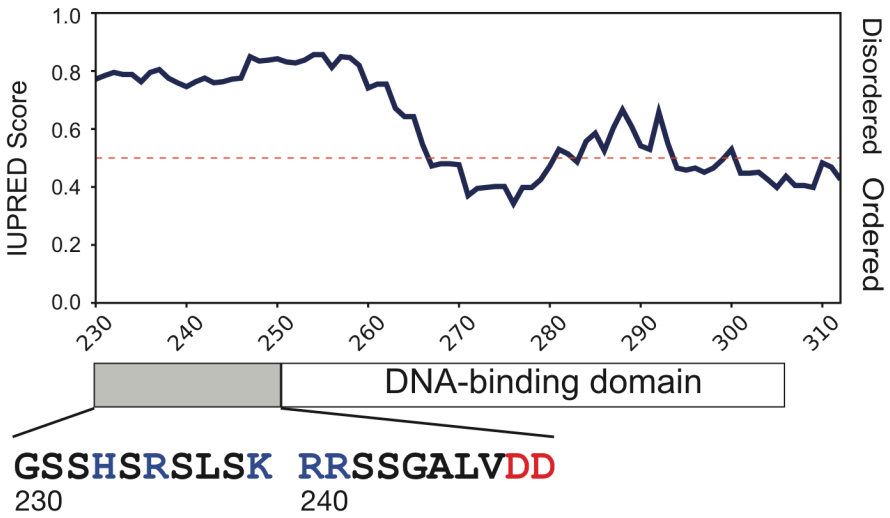

Figure S10 (Related to Figure 4). Predicted disorder of amino acids immediately preceding DNA binding domain of Pho4 (Mészáros, et al., 2018; Erdős and Dosztányi, 2020).

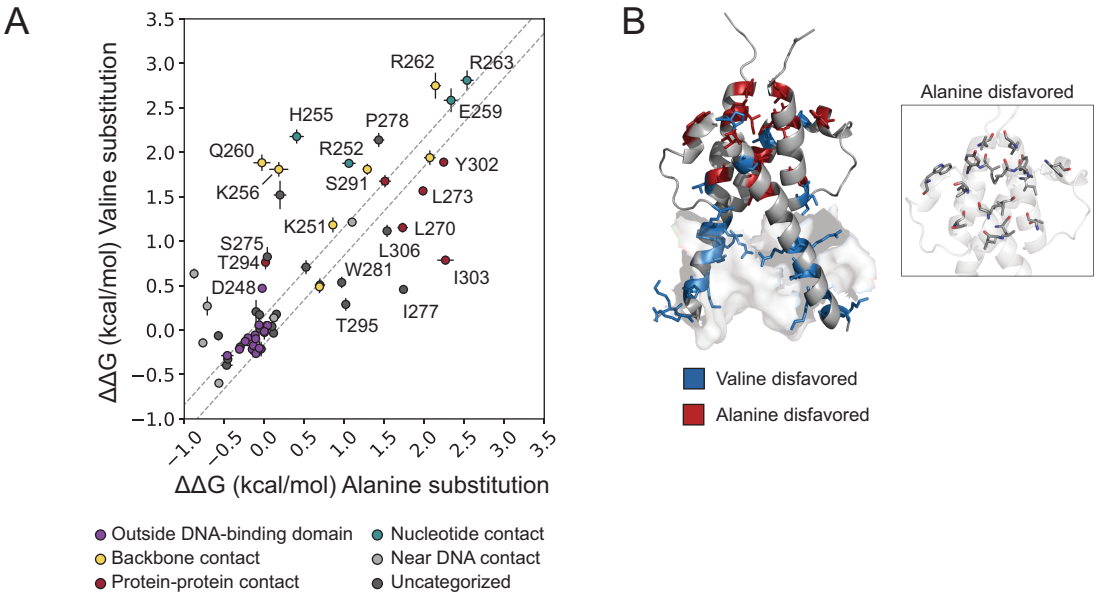

Figure S11 (Related to Figure 4). Differential effects of alanine and valine substitutions. **(A)** Measured ΔΔG values for valine *vs.* alanine substitutions at the same residue position; dashed lines indicate ±1 standard deviation of all wildtype Pho4 ΔΔG measurements. **(B)** Positions at which either alanine or valine are disfavored projected onto Pho4 crystal structure and alanine disfavored residues shown on transparent structure for clarity (inset).

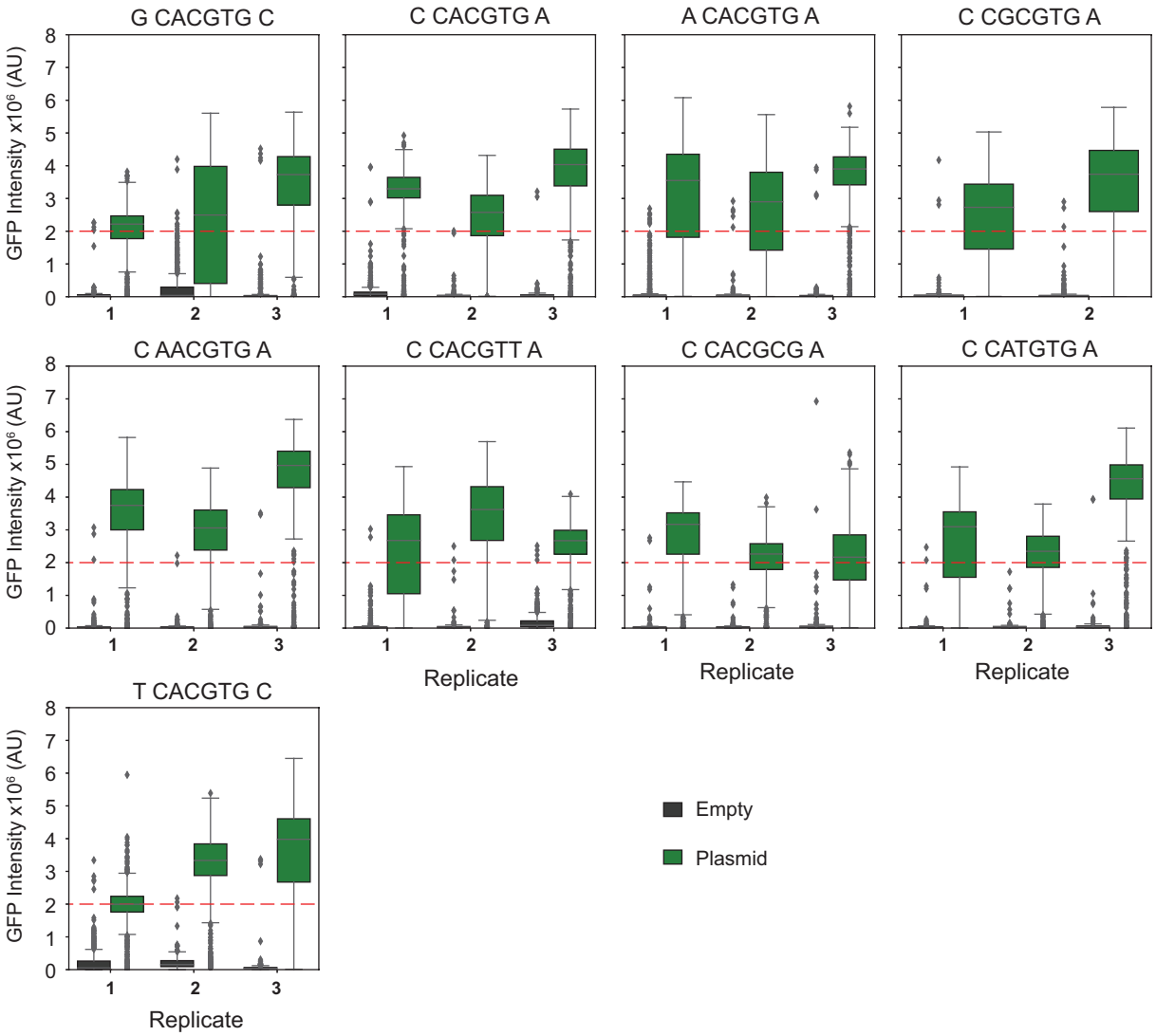

Figure S12 (Related to Figure 5 and supplemental methods). Measured TF GFP intensities for all experimental replicates for mutated DNA sequences in this study.

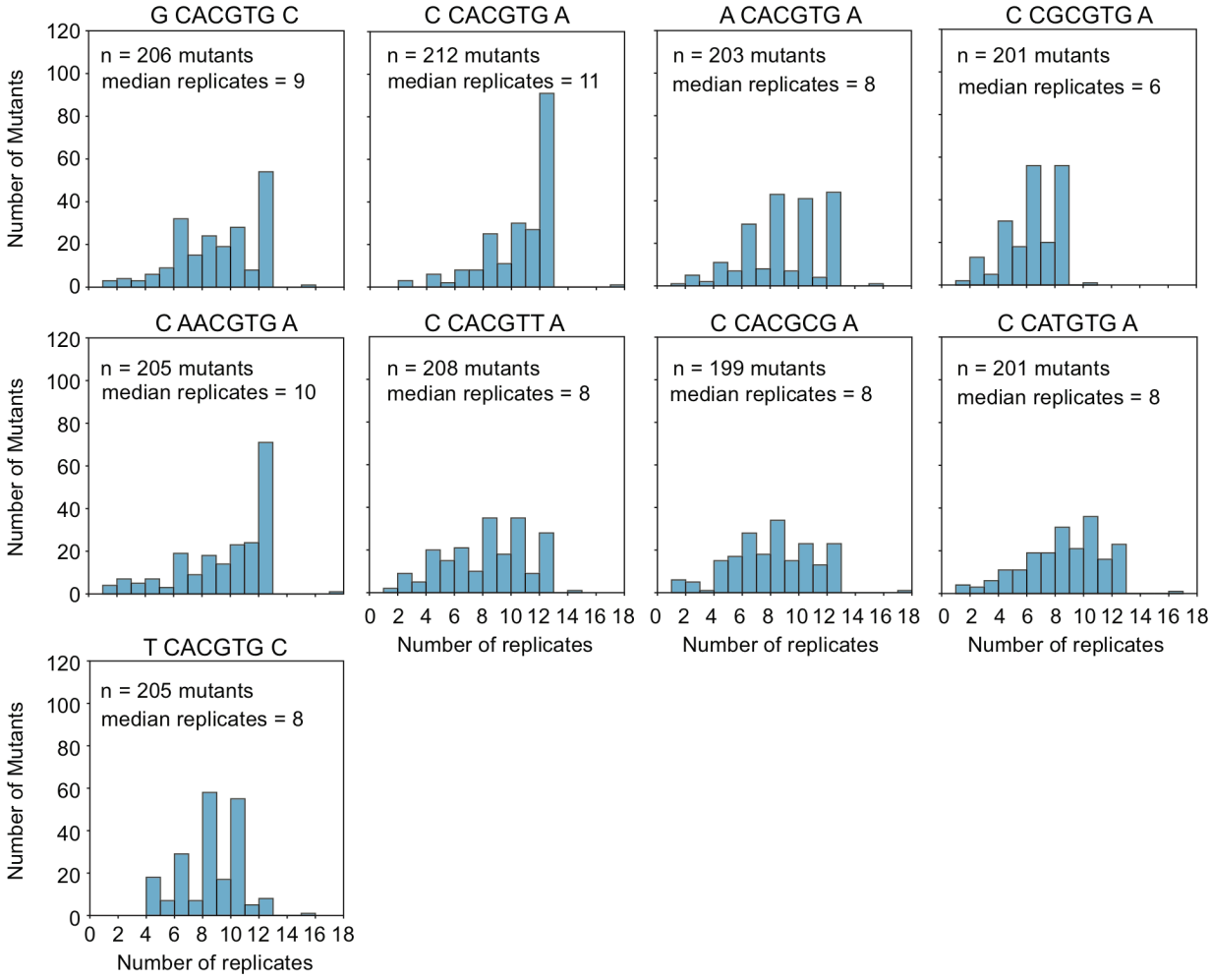

Figure S13 (Related to Figure 5 and supplemental methods). Histograms of experimental replicates per Pho4 mutant for mutated DNA sequences in this study aggregated across 3 devices for oligonucleotides (or 2 devices for the C CGCGTG A oligonucleotide). For visibility, we do not include the number of wildtype Pho4 replicates (2-16 replicates per experiment with a median replicate number of 12).

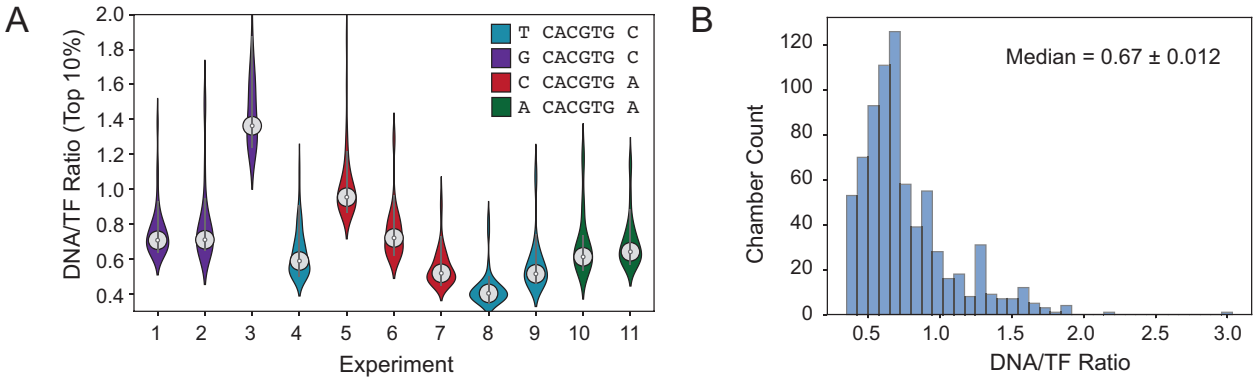

Figure S14 (Related to Figure 5 and supplemental methods). (A) Violin plots for the highest 10% of measured DNA/protein ratios at the highest measured DNA concentration for all experiments containing cognate E-box motif. **(B)** Distribution of number of chambers with a given DNA/TF ratio; median ratio = 0.67 ± 0.012 (SEM).

G CACGTG C

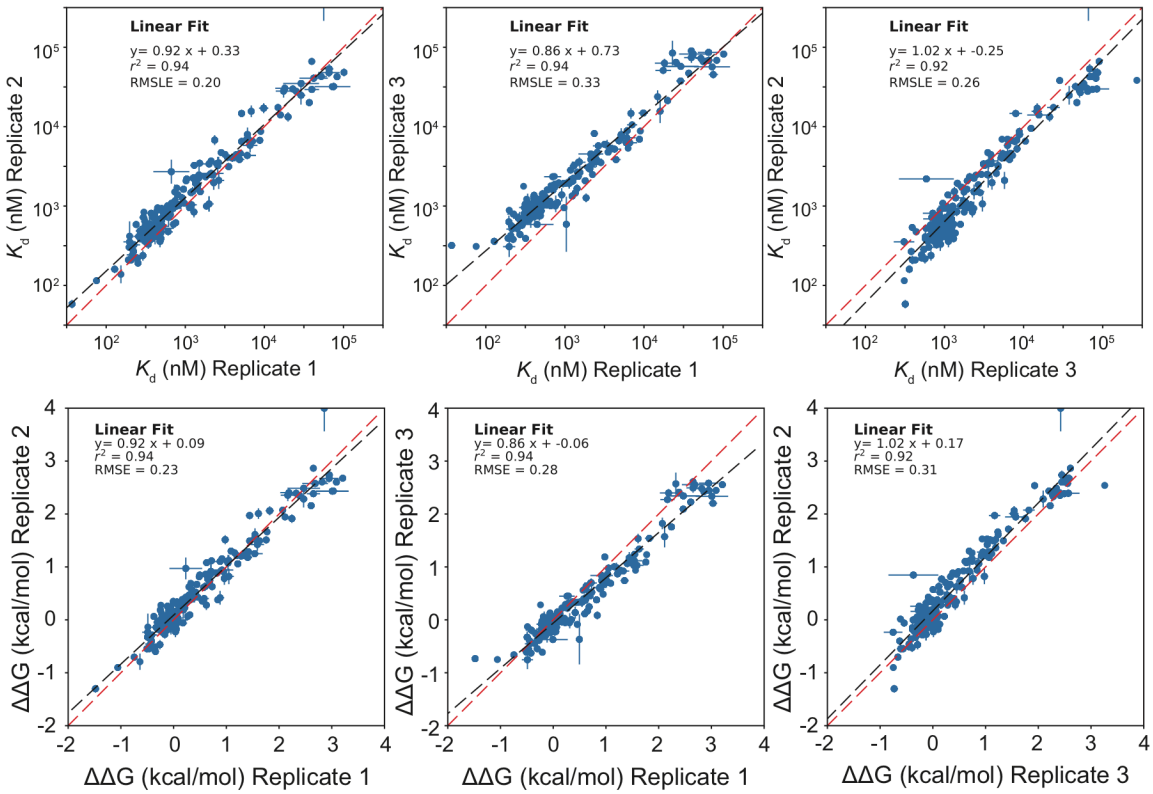

T CACGTG C

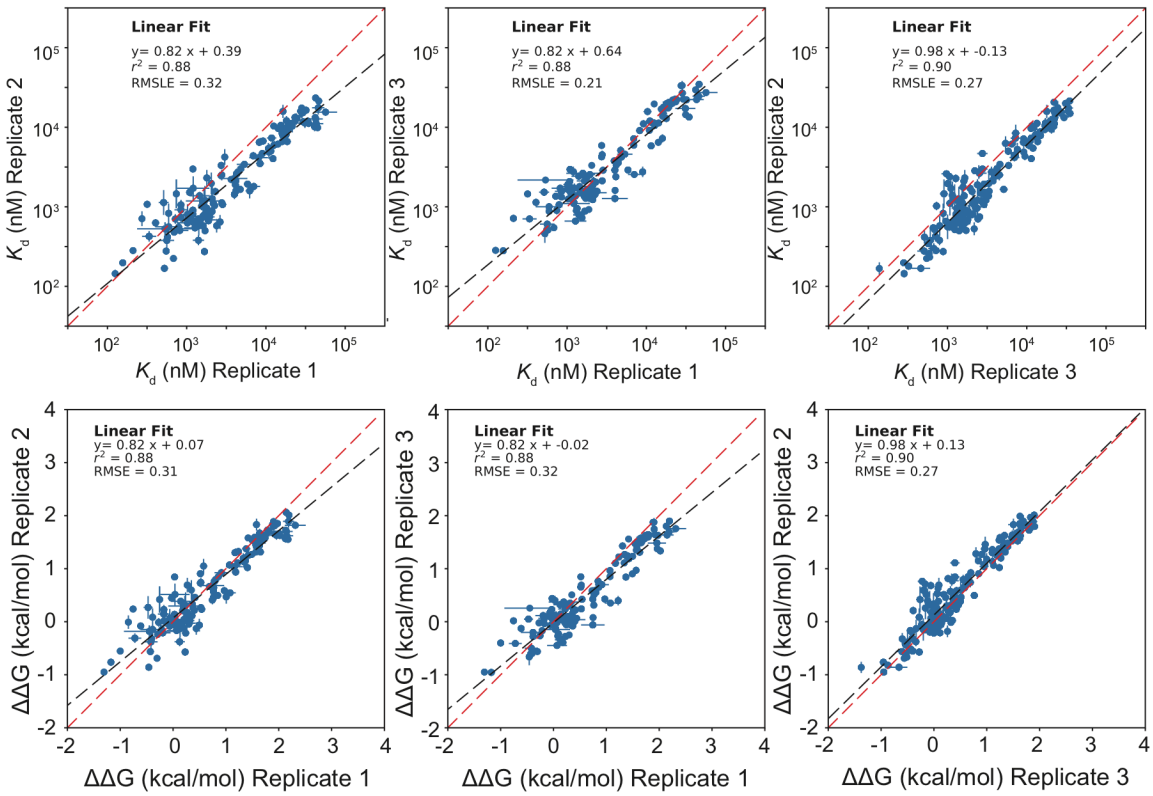

A CACGTG A

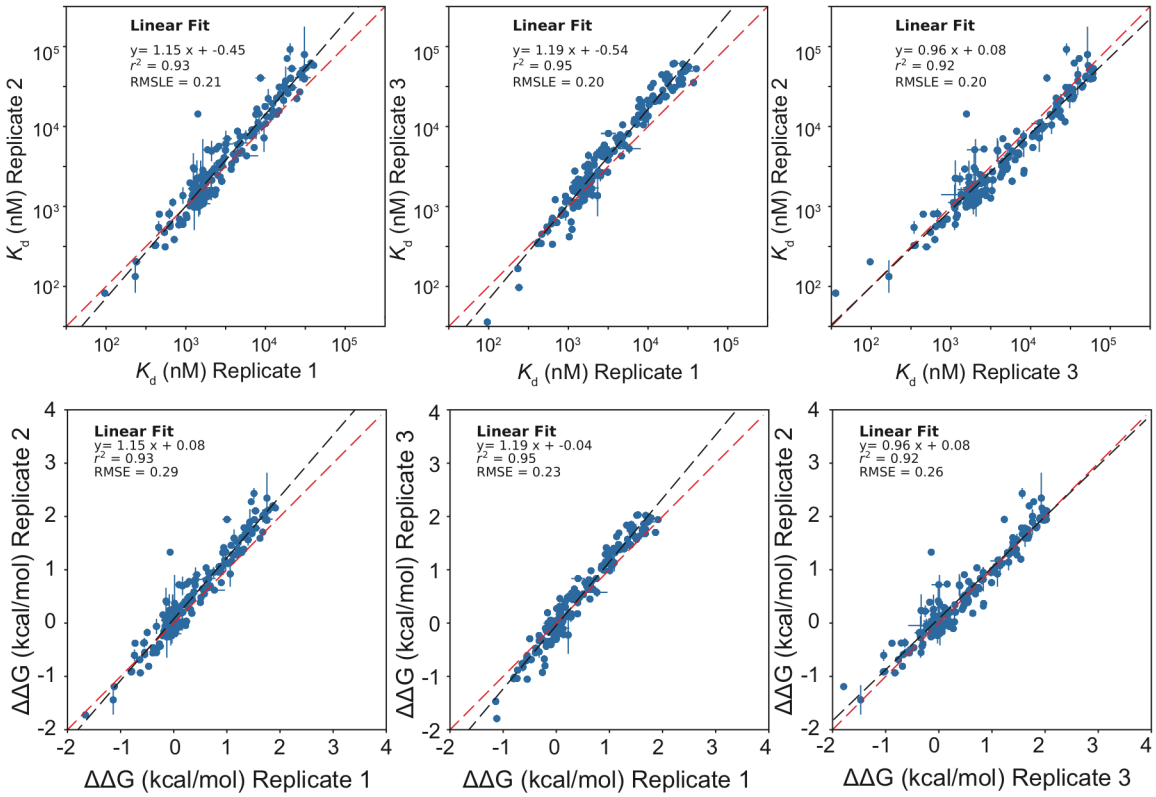

C AACGTG A

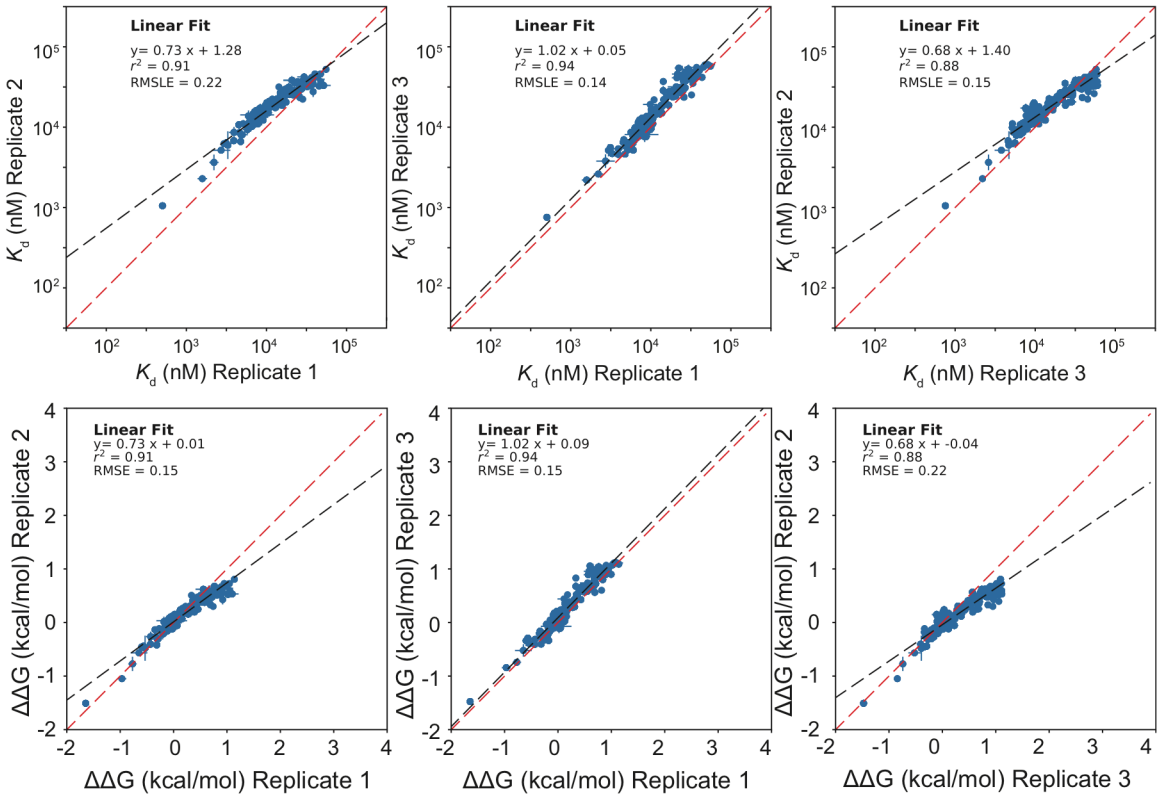

C CACGTT A

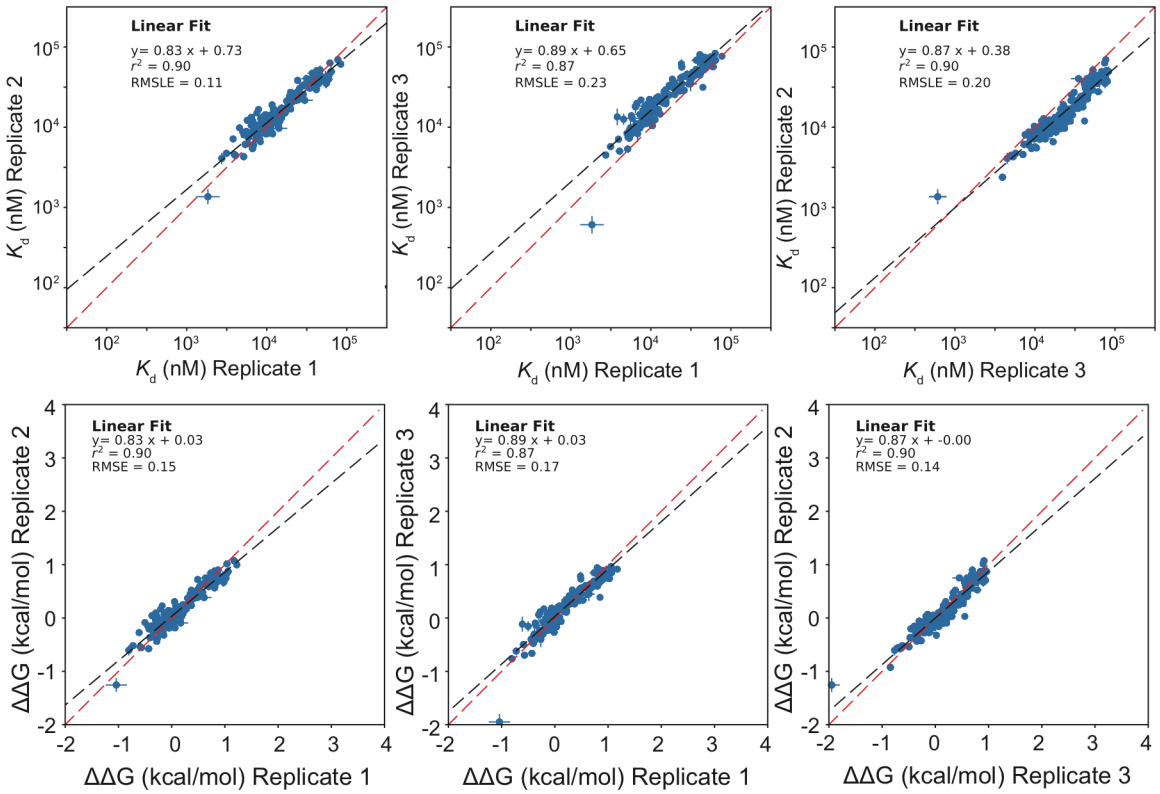

C CACGCG A

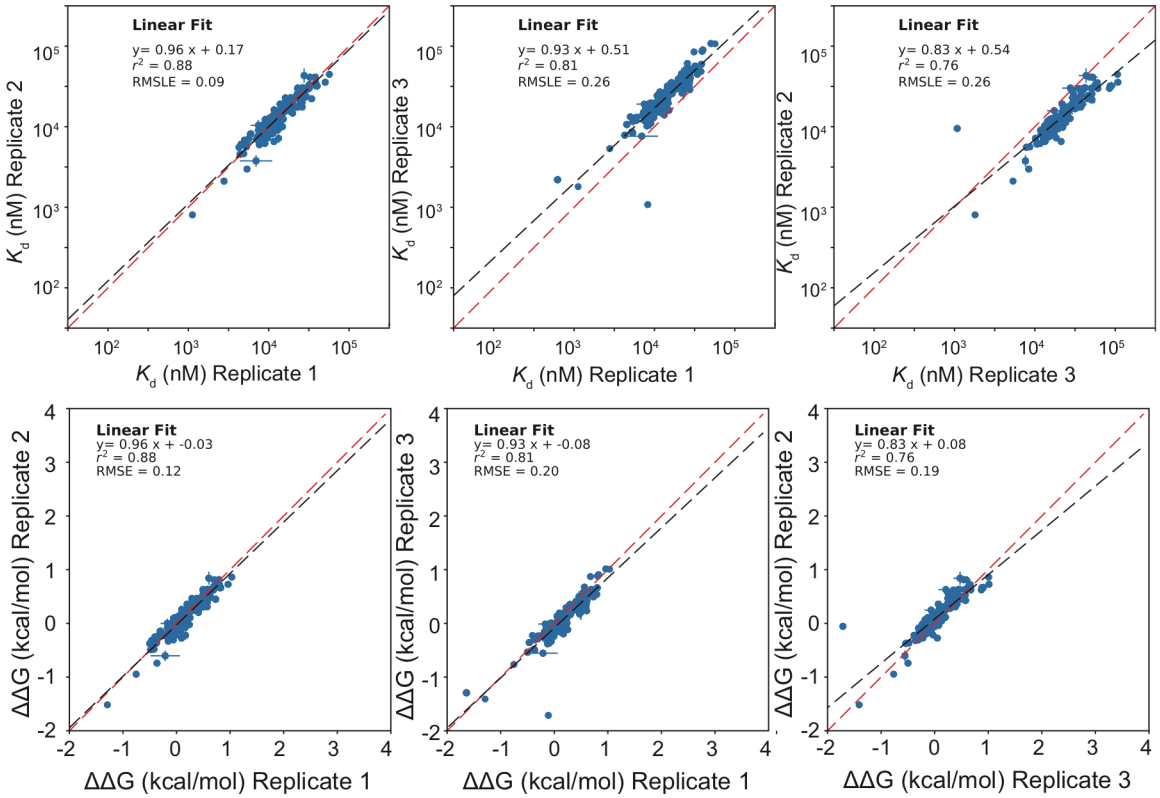

C CATGTG A

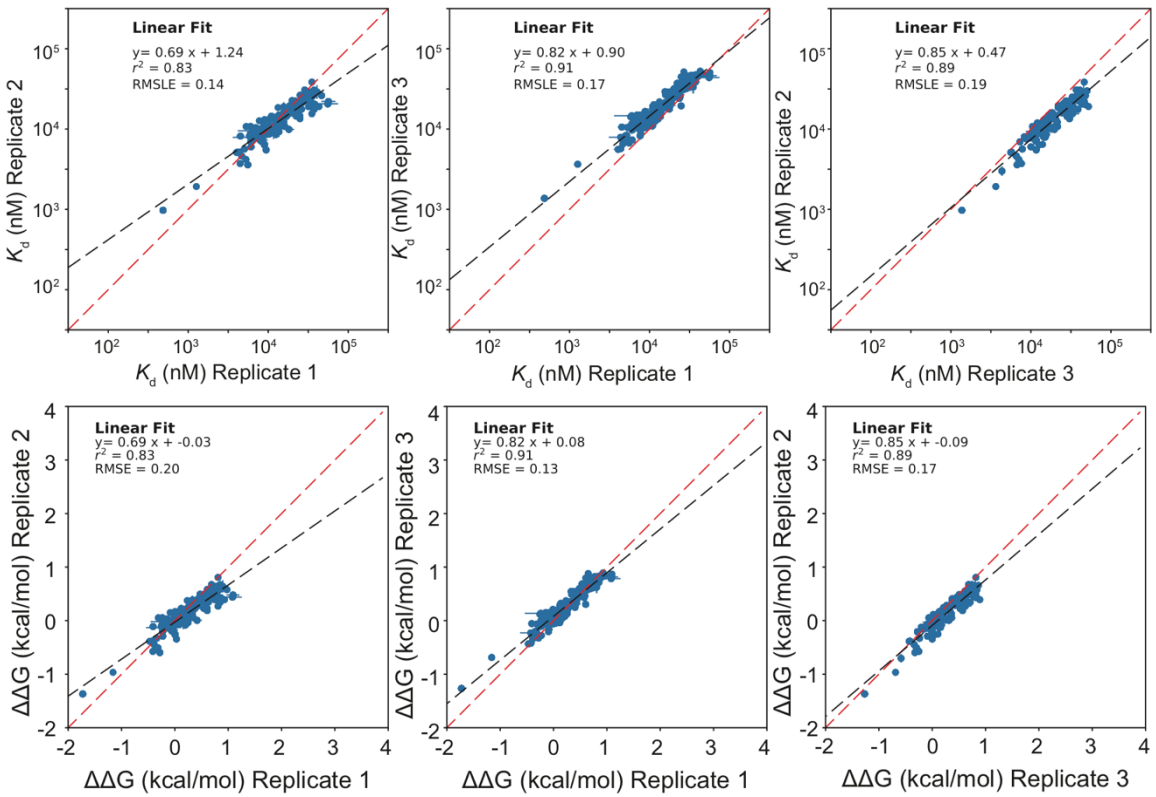

C CGCGTG A

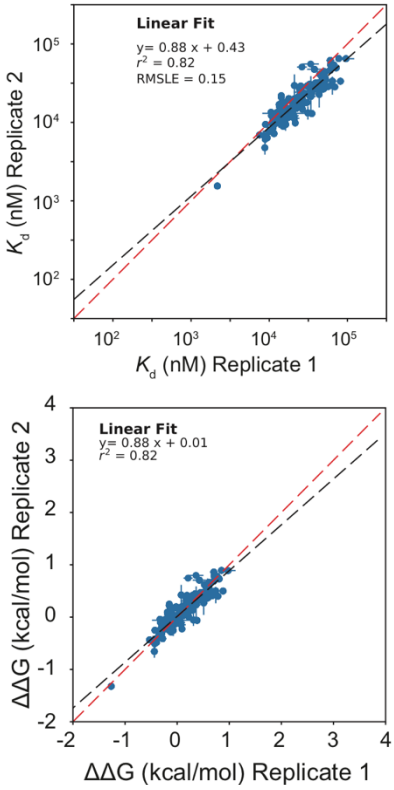

Figure S15 (Related to Figure 5). Pairwise comparison of per-mutant K_ds (top row) and ΔΔGs (bottom row) for all TF mutants for all replicates across all DNA sequences in this study. Points indicate median affinities (± SEM) for each TF mutant; all ΔΔGs are calculated relative to the WT Pho4 variant on a per-experiment basis. Black and red dashed lines indicate linear fits and identity lines, respectively.

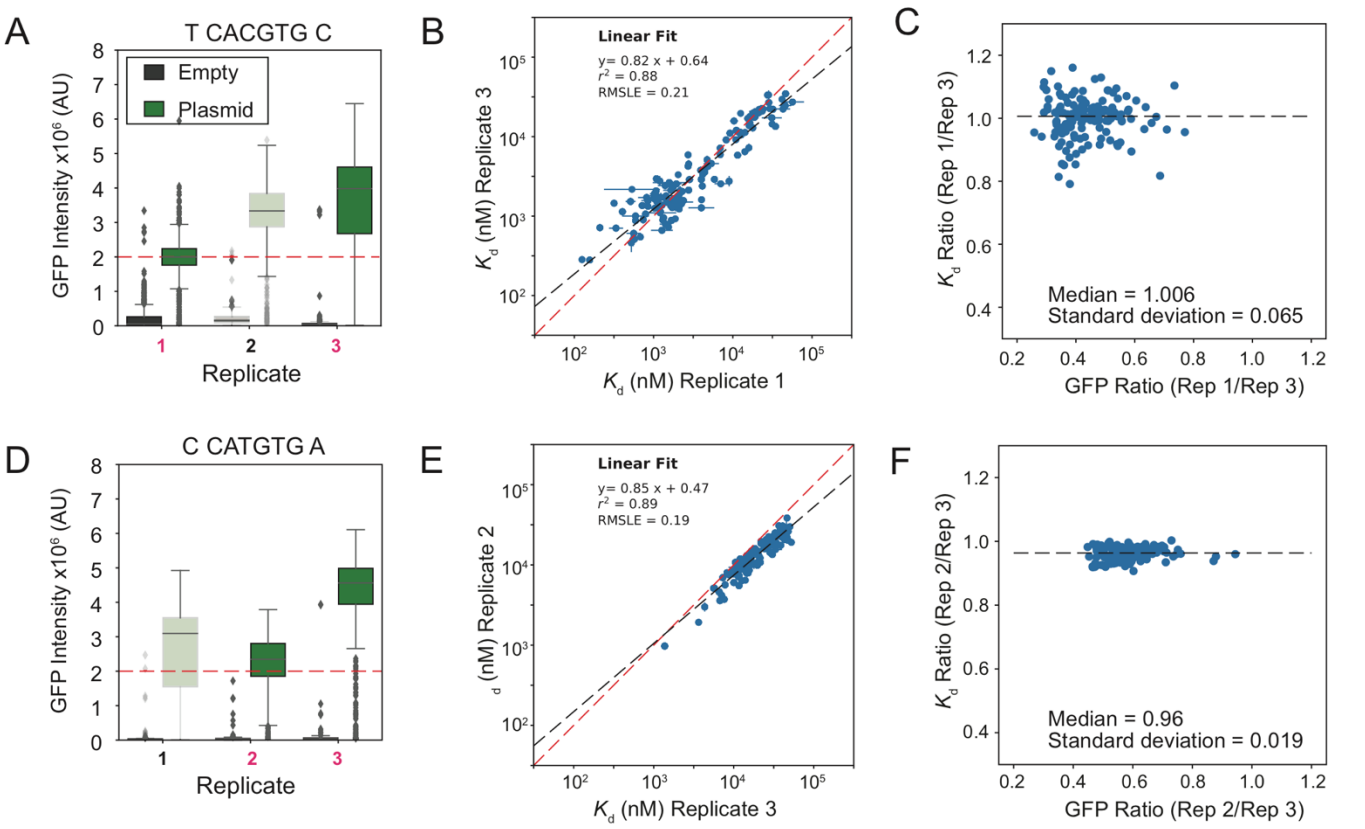

Figure S16 (Related to Figure 5). Measured Kds do not depend on the surface-immobilized TF concentration. **(A)** Boxplots showing intensity of surface-immobilized eGFP-tagged Pho4 across all replicates for oligo sequence 5'-T CACGTG C-3'. **(B)** Pairwise comparison of per-mutant K_ds (left) and ΔΔGs (right) for all TF mutants for replicates 1 and 3 for oligo sequence 5'-T CACGTG C-3'. Data points represent median +/- SEM of affinity measurements. **(C)** Fold K_d versus fold GFP between both replicates. Data represents ratio of median affinities; median K_d ratio = 1.006. **(D)** Boxplots showing intensity of trapped eGFP-tagged Pho4 across all replicates for oligo sequence 5'-C CATGTG A-3'. **(E)** Pairwise comparison of per-mutant K_ds (left) and ΔΔGs (right) for all TF mutants for replicates 1 and 3 for oligo sequence 5'-C CATGTG A-3'. Data points represent median +/- SEM of affinity measurements. **(F)** Fold K_d versus fold GFP between both replicates. Data represents ratio of median affinities; median K_d ratio = 0.96.

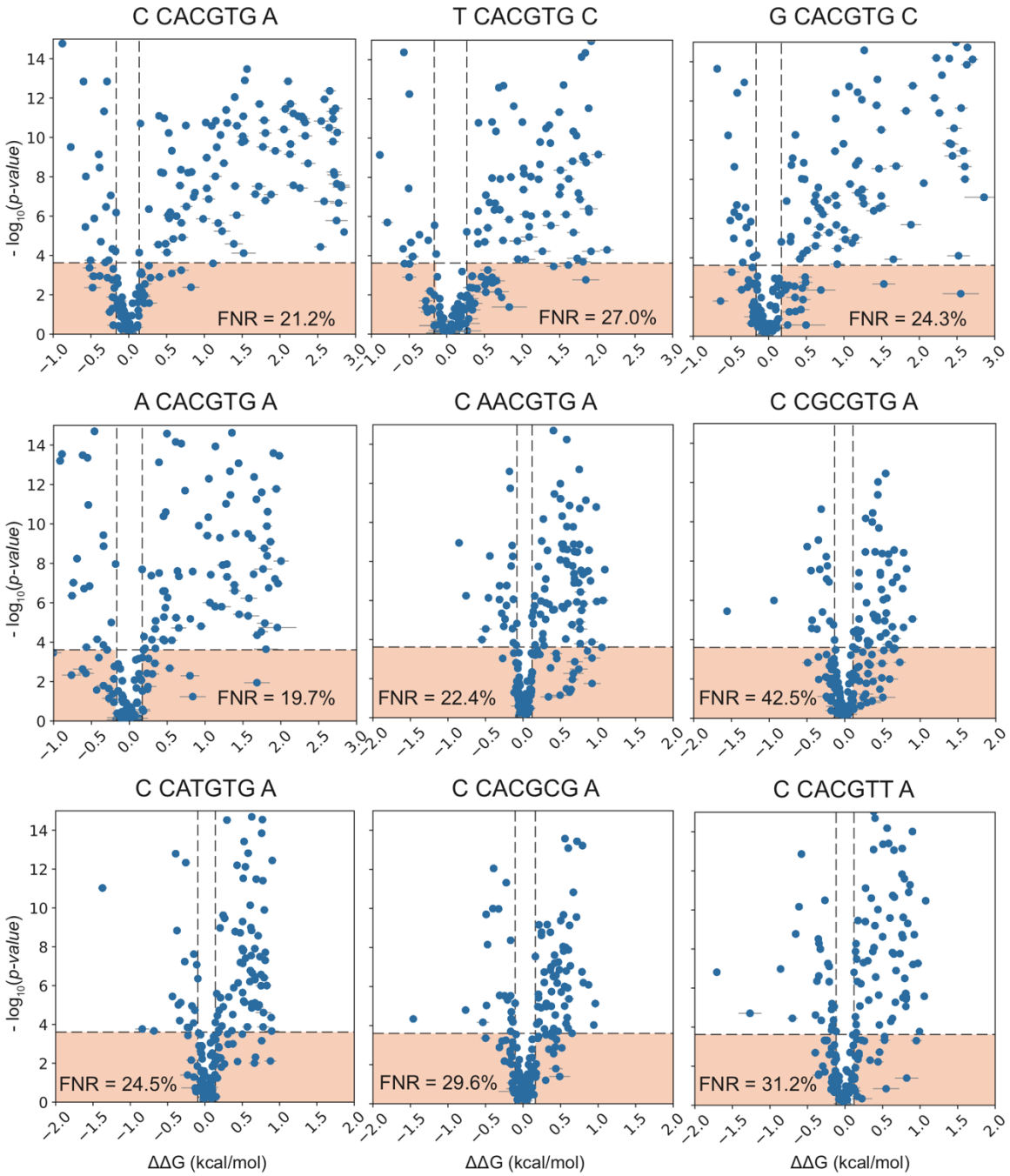

Figure S17 (Related to Figure 5). Comparison of the distribution of measured ΔΔGs (± SEM) for a given mutant vs. the distribution of ΔΔGs for WT Pho4 to determine statistically significant differences in binding (using a two-tailed t-test with a Bonferroni correction). Horizontal dashed line indicates p-value cutoff for statistical significance. Vertical dashed lines indicate minimum perturbations in ΔΔG measurements for which mutants showed statistical difference from wildtype Pho4. Red regions indicate False Negative (FN) mutants with ΔΔG perturbations surpassing minimum ΔΔG but not considered different from wildtype. All mutants which were statistically significant were considered True Positive (TP). False Negative Rate (FNR) = FN/(FN+TP).

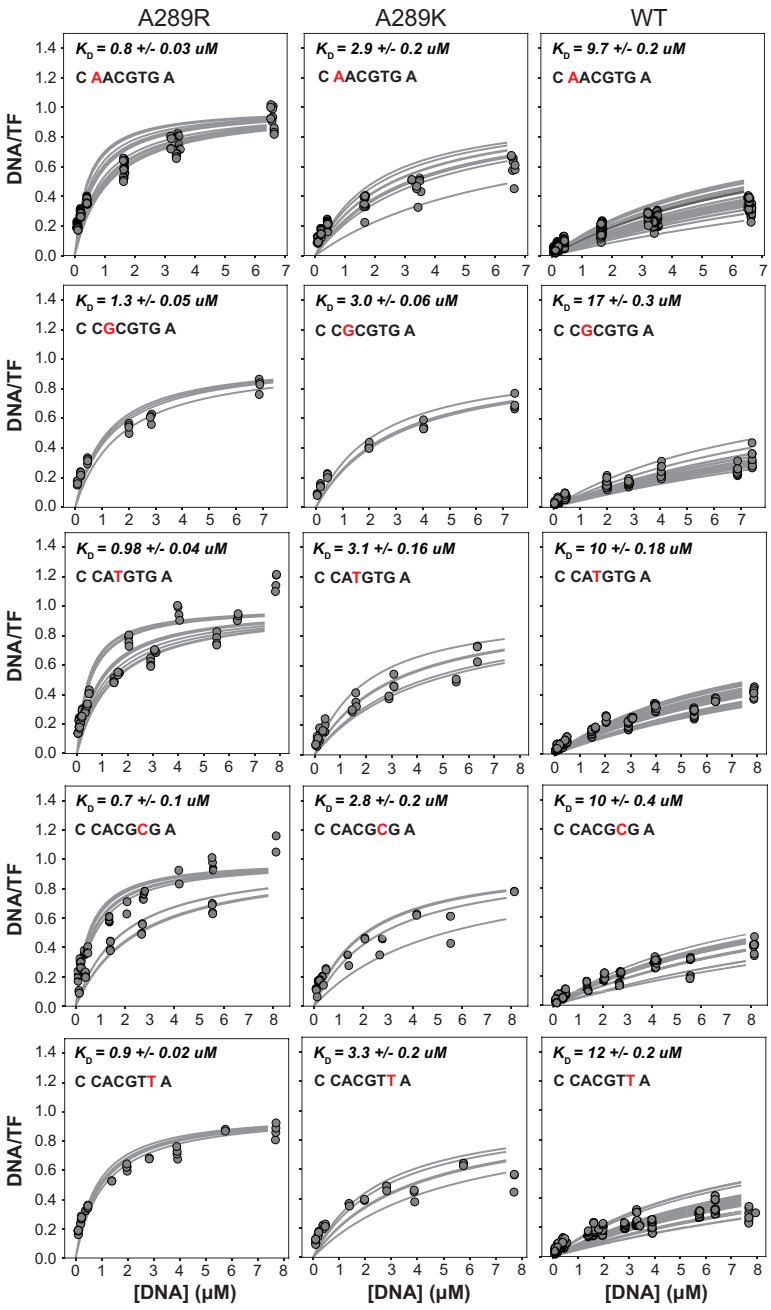

Figure S18 (Related to Figure 5). Concentration-dependent binding curves for mutations at the backbone-contacting residue A289 across all oligonucleotide sequences containing core mutations. A289R and A289K both increase binding affinities for all DNA sequences; K_d values represent the median of all curves ± SEM.

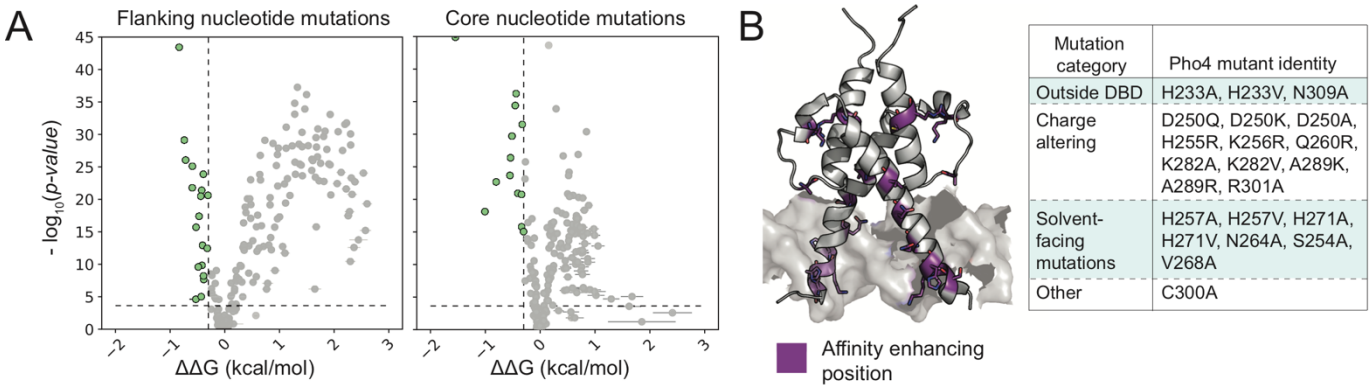

Mutation category	Pho4 mutant identity
Outside DBD	H233A, H233V, N309A
Charge altering	D250Q, D250K, D250A, H255R, K256R, Q260R, K282A, K282V, A289K, A289R, R301A
Solvent-facing mutations	H257A, H257V, H271A, H271V, N264A, S254A, V268A
Other	C300A

Figure S19 (Related to Figure 5 and methods). Affinity-enhancing Pho4 mutations. **(A)** Calculated -$\log_{10}$(*p*-values) (two-tailed T-test) *vs.* measured ΔΔG values (median ± SEM) for Pho4 variants interacting with DNA sequences containing mutations to flanking (left) or core (right) nucleotides; mutations with significantly enhanced binding are highlighted in green. **(B)** Location of affinity-enhancing mutations on Pho4 crystal structure and list of residues.

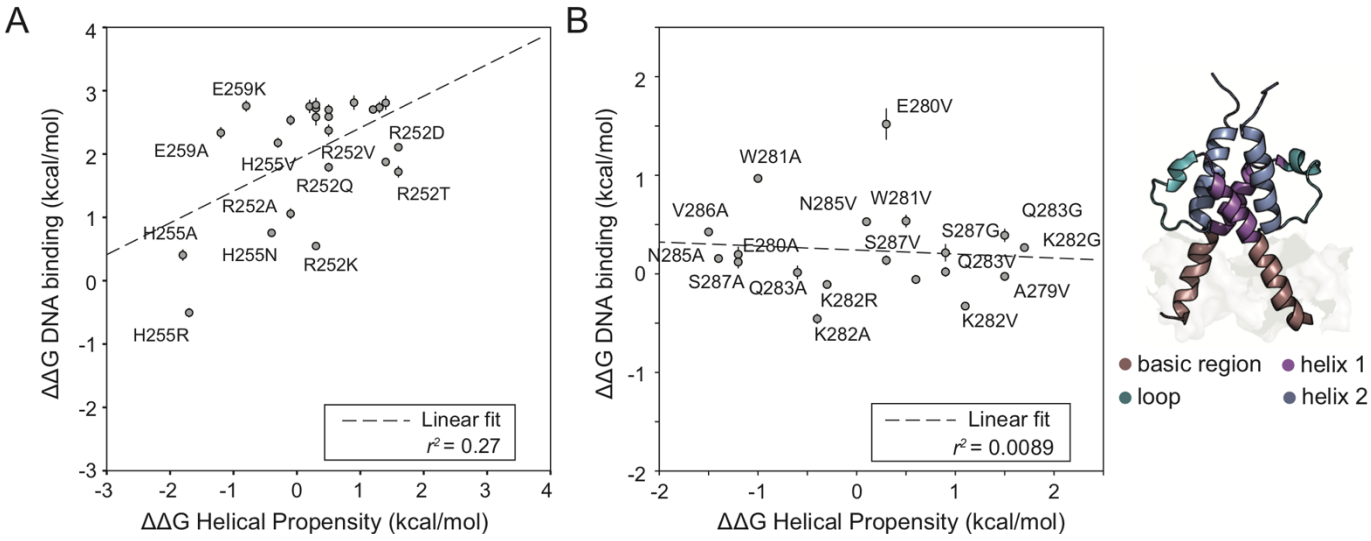

Figure S20 (Related to Figure 6). Measured ΔΔGs for substitutions to nucleotide-contacting and loop residues do not correlate with predicted changes in helical propensity. **(A)** Measured ΔΔGs for mutations at nucleotide-contacting residues *vs.* predicted changes in helical propensity (r^2 = 0.27; RMSE = 2.0 kcal/mol); as expected, ΔΔG effects are dominated by changes to residue/DNA contacts. **(B)** Measured ΔΔGs for mutations in unstructured loop region *vs.* predicted changes in helical propensity (r^2 = 0.0089; RMSE = 1.2 kcal/mol); as expected, ΔΔG effects in unstructured regions do not correlate with changes in helical propensity.

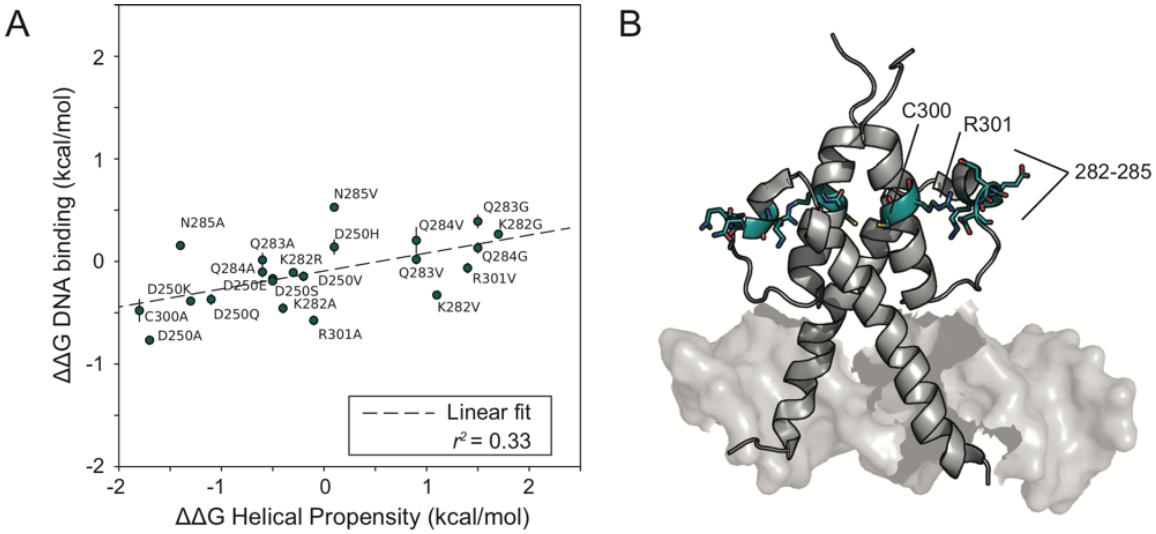

Figure S21 (Related to Figure 6). (A) Comparison of changes in helical propensity with change in binding energy relative to wildtype for mutants at positions within helical area of loop region (residues 282-285), and helix 2 (C300, R301). **(B)** Positions of mutated residues shown on Pho4 crystal structure (PDB: 1A0A), residues 282-285, 300, and 301 highlighted in teal.

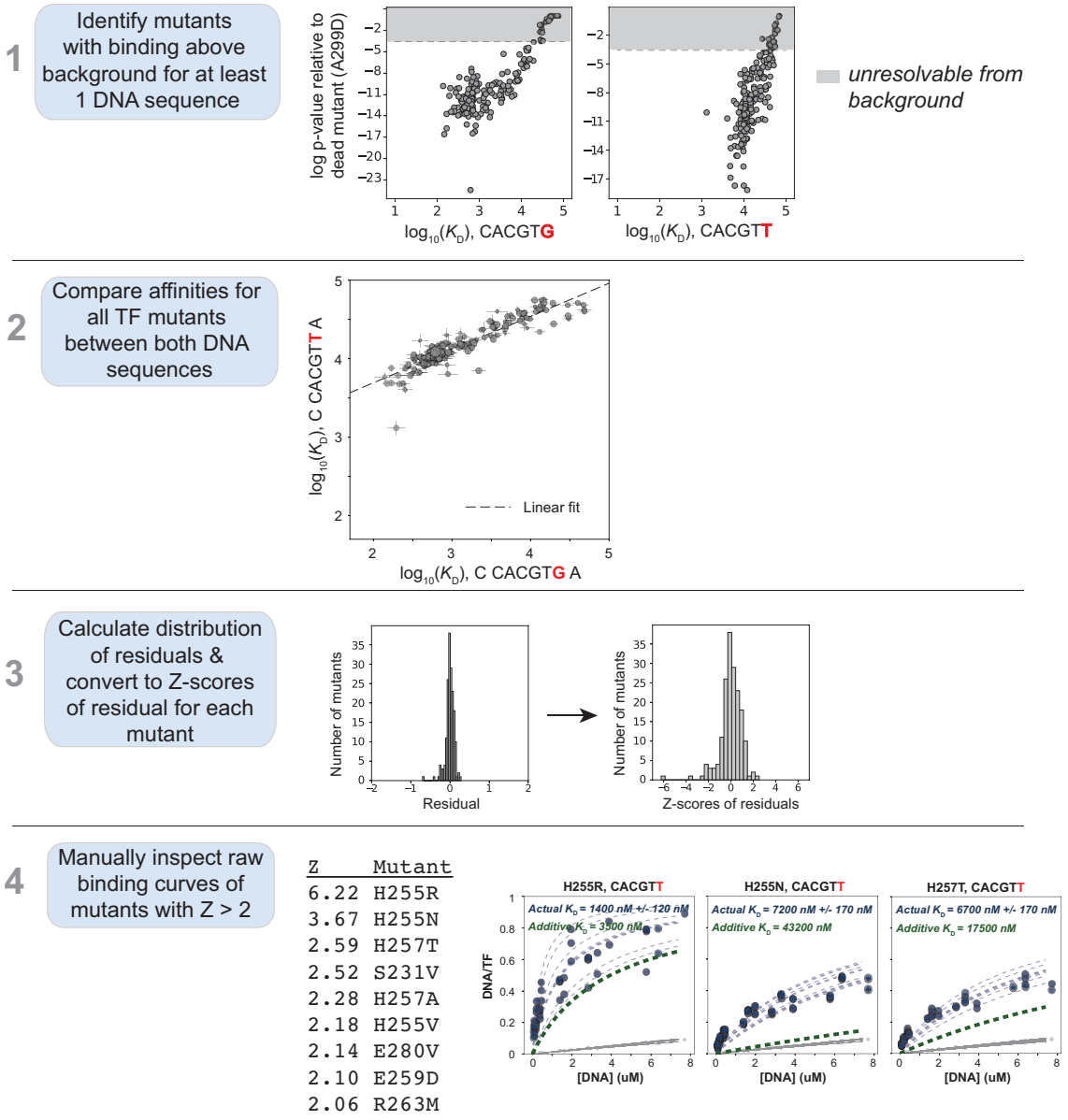

Figure S22 (Related to Figure 7). Analysis pipeline for identifying epistasis (non-additivity) between TF and DNA mutations.

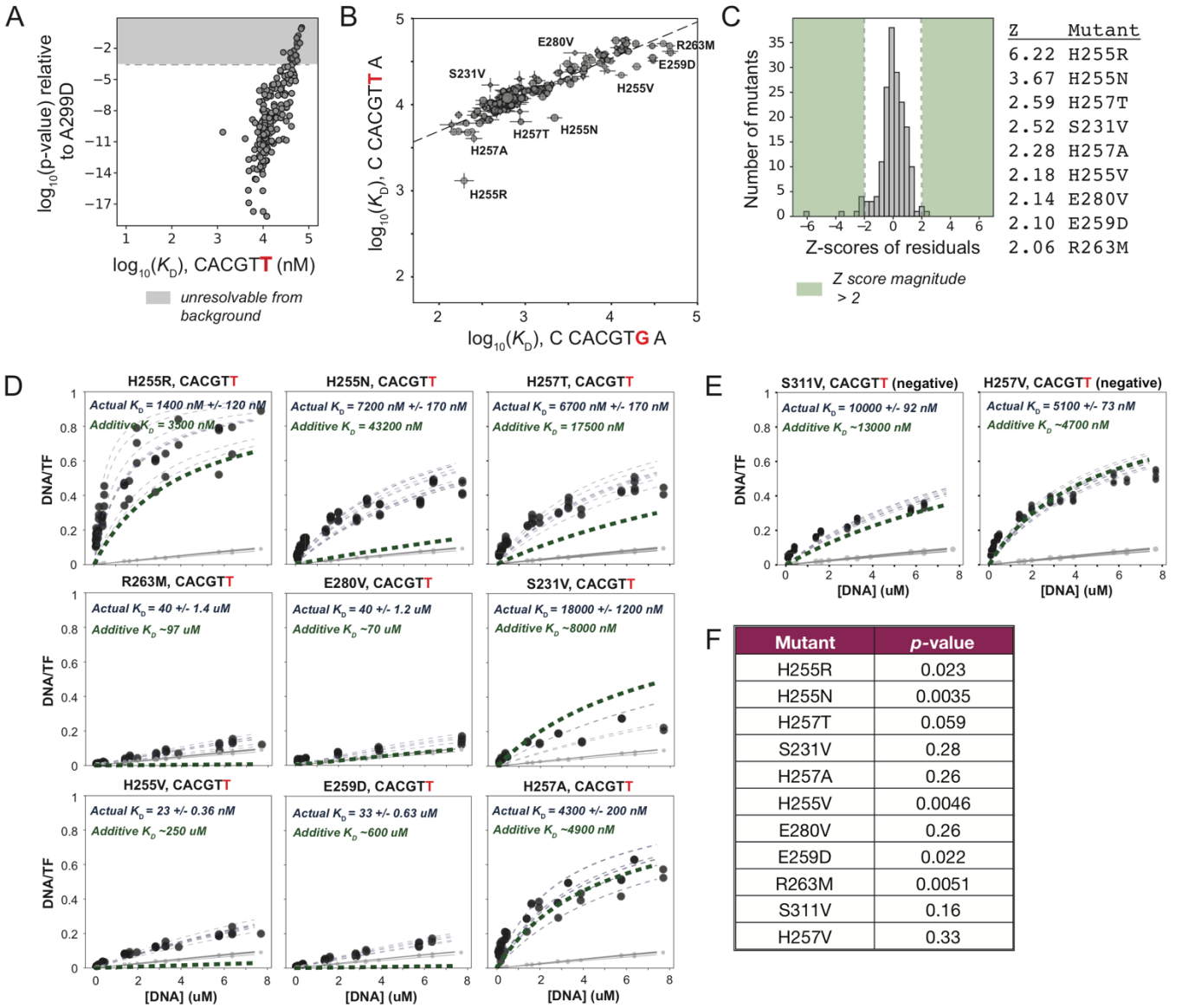

F

Mutant	*p*-value
H255R	0.023
H255N	0.0035
H257T	0.059
S231V	0.28
H257A	0.26
H255V	0.0046
E280V	0.26
E259D	0.022
R263M	0.0051
S311V	0.16
H257V	0.33

Figure S23 (Related to Figure 7). Double-mutant cycle analysis across the TF-DNA interface for the 5'-C CACGTG A-3' and 5'-C CACGTT A-3' oligonucleotides. **(A)** Identification of mutants statistically resolvable from background for 5'-C CACGTT A-3' binding measurements. **(B)** Pairwise comparisons of measured $\log_{10}(K_d)$ values (median ± SEM) for Pho4 mutants for 5'-C CACGTG A-3' and 5'-C CACGTT A-3' oligonucleotides with outliers labeled. Dashed line indicates linear fit to plotted data (r^2 = 0.84). **(C)** Distribution of residual Z-scores (standardized residuals) with magnitude Z-score ≥ 2 highlighted and candidate mutants listed. **(D)** Validation of mutants with Z-scores ≥ 2; boldened green dashed curves represent binding curve for an expected K_d for which TF and DNA mutations are purely additive. **(E)** Example additive mutants conforming to non-epistatic expectation. **(F)** Two-tailed T-test results comparing experimental double-mutant measurement to distribution of predictive additive K_d measurements.

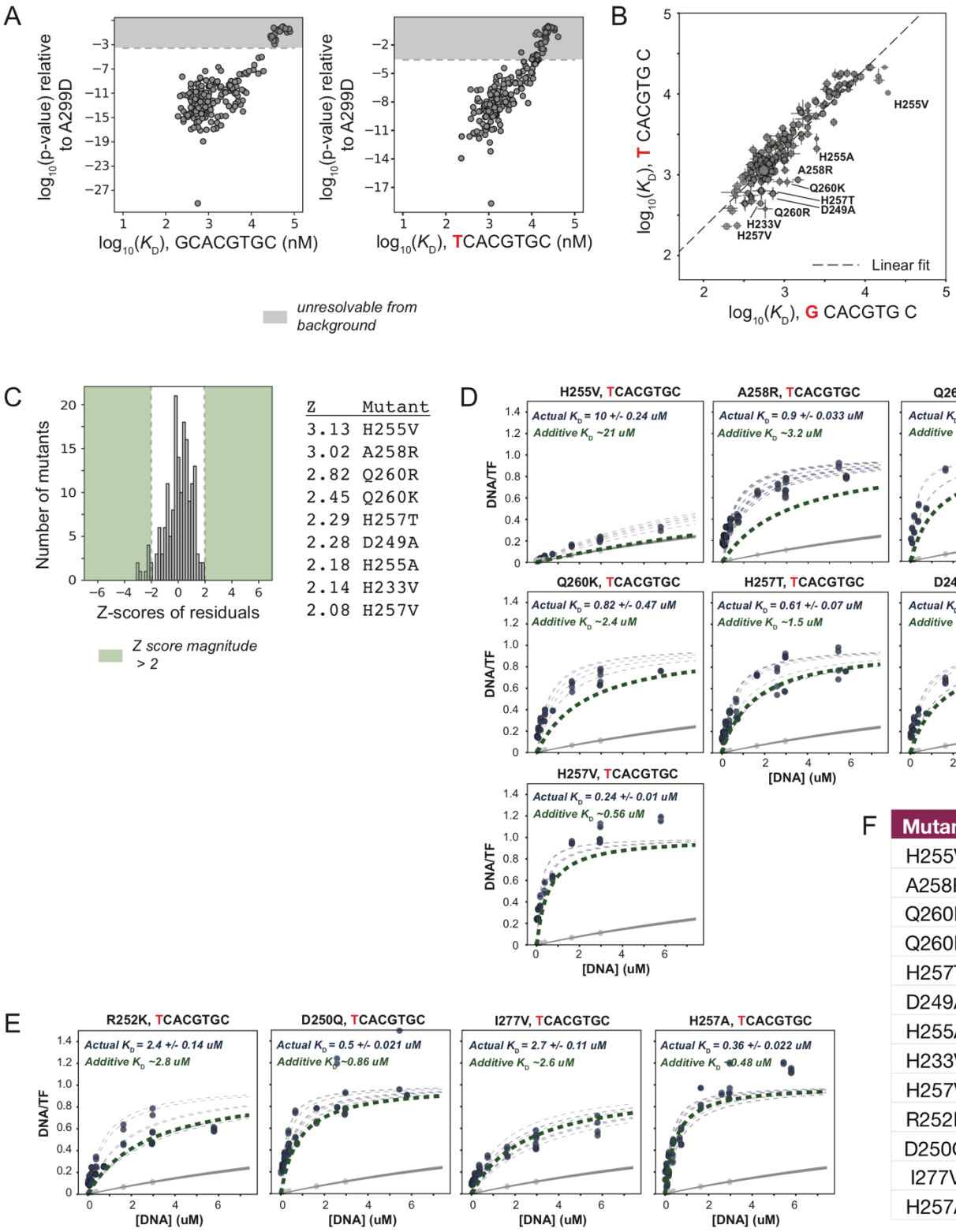

Mutant	*p*-value
H255V	0.015
A258R	0.0055
Q260R	0.082
Q260K	0.031
H257T	0.12
D249A	0.19
H255A	0.019
H233V	0.018
H257V	0.0090
R252K	0.41
D250Q	0.067
I277V	0.70
H257A	0.24

Figure S24 (Related to Figure 7). Double-mutant cycle analysis across the TF-DNA interface for the 5'-G CACGTG C-3'and 5'-T CACGTG C-3 oligonucleotides. **(A)** Identification of mutants with binding statistically resolvable from background for 5'-G CACGTG C-3' and 5'-T CACGTG C-3' sequences. **(B)** Pairwise comparisons of measured K_ds (median ± SEM) for TF variants binding 5'-G CACGTG C-3' and 5'-T CACGTG C-3' DNA sequences with outliers marked; dashed line indicates linear fit (r^2 = 0.85). **(C)**

Distribution of residual Z-scores (standardized residuals) with magnitude Z-score ≥ 2 highlighted and candidate mutants listed. **(D)** Validation of mutants with Z-scores ≥ 2; boldened green dashed curves represent binding curve for an expected K_d for which TF and DNA mutations are purely additive. **(E)** Example additive mutants conforming to non-epistatic expectation. **(F)** Two-tailed T-test results comparing experimental double-mutant measurement to distribution of predictive additive K_d measurements.

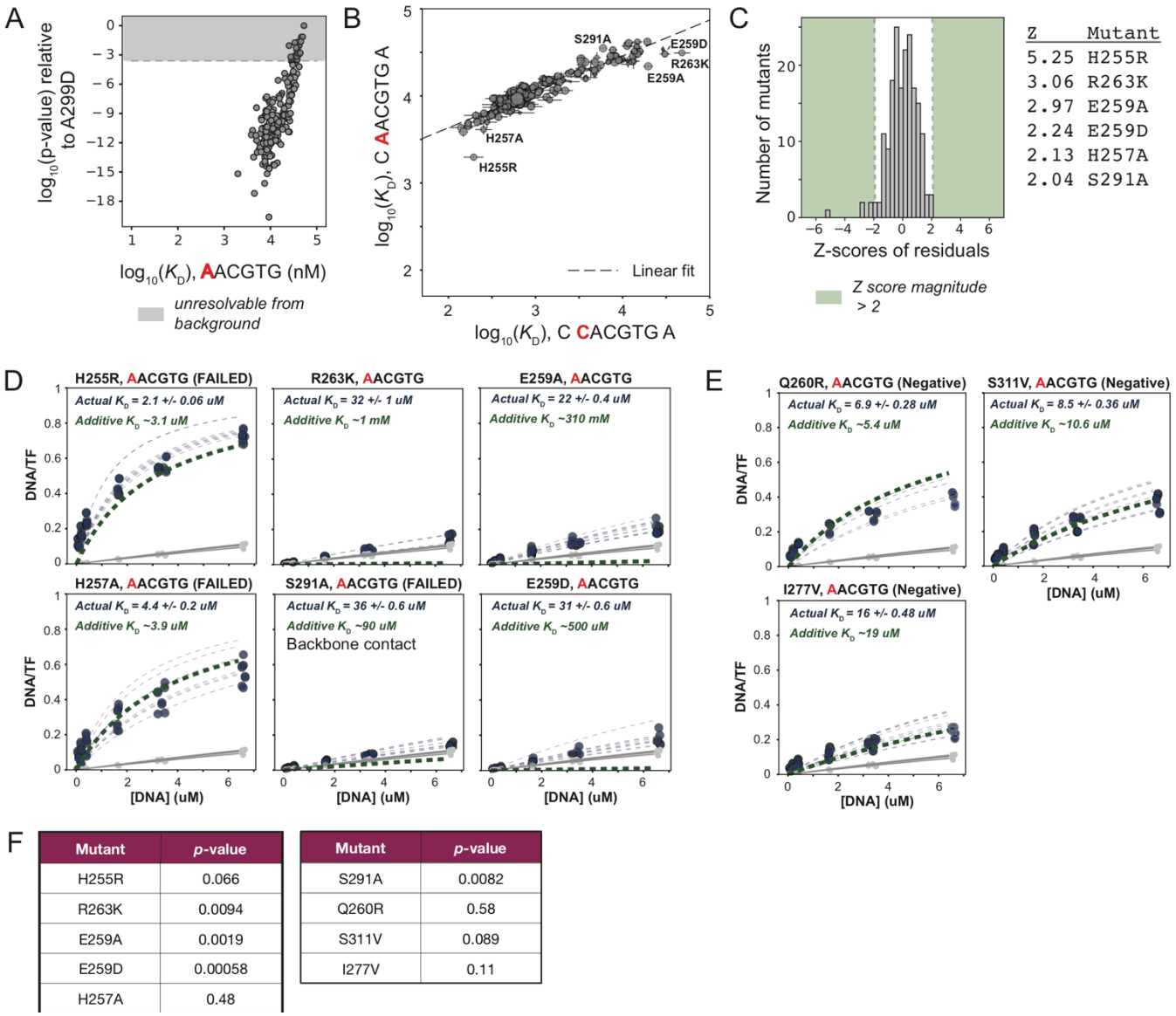

F

Mutant	*p*-value
H255R	0.066
R263K	0.0094
E259A	0.0019
E259D	0.00058
H257A	0.48

Mutant	*p*-value
S291A	0.0082
Q260R	0.58
S311V	0.089
I277V	0.11

Figure S25 (Related to Figure 7). Double-mutant cycle analysis across the TF-DNA interface for the 5'-G CACGTG C-3'and 5'-C AACGTG C-3 oligonucleotides. **(A)** Identification of mutants statistically resolvable from background for 5'-C AACGTG A-3' binding measurements. **(B)** Pairwise comparisons of measured affinities (K_ds, median ± SEM) for TF variants binding 5'-C CACGTG A-3' and 5'-C AACGTG A-3' DNA sequences with outliers marked; dashed line indicates linear fit (r^2 = 0.88). **(C)** Distribution of residual Z-scores (standardized residuals) with magnitude Z-score ≥ 2 highlighted and candidate mutants listed. **(D)** Validation of mutants with Z-scores ≥ 2; boldened green dashed curves represent binding curve for an expected K_d for which TF and DNA mutations are purely additive. **(E)** Example additive mutants conforming to non-epistatic expectation. **(F)** Two-tailed T-test results comparing experimental double-mutant measurement to distribution of predictive additive K_d measurements.

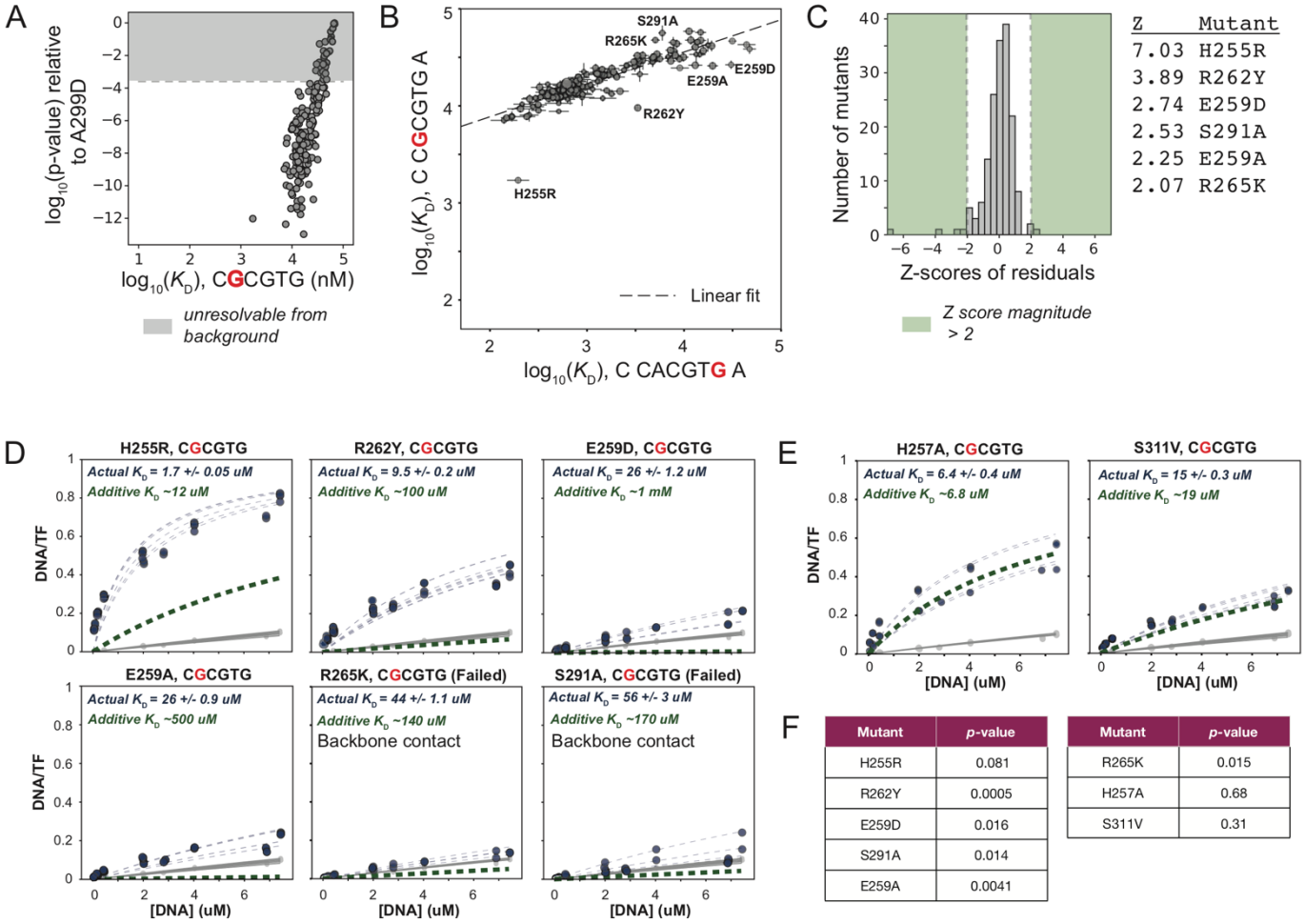

Mutant	*p*-value
H255R	0.081
R262Y	0.0005
E259D	0.016
S291A	0.014
E259A	0.0041

Mutant	*p*-value
R265K	0.015
H257A	0.68
S311V	0.31

Figure S26 (Related to Figure 7). Double-mutant cycle analysis across the TF-DNA interface for the 5'-G CACGTG C-3'and 5'-C CGCGTG C-3 oligonucleotides. **(A)** Identification of mutants statistically resolvable from background for 5'-C CGCGTG A-3' binding measurements. **(B)** Pairwise comparisons of measured affinities (K_ds, median ± SEM) for TF variants binding 5'-C CACGTG A-3' and 5'-C CGCGTG A-3' DNA sequences with outliers marked; dashed line indicates linear fit (r^2 = 0.76). **(C)** Distribution of residual Z-scores (standardized residuals) with magnitude Z-score ≥ 2 highlighted and candidate mutants listed. **(D)** Validation of mutants with Z-scores ≥ 2; boldened green dashed curves represent binding curve for an expected K_d for which TF and DNA mutations are purely additive. **(E)** Example additive mutants conforming to non-epistatic expectation. **(F)** Two-tailed T-test results comparing experimental double-mutant measurement to distribution of predictive additive K_d measurements.

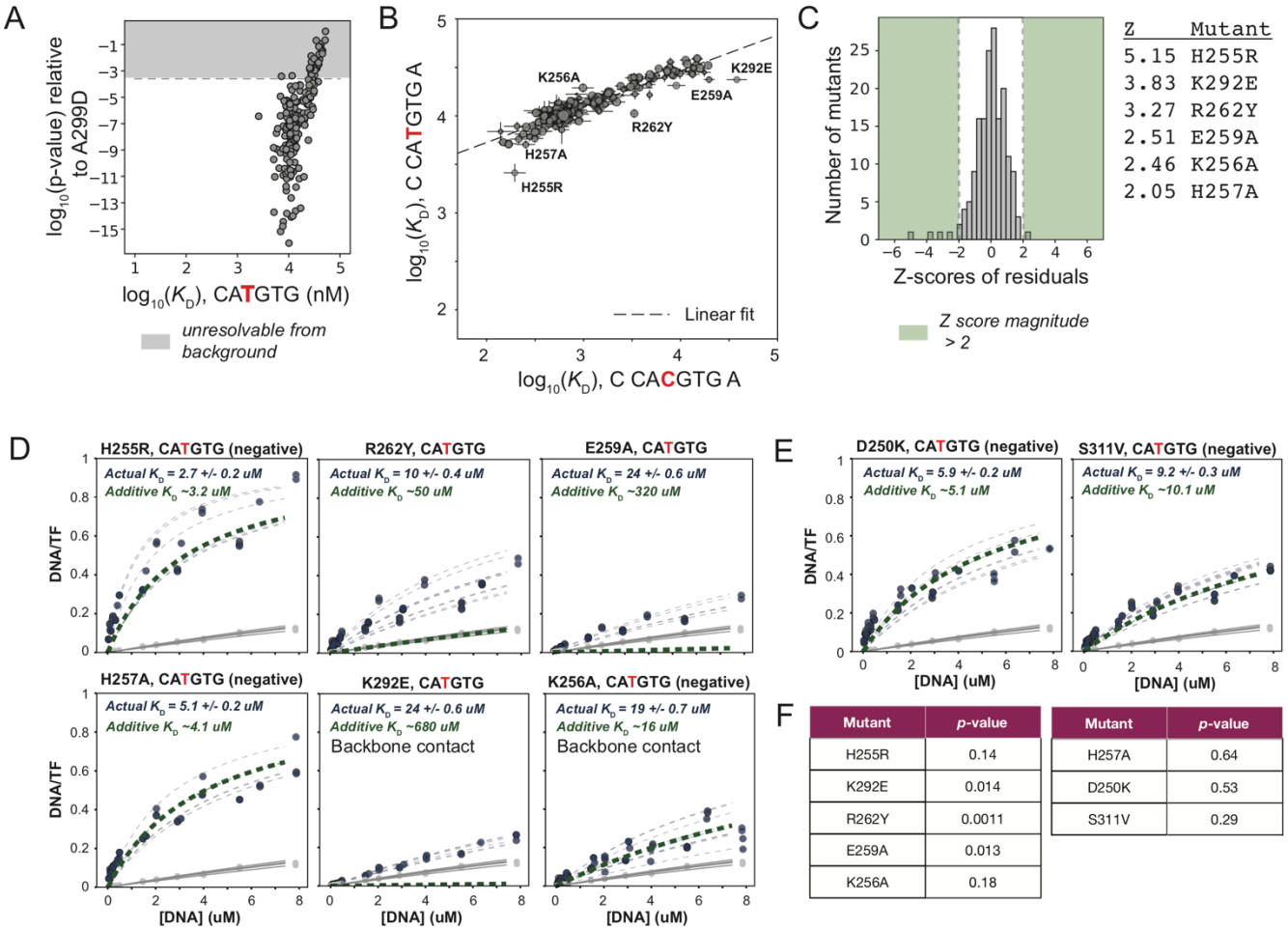

F

Mutant	*p*-value
H255R	0.14
K292E	0.014
R262Y	0.0011
E259A	0.013
K256A	0.18

Mutant	*p*-value
H257A	0.64
D250K	0.53
S311V	0.29

Figure S27 (Related to Figure 7). Double-mutant cycle analysis across the TF-DNA interface for the 5'-G CACGTG C-3'and 5'-C CATGTG C-3 oligonucleotides. **(A)** Identification of mutants statistically resolvable from background for 5'-C CATGTG A-3' binding measurements. **(B)** Pairwise comparisons of measured affinities (K_ds, median ± SEM) for TF variants binding 5'-C CACGTG A-3' and 5'-C CATGTG A-3' DNA sequences with outliers marked; dashed line indicates linear fit to plotted data (r^2 = 0.86). **(C)** Distribution of residual Z-scores (standardized residuals) with magnitude Z-score ≥ 2 highlighted and candidate mutants listed. **(D)** Validation of mutants with Z-scores ≥ 2; boldened green dashed curves represent binding curve for an expected K_d for which TF and DNA mutations are purely additive. **(E)** Example additive mutants conforming to non-epistatic expectation. **(F)** Two-tailed T-test results comparing experimental double-mutant measurement to distribution of predictive additive K_d measurements.

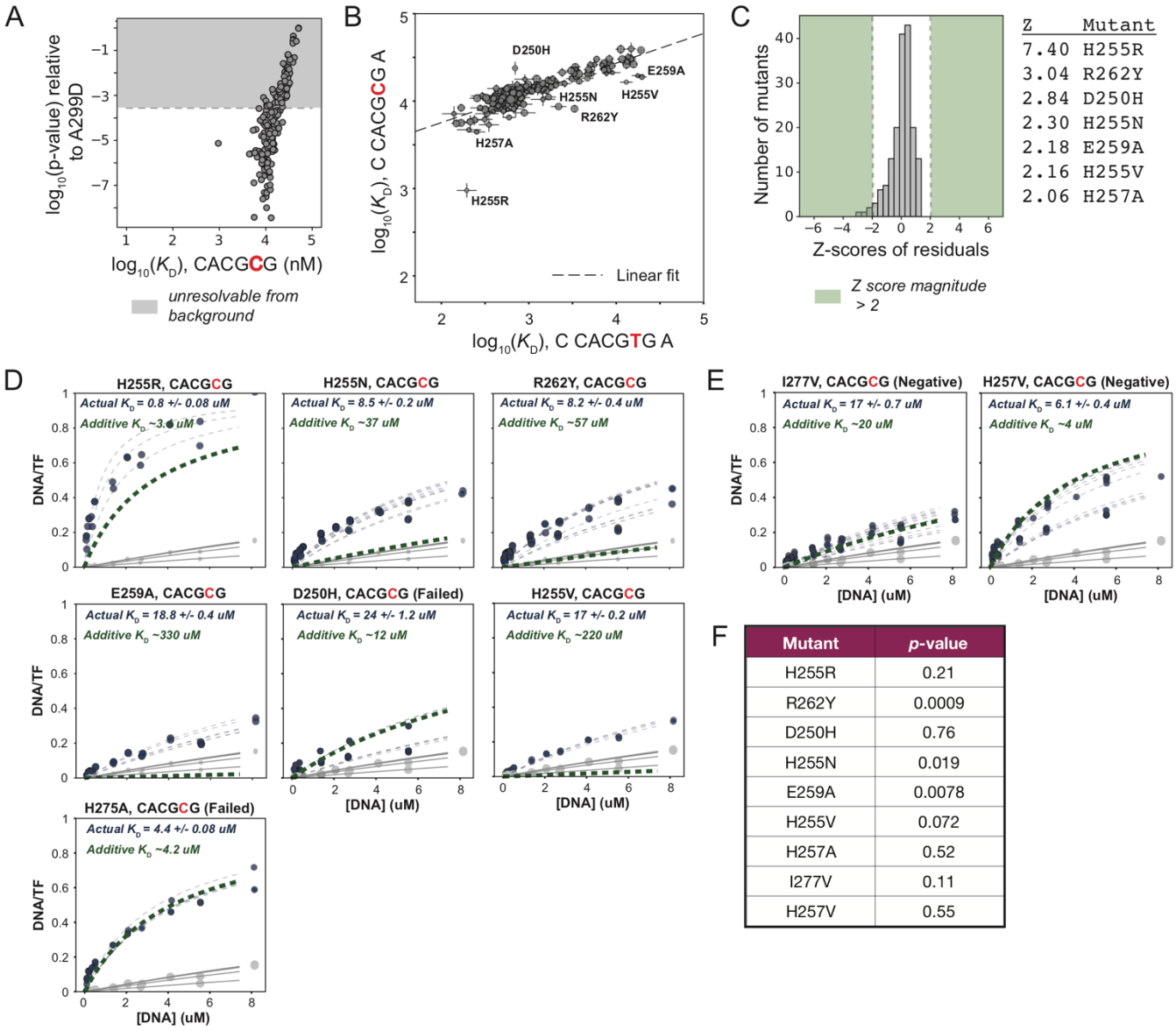

Mutant	*p*-value
H255R	0.21
R262Y	0.0009
D250H	0.76
H255N	0.019
E259A	0.0078
H255V	0.072
H257A	0.52
I277V	0.11
H257V	0.55

Figure S28 (Related to Figure 7). Double-mutant cycle analysis across the TF-DNA interface for the 5'-G CACGTG C-3'and 5'-C CACGCG C-3 oligonucleotides. **(A)** Identification of mutants statistically resolvable from background for 5'-C CACGCG A-3' binding measurements. **(B)** Pairwise comparisons of median affinities (± SEM) for TF mutants between 5'-CCACGTGA-3' and 5'- CCACGCGA -3' DNA sequences with outliers marked. Dashed line indicates linear fit to plotted data. Linear fit r^2 = 0.69). **(C)** Distribution of residual Z-scores (standardized residuals) with magnitude Z-score ≥ 2 highlighted and candidate mutants listed. **(D)** Validation of mutants with Z-scores ≥ 2; boldened green dashed curves represent binding curve for an expected K_d for which TF and DNA mutations are purely additive. **(E)** Example additive mutants conforming to non-epistatic expectation. **(F)** Two-tailed T-test results comparing experimental double-mutant measurement to distribution of predictive additive K_d measurements.

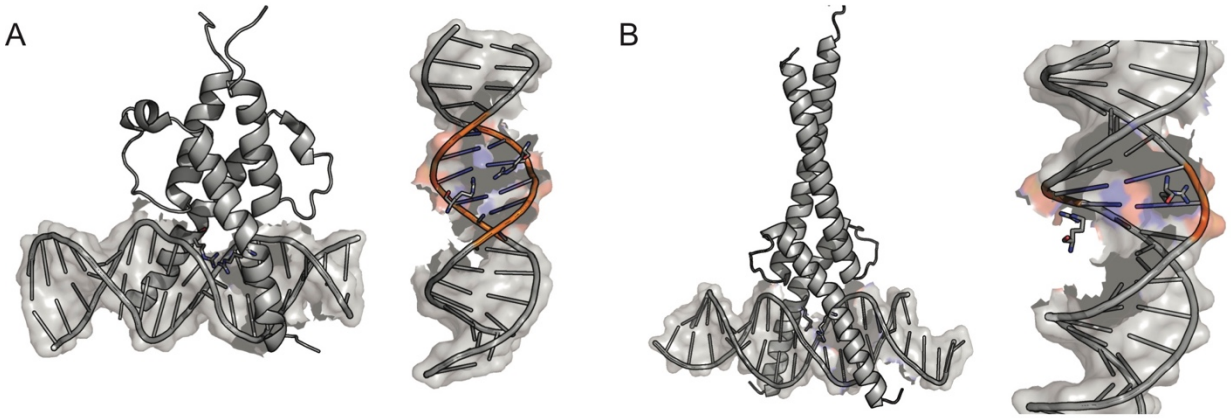

Figure S29 (Related to Figure 7). Comparison of 13th arginine in DNA binding domains for Pho4 and SREBP1. **(A)** Pho4 bound to DNA (PDB: 1A0A) (left); DNA molecule with 13th arginine residue in Pho4 (R263) shown as sticks making contacts across central nucleotides in E-box motif (right). Portion of DNA sequence containing E-box indicated by orange DNA backbone. **(B)** SREBP1 bound to DNA (PDB: 1AM9) (left); DNA molecule with 13th arginine residue in SREBP1 shown as sticks contacting DNA backbone (right). Conformations of arginine for both monomers are symmetric regardless of half-site identity. Portion of DNA sequence containing E-box indicated by orange DNA backbone.